Master in Mining and Geological Engineering

University of Liège - Faculty of Applied Sciences

Department UEE

Inversion and Prediction-Focused Approach (PFA) imaging of multiple loops Surface Nuclear Magnetic Resonance (SNMR) data

Graduation Studies conducted for obtaining the Master's degree
in Mining and Geological Engineering by
Hadrien Michel

Supervisor
Prof. Dr. Frédéric Nguyen

Academic year 2017-2018

Acknowledgements

Many people have contributed to the present work. Without their knowledge, advices and support, this work would not have been possible. I would like to thank some of them in particular.

Prof. Dr. Thomas Hermans for the unique opportunity to carry out an internship at the UGent and his time and tenacity in teaching the concepts inherent to Bayesian evidential learning. Moreover, his latest reviews of my codes have been salutary.

Prof. Dr. Frédéric Nguyen to trust me in conducting research on the subject of SNMR data interpretation, which I truly enjoyed; for the revisions of my results and the constructive comments that always helped me to get forward and continue on the right track; and for the continuous work as a supervisor.

Thomas Kremer, for his help in the introduction to the heavy subject of SNMR, his countless reviews of my results and the constructive exchanges.

My mother for the countless grammar and spelling checks, which is clearly not my strength.

All my family and friends for their support all along this work.

Finally, for their day-to-day support, whatever my mood, I would like to thank Gojira, Metallica, Radiohead, Muse and all the other bands that accompanied my countless hours of work on my desk late at night.

Abstract (English)

Surface Nuclear Magnetic Resonance (SNMR) is a geophysical experiment that enables to retrieve hydrogeological parameters of the subsurface with surface-based measurements. However, the method suffers from a low signal-to-noise ratio. To overcome this impediment, a new experimental configuration, called the multiple loops (or multi-central) configuration, is introduced, benefiting from both a decreased signal-to-noise ratio and an increased sensitivity to shallow subsurface. In order to take advantage of those improvements, an adaptation of the state-of-the-art QT inversion is proposed. On the other hand, a novel innovative approach to SNMR data interpretation is developed and tested. This approach, called prediction-focused approach (PFA) imaging, is part of a broader alternative way to exploit geophysical data: Bayesian evidential learning (BEL). PFA enables a quantification of the uncertainty on model parameters issued from statistics-based relations between simulated models and data. Finally, the QT inversion approach and the PFA imaging are tested on synthetic and real multiple loops experiments, proving the usefulness of the multiple loops configuration in specific contexts.

Abstract (Français)

La résonance magnétique protonique (RMP) est une expérience géophysique qui permet de récupérer les paramètres hydrogéologiques de la subsurface à l'aide de mesures de surface. Cependant, la méthode souffre d'un faible rapport signal/bruit. Pour surmonter cet obstacle, une nouvelle configuration expérimentale, appelée configuration à multi-boucles (ou multi-centrale), est introduite, bénéficiant à la fois d'un rapport signal/bruit réduit et d'une sensibilité accrue à la subsurface peu profonde. Afin de profiter de ces avantages, une adaptation de l'inversion QT à la pointe de la technologie est proposée. D'autre part, une nouvelle approche innovante de l'interprétation des données SNMR est développée et testée. Cette approche, appelée imagerie par approche prédictive (prediction-focused approach, PFA), fait partie d'une méthode alternative, plus large, d'exploitation des données géophysiques: l'apprentissage probant bayésien (Bayesian evidential learning, BEL). La PFA permet une quantification de l'incertitude sur les paramètres de modèles à l'aide de relations statistiques entre des modèles et des données simulés. Enfin, l'approche d'inversion QT et l'imagerie PFA sont testées sur des expériences multi-boucles synthétiques et réelles, prouvant l'utilité de la configuration multi-boucles dans des contextes spécifiques.

Abstract (Nederlands)

Surface Nuclear Magnetic Resonance (SNMR) is een geofysisch experiment dat mogelijk maakt hydrogeologische parameters van de ondergrond achter te halen met oppervlak gebaseerde metingen. De methode heeft echter een lage signaal-ruisverhouding. Om deze belemmering over te winnen, wordt een nieuwe experimentele configuratie geïntroduceerd, de multi-lussen (of multi-centrale) configuratie, die profiteert van zowel een verlaagde signaal-ruisverhouding als een verhoogde gevoeligheid voor ondiepe ondergrond. Om van deze voordelen te kunnen genieten, wordt echter een aanpassing van de state-of-the-art QT inversie ontwikkeld. Aan de andere kant is een nieuwe, innovatieve benadering van de interpretatie van SNMR-gegevens ontwikkeld en getest. Deze benadering, genaamd voorspelling-gerichte benadering beeldvorming (prediction-focused approach, PFA), maakt deel uit van een bredere alternatieve manier om geofysische gegevens te exploiteren: Bayesian evidential learning (BEL). PFA maakt een kwantificering mogelijk van de onzekerheid op modelparameters die worden uitgegeven door op statistieken gebaseerde relaties tussen gesimuleerde modellen en gegevens. Ten slotte worden de QT inversie-benadering en de PFA-beeldvorming getest op synthetische en reële multi-lussen experimenten, die het nut bewijzen van de configuratie van multi-lussen in specifieke contexten.

Contents

List of Figures

List of Tables

Chapter 1

Introduction

Surface Nuclear Magnetic Resonance is a near-surface geophysical method used to retrieve informations about groundwater in the subsurface up to 150 m. It exploits quantum mechanics behavior of protons contained in water molecules in a magnetic field. At rest, the spins of the protons precess about Earth's magnetic field $\mathbf{B}_E$ at a specific frequency called the Larmor frequency. The SNMR experiment consists in disturbing the thermal equilibrium by applying a secondary magnetic field for a short time, thus perturbing the equilibrium. When the man-made secondary magnetic field is removed, the spins are relaxed back to their thermal equilibrium, emitting a magnetic field that is registered via the induced current in the receiver loop (free induction decay). This signal can be interpreted in terms of water content and relaxation time. These parameters can also be correlated to hydrogeological parameters such as pore sizes and hydraulic conductivities using petrophysical relations (Behroozmand et al., 2015).

However, this type of experiment suffers from a significant drawback: the signal-to-noise ratio is generally very low. In order to alleviate this impediment, Behroozmand, Auken, Fiandaca, and Rejkjaer (2016) proposed the use of coaxial transmitter/receiver couples instead of the classically used coincident transmitter/receiver couples. They demonstrated that the behavior of inner receiver loops was superior to the classical configuration: they were less prone to noise, resulting in a higher signal-to-noise ratio, but also they were more sensitive to shallower zones of the subsurface. However, the in-depth sensitivity is slightly reduced by this configuration. The subject of this work is to propose a method that fully benefits from the advantages of both coincident and coaxial loops: the multiple loops (or multi-central) configuration. This configuration uses both the classical transmitter/receiver couples combined with other couples composed of coaxial receiver loops (Kremer et al., 2018).

In SNMR, the QT inversion (Mueller-Petke & Yaramanci, 2010) is the state-of-the-art approach for the interpretation of FID signals. However, this inversion scheme is not yet

adapted to the use of multiple loops. Therefore, a new definition of the kernel functions needs to be stated for this particular case.

On the other hand, quantification of uncertainty based on the classical inversion schemes remains costly in CPU time and memory. Those methods mainly consist of repeated inversions with slightly modified datasets. A second aim of this work is to propose a new approach to uncertainty quantification based on SNMR data (Michel, Nguyen, Kremer, & Hermans, 2018). This new method called Bayesian evidential learning (BEL) (Scheidt, Li, & Caers, 2018) is based on statistical relationships derived from synthetic models. The method has already proven efficient in geophysics (Hermans, Oware, & Caers, 2016). A comprehensive description of the BEL framework, especially the prediction part of BEL, prediction-focused approach (PFA) imaging, is proposed. Then the new method is tested on numerous "classical" synthetic examples (i.e. single transmitter/receiver configuration).

Afterwards, the multiple loops configuration is tested on synthetic models using both the adapted QT inversion and the PFA imaging process. Finally, the developed methodologies are exploited with a real dataset from a well-studied hydrogeological test site in Germany: Schillerslage (Dlugosch, 2014; Mueller-Petke & Yaramanci, 2010). The results will be extensively compared to analyze the effects of both methods for the interpretation of SNMR data using more and more complex configurations.

Chapter 2

Nuclear Magnetic Resonance

Nuclear magnetic resonance is a widely used technique in sciences. From geo-sciences to medicine, the method enables either to detect precise locations of a specific atomic structure or to establish the composition of an object. NMR is based on quantum properties of the matter (Levitt, 2008).

2.1 Basics of Nuclear Magnetic Resonance

The matter is composed of molecules, themselves composed of atoms, themselves composed of electrons and nuclei. Each nucleus has several physical properties among which the most important are the mass, the electric charge, the magnetism and the spin. The spin is the property from which the NMR signal originates. In atoms, the particular combination of different nuclei with different properties produces different energy states but, due to the Pauli Principle that states that two fermions could not have identical quantum states (set of characteristics of the fermion), the energy levels are degenerated. This means that multiple fermions might have the same energy level because they have different spins. When a magnetic field is applied, the degeneracy is broken. This is called the Zeeman splitting (Levitt, 2008).

As the spin angular momentum and the magnetic moment are intimately related by the gyromagnetic ratio (γ), any change in the magnetic field produces variations in the spin precession. This is the property used in nuclear magnetic resonance (NMR) (Levitt, 2008).

The nuclear spins are naturally precessing around the existing magnetic field at the Larmor frequency ω_0, proportional to the gyromagnetic ratio (γ) and to the magnetic field ($\mathbf{B}^0$). The bulk of nuclei that are present in a sample have microscopically different spin polarization axes (the angular momentum axes of the nuclei). However, on a macroscopic

scale, they produce a macroscopic magnetic moment that is measurable (Levitt, 2008).

In the absence of magnetic field, all spins are oriented differently, hence the resulting macroscopic magnetic moment is close to zero. When the sample is suddenly set in a magnetic field, the spins execute Larmor precession around this field. When the magnetic field is applied using a radio frequency pulse tuned to the Larmor frequency of the particle of interest, it produces a significant change in the spin polarization, i.e. a significant macroscopic change (Levitt, 2008). Finally, when the applied magnetic field is removed, the spins are relaxing back to their thermal equilibrium, producing a measurable magnetic field at the Larmor frequency (Levitt, 2008).

Different experimental configurations are co-existing in the different fields of application of the NMR methods. Most of the NMR experiments rely on a strong primary magnetic field (tens of Tesla) produced by a magnet. This enables the primary field to be stable and homogeneous on the scale of the tested sample (Levitt, 2008). However, in geology, surface nuclear magnetic resonance (SNMR) rather uses Earth's magnetic field ($\mathbf{B_E}$) as the primary field (thousands of nano-Tesla) (Behroozmand et al., 2015). It differentiates this experimental process from classical NMR experiments.

The NMR response is characterized by two fundamental parameters: the initial amplitude and the relaxation time. The first consists in the amplitude of the NMR response to a given excitation pulse at the very moment when the pulse is stopped. The relaxation time originates from two different physical processes. The spin-lattice (or longitudinal) relaxation is governed by the movement of the spins back to their original thermal equilibrium. On the other hand, the spin-spin (or transverse) relaxation is related to the loss of coherence of the spins (Levitt, 2008).

2.2 Nuclear Magnetic Resonance in geology

In geosciences, three NMR experiments coexist: Laboratory NMR (Lab-NMR), Borehole NMR (BNMR) and Surface NMR (SNMR). All those methods are used for different purposes.

Lab-NMR

The Lab-NMR experiment consists in the characterization of a small sample in search of specific properties or in the development of petrophysical relations linking NMR parameters to properties of interest for the characterization of larger samples using BNMR or SNMR (Behroozmand et al., 2015).

BNMR

Borehole NMR is a common tool in the petroleum industry to characterize the pore spaces and fluids inside a petroleum reservoir. Due to the large pressures those instruments are subject to, they have a significantly large diameter, reducing their applicability to near-surface geophysics. However, recent works have been conducted to present technologies that are adapted to smaller sites with reasonable diameters of probes as well as reduced costs (Walsh et al., 2013). Those tools allow the characterization of the water content distributions and other hydrogeologically-based parameters of the subsurface without the limitations of the surface-based investigations lead commonly in near-surface geophysics.

SNMR

SNMR measurement is a non-invasive method to retrieve information about near-surface water content and, to a given extent, other hydrogeological parameters. The development of the method began in the early 1980s with the "HYDROSCOPE" instrument release (Russia), the first ever instrument to register a signal from in-situ groundwater. Later, the Russians collaborated with French scientists in order to develop a commercial SNMR equipment (NUMIS). However, the method was still constrained by the limitations linked to ambient noise and noise processing. Those impediments directed the research to multi-channel NMR measurements that enabled the recording of, at the same time, the signal originating from the NMR response of hydrogen in the subsurface and the noise originating from identified sources. These measurements enable the use of the instrument in higher noise environments (Behroozmand et al., 2015).

2.3 The SNMR experiment

Surface nuclear magnetic resonance (SNMR) experiments rely on the same principles as any other NMR experiment. However, SNMR differs from the other NMR applications by a significantly lower primary magnetic field ($\mathbf{B}_0$). Actually, the exploited primary magnetic field is the natural Earth's magnetic field ($\mathbf{B}_E$), which has an amplitude ranging from 25 to 70 μT, very low compared to the classically used magnet-produced fields of tens of T. Above this first impediment, Earth's magnetic field is also slightly fluctuating with diurnal variations or solar activity. However, at the scale of the SNMR experiment, Earth's magnetic field can be considered homogeneous (Behroozmand et al., 2015).

From those informations, it is of prime concern to accurately measure Earth's magnetic field at the experiment location before any measurements, as it will govern the measured response via the Larmor frequency ($\omega_0 = -\gamma \mathbf{B}_E$). Moreover, the declination of the magnetic field is also important to compute the efficient part of the applied energizing

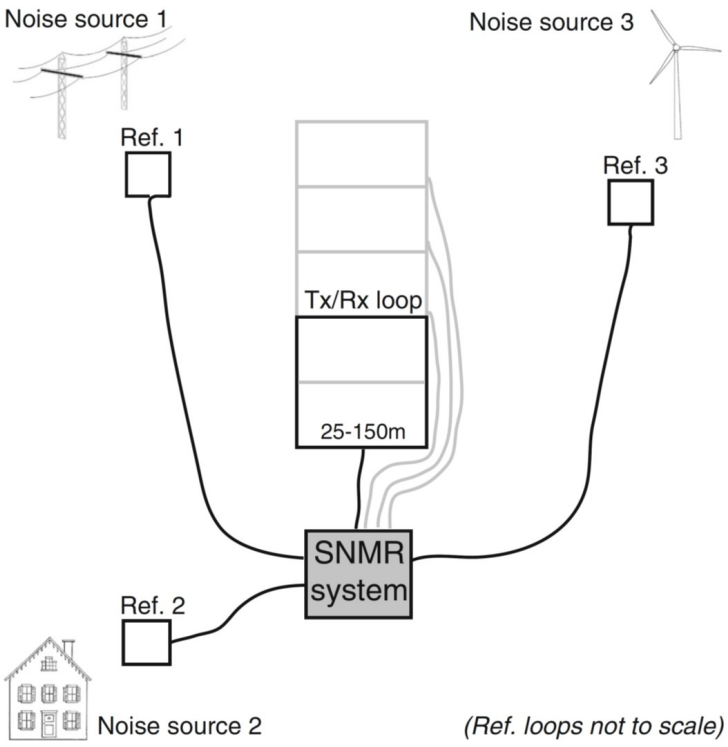

Figure 2.1: Example of experimental design of a multi-channel SNMR experiment accordingly with surrounding noise sources (From Behroozmand et al., 2015).

pulse (see Chapter 3) (Behroozmand et al., 2015). Those measurements are conducted before the NMR measurements in order to gain in accuracy.

The experiment installation consists of the SNMR system coupled with a set of transmitter/receiver loop(s) for signal recording and reference loops for noise recording. These latter are generally placed accordingly with a priori knowledge of noise sources in the surrounding of the experimental site (Figure 2.1).

The transmitter/receiver loops may have different shapes and sizes according to the sites needs. The classical shapes are circles but other shapes as squares or eights are also used in some typical situations. The eight-shape has the advantage of being less sensitive to noise as the current passes both loops of the shape with opposite directions, naturally canceling the effect of noise. However, those are rarely used due to their shallow depth of investigation (Roy & Lubczynski, 2003).

$$P = I\tau_p \tag{2.1}$$

The most classical experiment records the free induction decay (FID). This experiment consists of the injection of a sequence of excitation pulses at the Larmor frequency

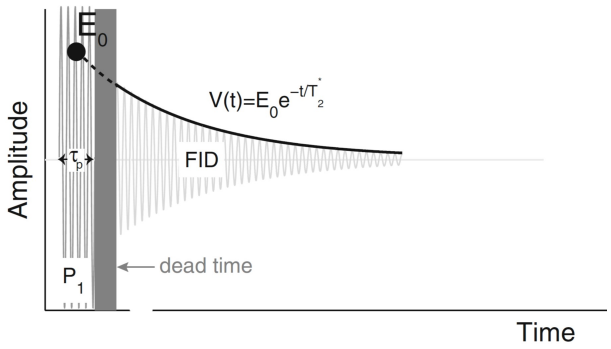

Figure 2.2: FID pulse sequence (From Behroozmand et al., 2015).

(Equation 2.1) varying from tens of As to approximately 10 As with pulse lengths (τ_p) of tens of ms followed by the recording of the NMR response, separated from the injection phase by a dead time (τ_{dead}) of less than 5 ms (Figure 2.2). Each pulse moment probes different volumes, enabling in the end the characterization of the subsurface distribution in water content (linked to the amplitude of the registered signal, E_0 in Figure 2.2) and the relaxation time (linked to the decay of the registered signal) through an inversion process (Chapter 4). From these distributions, it is also possible to retrieve other hydrogeological parameters, such as the porosity or the hydraulic conductivity of the subsurface based on petrophysical relations (Dlugosch, 2014).

After field acquisition, treatment of SNMR data plays an important role for further steps. First of all, the used data consists of the envelope of the FID (black curve in Figure 2.2) and not of the full induced current over time. It is thus required to sample this envelope in accordance with the field parameters. Then, the data is commonly too noisy to be exploited, even if the use of high numbers of stacks reduces the impact of Gaussian noise on the data. It is thus required to apply signal processing to the data to recover a better envelope of the FID. This signal processing generally first consists of despiking (i.e. removing the random spikes that appear in the dataset). Then, depending on the available data (reference loops to record noise or not), a removal of the ambiant noise is performed, either using reference loops (remote reference based noise cancelation) or known harmonics occurring in the dataset (harmonic noise cancelation). For more details on these steps, refer to Müller-Petke et al. (2016).

Examples of processed data are presented in Figures 2.3 and 2.4. In these figures, several aspects of the signal are displayed. The left column presents the signal characteristics for one given pulse moment, whereas the right column shows global characteristics of the experiment. The bottom-left graph represents the signal in frequency domain. This graph is centered on the field-measured Larmor frequency. The resonance of the signal is clearly observable, even if noise is present.

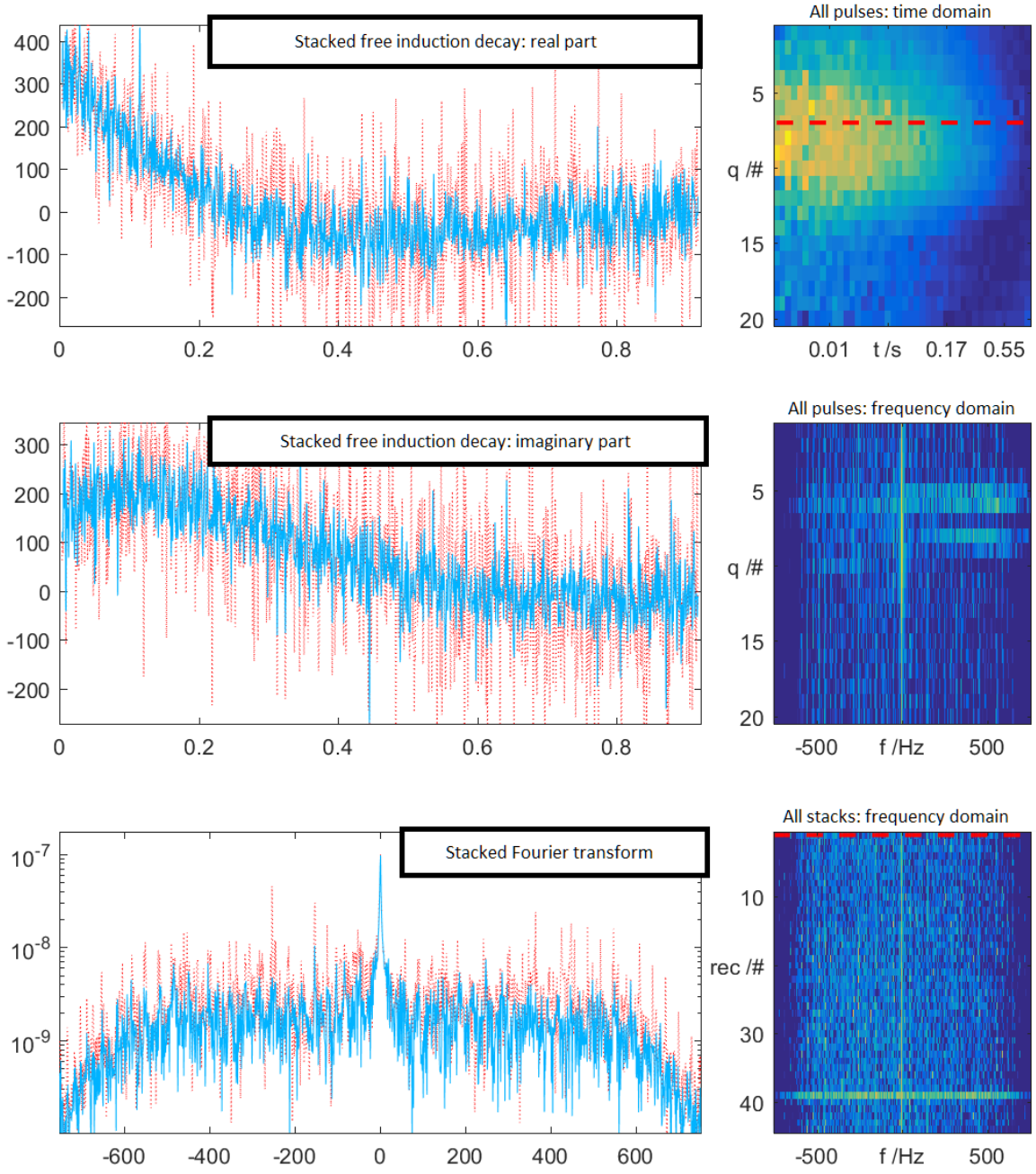

Figure 2.3: Example of noisy signal obtained after signal processing (case of the Schillerslage Tx50/Rx50, see Chapter 7). The blue lines represent the processed data and the red lines the raw data. Those results are obtained using the MRSmatlab tools (Müller-Petke et al., 2016).

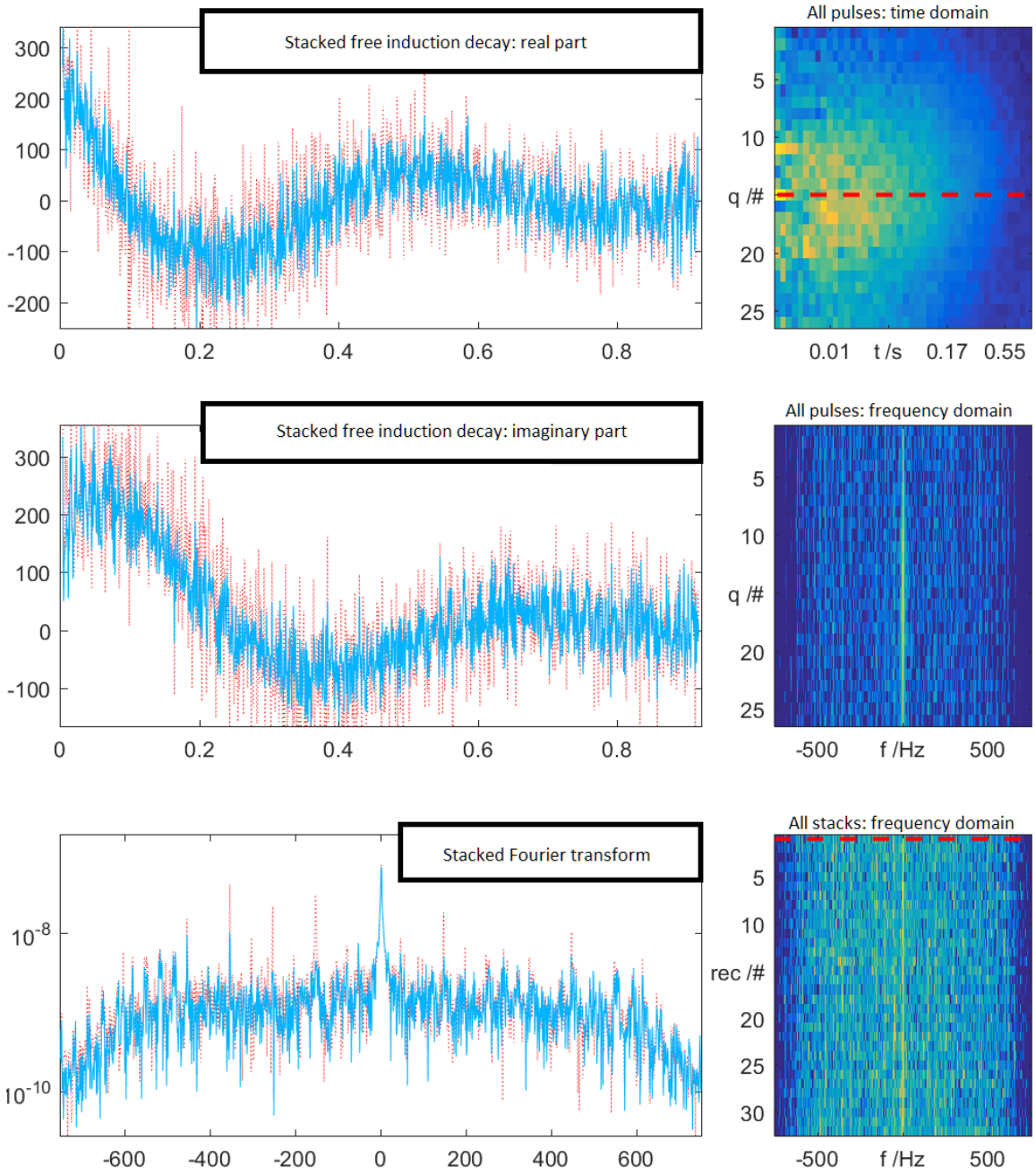

Figure 2.4: Example of noisy signal obtained after signal processing (case of the Schillerslage Tx30/Rx50, see Chapter 7). The blue lines represent the processed data and the red lines the raw data. Those results are obtained using the MRSmatlab tools (Müller-Petke et al., 2016).

Chapter 3

Forward modeling

The induced voltage in a given receiver loop is (e.g., Mueller-Petke and Yaramanci (2010))

$$V(q,t) = \int K(q,\mathbf{r}) \int W(\mathbf{r},T_2^*) \cdot e^{\frac{-t}{T_2^*}} dT_2^* d^3\mathbf{r} \tag{3.1}$$

where:

- $V(q,t)$ is the voltage received in the loop as a function of the pulse moment (q) and the time (t)
- $K(q,\mathbf{r})$ is the kernel function, depending on the pulse moment (q) and the position in space ($\mathbf{r}$)
- $W(\mathbf{r},T_2^*)$ is the partial water content, depending on the position ($\mathbf{r}$) and the relaxation time (T_2^*)

The decay time (t) starts at zero, corresponding to mid the length of the pulse moment (see Figure 2.2).

The kernel function is defined under on-resonance conditions (the excitation frequency is equal to the local Larmor frequency) by Hertrich (2008) and Weichman, Lavely, and Ritzwoller (2000):

$$\begin{aligned} K(q,\mathbf{r}) = \omega_0 M_0 \sin\left(-\gamma \frac{q}{I_0} \left|\mathbf{B}_T^+(\mathbf{r})\right|\right) \\ \times \frac{2}{I_0} \left|\mathbf{B}_T^-(\mathbf{r})\right| \cdot e^{i\left|\zeta_T(\mathbf{r},\omega_0)+\zeta_R(\mathbf{r},\omega_0)\right|} \\ \times \left[\hat{\mathbf{b}}_R^{\perp}(\mathbf{r},\omega_0) \cdot \hat{\mathbf{b}}_T^{\perp}(\mathbf{r},\omega_0) + i\hat{\mathbf{b}}_0 \cdot \hat{\mathbf{b}}_R^{\perp}(\mathbf{r},\omega_0) \times \hat{\mathbf{b}}_T^{\perp}(\mathbf{r},\omega_0)\right] \end{aligned} \tag{3.2}$$

The different parameters in Equation 3.2 are (Behroozmand et al., 2015):

- ω_0 the Larmor frequency (supposed equal to the excitation frequency)
- $\mathbf{r}$ is the position in space of the sample
- M_0 the specific magnetization of hydrogen protons
- γ the gyromagnetic ratio
- q the pulse moment
- I_0 the transmitter loop current
- $\mathbf{B}_T^+$ the co-rotating component of the projected transmitter field into the plane perpendicular to $\mathbf{B}_E$
- $\mathbf{B}_R^-$ the counter-rotating component of the virtual magnetic field from a unit current in the receiver loop projected into the plane perpendicular to $\mathbf{B}_E$
- $\hat{\mathbf{b}}_0$ a unit vector pointing in the direction of $\mathbf{B}_E$
- $\hat{\mathbf{b}}_T^\perp$ and $\hat{\mathbf{b}}_R^\perp$ unit vectors pointing in the direction of the components of $\mathbf{B}_T$ and $\mathbf{B}_R$ perpendicular to $\mathbf{B}_E$ respectively
- ζ_T and ζ_R the phase lags from the transmitter to the sample and from the sample to the transmitter respectively

The full development of Equation 3.2 is presented by Hertrich (2005). In this equation, the first line corresponds to the response of a spin system originating from the exciting pulse. Then, the second part takes into account the sensitivity of the receiver, without signal generation. The last part describes the behavior of the system for separated transmitter/receiver couples. From this equation, it emerges that the time dependency of the SNMR response only appears outside the kernel function. This means that the SNMR problem is linear on water content but not on the full problem.

For the 1-D SNMR experiment, the previous formulations can be simplified by integrating 3.1 along the x and y dimensions. The resulting equation is:

$$V(q,t) = \int K(q,z) \int W(z,T_2^*) \cdot e^{\frac{-t}{T_2^*}} dT_2^* dz \tag{3.3}$$

where $K(q,z)$ is the result of the integration along the x and y dimensions of Equation 3.2.

This latter formulation can be written in matrix form at a given decay time (t) as follows in Equation 3.4 (Mueller-Petke & Yaramanci, 2010). In this formulation, the dimensions n, l, k and m correspond respectively to the number of parameters used for the multi-exponential fit (mono-exponential = 1, bi-exponential = 2, etc.) of the FID, the number

of pulse moments, the number of layers in the discretization of the subsurface along the z-axis and the number of time-steps recorded during the experiment. m_k^n stands for the partial water content at the $k-th$ discretization related to the $n-th$ relaxation time. This latter formulation is the one used for the inversion (Chapter 4).

$$
\begin{bmatrix} V_1^1 \\ V_2^1 \\ \vdots \\ V_l^1 \\ V_1^2 \\ \vdots \\ V_l^m \end{bmatrix} = \left[\begin{array}{ccccccc} K(z_1,q_1)e^{-t(1)/T(1)_2^*} & \cdots & K(z_k,q_1)e^{-t(1)/T(1)_2^*} & K(z_1,q_1)e^{-t(1)/T(2)_2^*} & \cdots & K(z_z,q_1)e^{-t(1)/T(n)_2^*} \\ K(z_1,q_2)e^{-t(1)/T(1)_2^*} & \cdots & K(z_k,q_2)e^{-t(1)/T(1)_2^*} & K(z_1,q_2)e^{-t(1)/T(2)_2^*} & \cdots & K(z_z,q_2)e^{-t(1)/T(n)_2^*} \\ \vdots & \cdots & \vdots & \vdots & \cdots & \vdots \\ K(z_1,q_l)e^{-t(1)/T(1)_2^*} & \cdots & K(z_k,q_l)e^{-t(1)/T(1)_2^*} & K(z_1,q_l)e^{-t(1)/T(2)_2^*} & \cdots & K(z_z,q_l)e^{-t(1)/T(n)_2^*} \\ K(z_1,q_1)e^{-t(2)/T(1)_2^*} & \cdots & K(z_k,q_1)e^{-t(2)/T(1)_2^*} & K(z_1,q_1)e^{-t(2)/T(2)_2^*} & \cdots & K(z_z,q_1)e^{-t(2)/T(n)_2^*} \\ \vdots & \cdots & \vdots & \vdots & \cdots & \vdots \\ K(z_1,q_l)e^{-t(m)/T(1)_2^*} & \cdots & K(z_k,q_l)e^{-t(m)/T(1)_2^*} & K(z_1,q_l)e^{-t(m)/T(2)_2^*} & \cdots & K(z_z,q_l)e^{-t(m)/T(n)_2^*} \end{array}\right] \cdot \begin{bmatrix} m_1^1 \\ m_2^1 \\ \vdots \\ m_k^1 \\ m_1^2 \\ \vdots \\ m_k^n \end{bmatrix} \tag{3.4}
$$

Chapter 4

Inversion methods

From the early developments of the use of SNMR to nowadays, inversion of the corresponding data has largely evolved. At the beginning, the Initial Value Inversion (IVI) (Legchenko & Shushakov, 1998) was used, for its simplicity. Later, the Time Step Inversion (TSI) was introduced (Legchenko & Valla, 2002), involving a better fitting of the signal, and larger parts of the dataset. Finally the QT inversion (the state-of-the-art inversion) was introduced in 2010 by Mueller-Petke and Yaramanci. All those inversion methods differ widely and are based on different schemes/data uses (Figures 4.1 and 4.2). The diverse available inversion methods will be introduced in this chapter, with an emphasize on the state-of-the-art QT inversion.

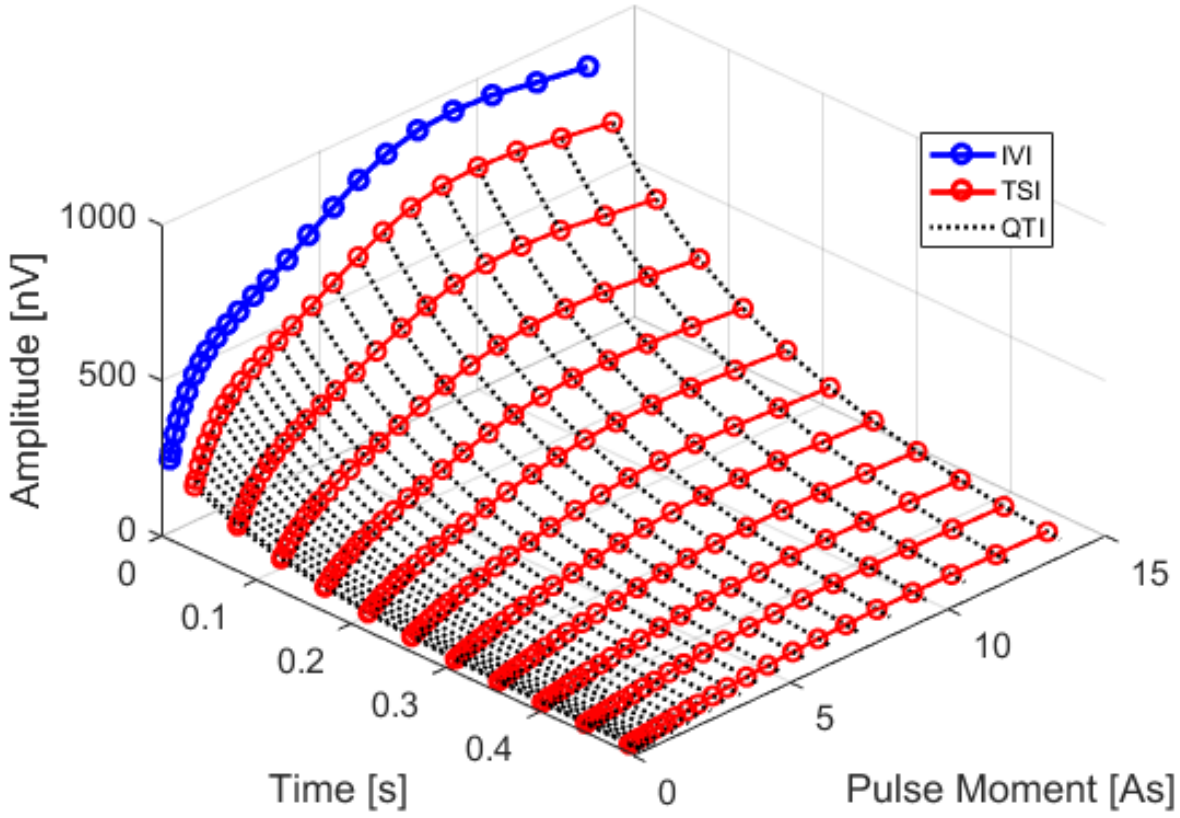

Figure 4.1: Datasets used for the different types of inversions. The blue line represents the initial value dataset, each red line represents one of the independent time-steps datasets and the dashed black lines represent the full QT dataset.

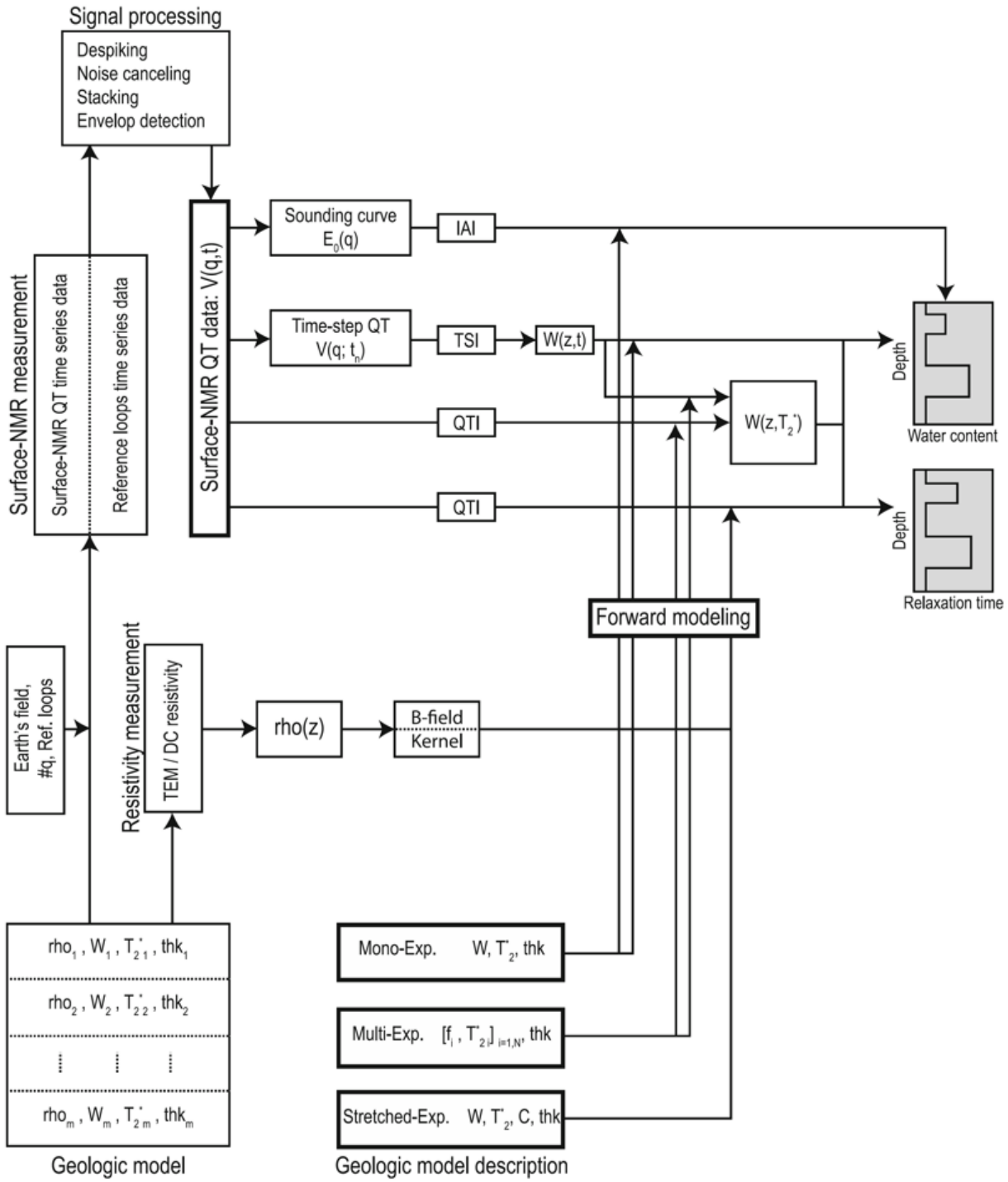

Figure 4.2: Flowchart of SNMR inversion (From Behroozmand et al. (2015)).

4.1 Initial Value Inversion

The Initial Value Inversion (IVI) was introduced in 1998 by Legchenko and Shushakov. It relies on a simplified form of Equation 3.3:

$$e_0(q) = \int_0^L K(q,z) \cdot W(z) dz \tag{4.1}$$

where $W(z)$ is the water content distribution and $e_0(q)$ is the initial amplitude of the signal for a given pulse moment (q). This equation already presents the main weakness of the IVI scheme: it requires the knowledge of the initial amplitude of the signal. However, this value is not measured during the SNMR experiment and, therefore, needs to be estimated (Mueller-Petke & Yaramanci, 2010). This latter operation is performed under the assumption that the exponential decay follows a mono-exponential path.

The linear equation presented in Equation 4.1 can be written in matrix form assuming a given spatial discretization:

$$\mathbf{E}_0 = \mathbf{G}\mathbf{m} \tag{4.2}$$

where $\mathbf{E}_0$ is a vector containing the initial amplitude of the signal for each l pulse moment q, $\mathbf{G}$ is the discrete 1-D kernel function and $\mathbf{m}$ the model (i.e. the discrete water content). With such a system, the inversion is conducted using the generalized singular-value decomposition (GSVD) with Tikhonov regularization (see Mueller-Petke and Yaramanci (2010)).

4.2 Time Step Inversion

The Time Step Inversion (TSI) scheme uses a more complete part of the SNMR QT dataset. It consists in a more complex form of the previously presented IVI. Multiple time steps (t_n) are independently defined and inverted using the exact same method as the one presented for the IVI on each n equation (Legchenko & Valla, 2002; Mueller-Petke & Yaramanci, 2010):

$$\mathbf{E}_{t_n} = \mathbf{G}\mathbf{m}_{t_n} \tag{4.3}$$

This results in a set of water contents $w(z,t)$. Finally, the $w(z,t)$ are used to fit a relaxation time (T_2^*) value for each discrete layer of the subsurface. The proposed fit in Legchenko and Valla (2002) is mono-exponential. Later, Mohnke and Yaramanci (2005) introduced a multi-exponential fit using partial water content ($w(z,T_2^*)$) which provides an exact solution to the 1-D forward model (Equation 3.3).

4.3 State-of-the-art: the QT inversion

The QT inversion uses the full QT dataset originating from field acquisition in order to estimate both water contents (or partial water contents) and relaxation times. It was first introduced by Mueller-Petke and Yaramanci (2010) as a result of a PhD research (Müller-Petke, 2009). As the inversion process uses both time and pulse moment dimensions simultaneously, the problem is very large, hence requiring more advanced inversion schemes. The forward problem under the assumption that the T_2^* corresponds to a smooth distribution (i.e. a discretization of the relaxation time space is specified by the user - default values between 5 and 500 ms with 30 steps) is stated :

$$V(q,t) = \int G(z, T_2^*, q, t) w(z, T_2^*) dT_2^* dz \tag{4.4}$$

The matrix formulation of the 1-D forward modeling is presented in Equation 3.4. The forward operator that is used is the kernel function ($K(q,z)$) developed in Equation 3.2 integrated along the x and y directions of the space and multiplied by e^{-t/T_2^*}. Therefore, it is computed using the 1-D kernel function presented in the matrix form:

$$\begin{array}{c} \\ z_1 \\ z_2 \\ z_3 \\ \vdots \\ z_k \end{array} \begin{array}{c} \begin{array}{ccccc} q_1 & q_2 & q_3 & \cdots & q_l \end{array} \\ \begin{bmatrix} K_{1,1} & K_{1,2} & K_{1,3} & \cdots & K_{1,l} \\ K_{2,1} & K_{2,2} & K_{2,3} & \cdots & K_{2,l} \\ K_{3,1} & K_{3,2} & K_{3,3} & \cdots & K_{3,l} \\ \vdots & \vdots & \vdots & \ddots & \\ K_{k,1} & K_{k,2} & K_{k,3} & & K_{k,l} \end{bmatrix} \end{array} \tag{4.5}$$

Once the forward operator is computed as presented in Equation 3.4, the problem becomes linear. However, due to the use of the full QT dataset, the dimensions of the problem are too large to apply the GSVD solver accepted for the other inversion methods (Mueller-Petke & Yaramanci, 2010). This is the reason why the preferred process relies on a conjugated gradient solver. The minimized functional is:

$$\left| \left(\mathbf{J}^{A,T} \mathbf{\Delta m} - \mathbf{\Delta} \left| \mathbf{V} \right| \right) \right|_2^2 + \alpha^2 \left| \mathbf{L \Delta m} \right|_2^2 \tag{4.6}$$

In this equation, the different parameters are:

- $\mathbf{J}^{A,T}$ the transpose of the Jacobian matrix corresponding to the forward operator $\mathbf{G}$
- $\mathbf{m}$ the model (partial water contents: $W(z, T_2^*)$)
- $\mathbf{V}$ the data containing the amplitude of the signal

- α the regularization parameter
- $\mathbf{L}$ an operator that estimates the first derivative

The applied conjugated gradient least square solver, called **C**onjugated **G**radient **L**east **S**quare solver using **C**onstraints, **D**ata weighting and **P**arametric mapping (CGLSCDP), is presented by Günther, Rücker, and Spitzer (2006) (and fully defined by Günther (2004)). This solver enables to avoid memory issues, which significantly improves the inversion process feasibility.

The algorithm presented by Günther (2004) is used to solve an equation of the type:

$$\left(\mathbf{A}^T\mathbf{D}^T\mathbf{D}\mathbf{A} + \lambda\mathbf{C}^T\mathbf{C}\right)\mathbf{x} = \mathbf{A}^T\mathbf{D}^T\mathbf{D}\mathbf{b} - \lambda\mathbf{C}^T\mathbf{C}\delta\mathbf{m}^k \tag{4.7}$$

where $\mathbf{A}$ is the Jacobian of the forward operator, $\mathbf{C}$ is the constraint matrix and $\mathbf{D}$ is the weighting matrix, $\mathbf{x}$ is the model increment, $\mathbf{b}$ the data and $\delta\mathbf{m}^k = \mathbf{m}^k - \mathbf{m}^0$ the current model compared to the reference (initial) model ($\mathbf{m}^0$). The regularization parameter (λ) is classically determined using the L-curve criterion (Aster, Borchers, & Thurber, 2013).

In the QT inversion, the system is similar, with a perfect correspondence between the code of MRSmatlab (Müller-Petke et al., 2016) and the algorithm proposed by Günther (2004).

The result of the CGLSCDP algorithm is the model gradient. Then, a line search algorithm explores the direct surrounding of this solution to assess the best increment to apply to the model (partial water contents), i.e. a multiple of the computed increment that minimizes the norm of the residuum (Müller-Petke et al., 2016).

When the relaxation time is no longer discrete (i.e. the decay is characterized by one unknown value and not a set of known multiple values associated with unknown partial water contents), the problem becomes non-linear. This is the case when the T_2^* distribution is set to a smooth-mono distribution. In order to resolve this issue, the previously used algorithm remains the same, but the forward operator is recomputed at each step, to converge towards relevant relaxation time and water content distributions. This latter option is the default choice of the MRSmatlab code (Müller-Petke et al., 2016) and is the one used in later developments.

In order to estimate the uncertainty on the obtained distributions, it is possible to use bootstrap resampling (Hertrich, 2008). This method consists of randomly resampling the dataset with a predefined percentage, in order to carry out the inversion with the slightly modified dataset.

Chapter 5

A new approach: PFA imaging

The Prediction-Focused Approach (PFA) is a recent tool used to interpret data. It is part of a broader new way to acquire/interpret data based on statistics called Bayesian Evidential Learning (BEL) (Scheidt et al., 2018). This latter consists in two different parts: pre-acquisition and post-acquisition phases. The first part concerns experimental design issues, whereas the second addresses the prediction of forecast variables from field-acquired data. The prediction-focused approach is the main object of the second part of BEL.

Prediction-focused approach has been introduced in 2015 by Scheidt et al.. It emerges from the need for a better way to assess uncertainty on forecast variables without requiring a large number of full inversion of data with substantial variations. Moreover, the intention of most inverse modeling methods is not especially their results but the ability of those results to generate a prediction. In the proposed approach, Scheidt et al. are generating some models that constitute the prior distribution of models and compute the full forward modeling for all those models. As they describe the method:

"PFA does not require iteration, but rather relies on estimating a direct relationship between the simulated data variables and prediction variables. This analysis requires the creation of prior Earth models to calibrate that relationship, but these Earth models need not match any data." (Scheidt et al., 2015)

The method is further described by Hermans et al. in 2016. In the case presented there, the method uses 6 steps:

1. Generation of prior data and forecasts from the prior distribution
2. Dimension reduction of the data and the forecast variables, using principal component analysis
3. Canonical correlation analysis to establish multivariate correlations between data and forecast variables

4. Gaussian process regression to derive the conditional mean and covariance matrix of the forecast variables in the canonical component space

5. Sampling of the Gaussian model

6. Back-transformation of the samples into original space

In this work, such an approach is applied for the first time to SNMR measurements, with free induction decay (FID) envelope as data, and water content (W) and relaxation time (T_2^*) as a function of depth as forecast variables (Figure 5.1).

In this chapter, the development of the method used to achieve a PFA imaging of SNMR data is detailed. The method is roughly the same as the one developed by Hermans et al. in 2016, but some parts of the process needed to be adapted to achieve a convenient result (Figure 5.1). The principle component analysis applied to the models parameters is inefficient (step 2) and the Gaussian process regression is replaced by a kernel density function (step 4). The different steps defined here are coded in MATLAB (MATLAB, 2016a). The developments of this chapter are discussed in an extended abstract submitted to the "7th International Workshop on Magnetic Resonance" by Michel et al. (2018).

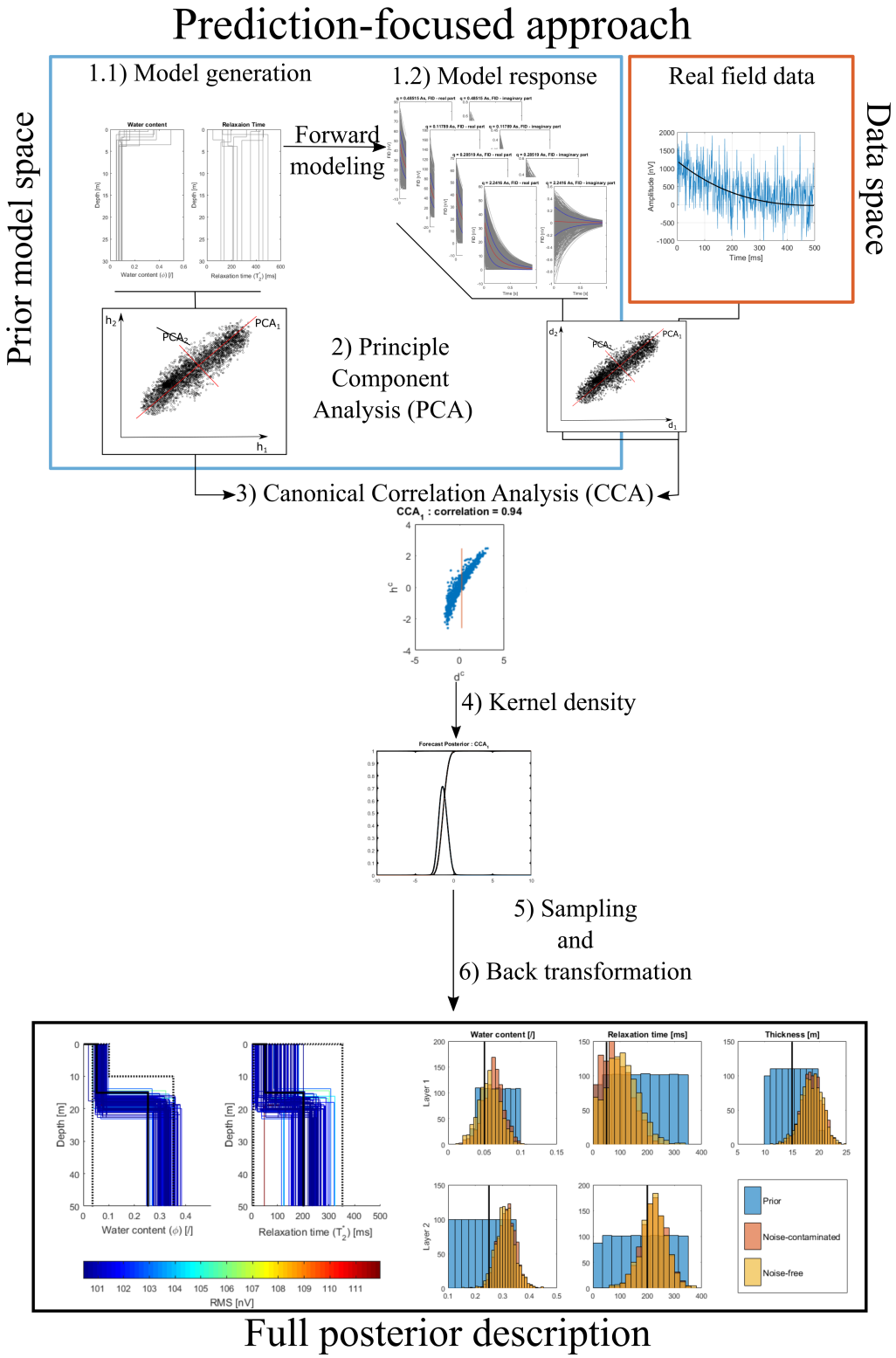

Figure 5.1: Work-flow of the developed PFA imaging process.

5.1 Generation of prior data and models (step 1)

5.1.1 Model generation

The model generation is the first step of the PFA. It consists in creating models with physical parameters that can generate a response according to the same protocol as for the field measurements. In the case that concerns us, multiple possibilities exist to create these prior models. Those are listed below:

1. **A multiple layer model with constant parameters**
   This approach consists in creating models with a given number of layers (generally low, noted N_{layers}) of unknown thickness. For each layer, the parameters are totally independent.
   In this approach, the number of parameters is reduced:

   - The thickness of the layers $(e_i, i = 1, \ldots, N_{layers} - 1)$
   - The water content of the layers $(W_i, i = 1, \ldots, N_{layers})$
   - The relaxation time of the layers $(T^*_{2,i}, i = 1, \ldots, N_{layers})$
   - The resistivity of the layers $(\rho_i, i = 1, \ldots, N_{layers})$

   This results in a total of $4 \cdot N_{layers} - 1$ variables that are independent.

2. **A fixed layered model with varying parameters**
   This approach consists in discretizing the soil into a given number of layers (generally high, noted N_{layers}) of known thickness. In each layer, the parameters are fixed but not totally independent (the idea is to create geologically realistic models). Therefore, the number of parameters is higher, but due to correlations between them, the expected reduction of the dataset should perform better. The parameters are listed below:

   - The water content of the layers $(W_i, i = 1, \ldots, N_{layers})$
   - The relaxation time of the layers $(T^*_{2,i}, i = 1, \ldots, N_{layers})$
   - The resistivity of the layers $(\rho_i, i = 1, \ldots, N_{layers})$

   This results in a total of $3 \cdot N_{layers}$ variables that are correlated with one another (through a variogram for example).

Currently, for the sake of testing the developed method, the retained approach is to use the first type of models with only two layers. Later, the prior model space will be discussed

case-by-case in order to correspond to the best of our prior understanding of the geology on the tested site (Chapter 7). This approach enables to understand the physical relationships between the parameters and the response. For numerical and time limitations, the models have been set with a uniform resistivity along the whole 1-D profile. This hypothesis has been confirmed via a sensitivity analysis (5.7 Sensitivity analysis). Therefore, the exploited model was relatively simple:

- Two layers (therefore, one unknown thickness)
  - The thickness of the first layer is limited to the injection loop diameter
- The water content is separated into two distinct zones
  - The first layer is supposed unsaturated ($W_1 \in [0.035\ 0.1]$)
  - The second layer is supposed saturated ($W_2 \in [0.035\ 0.35]$)
- The relaxation time is independent in both layers ($T^*_{2,i} \in [10\ 1000]\ ms$)

Three options are proposed to randomly generate the model:

- Variables uniformly distributed (*rand* function in MATLAB)
- Variables uniformly distributed with a Latin-hypercube sampler (McKay, Beckman, & Conover, 1979) (*lhsdesign* function in MATLAB)
- Variables normally distributed (*randn* function in MATLAB)
  - The mean is set as the mean of the interval
  - The standard deviation is set as one-fourth of the size of the interval

  This way, 95% of the values taken are inside the predefined interval. On the other hand, the normal distributions had to be truncated to ensure a null probability of negative values for the parameters.

As no prior information was available to justify one choice or another, they have all been tested. It appeared that the Latin-hypercube sampler (McKay et al., 1979) applied on the uniform distribution performed similarly to the "simple" uniform distribution sampler. Therefore, this option has not been explored any further. The difference between the uniform and normal laws is that the uniformly distributed variables give less prior information on the model (the models are evenly spread along all the dimensions), whereas in the Gaussian sampler, most of the models will approach the mean parameters. This latter option, therefore, assumes more prior information to the process than the uniformly distributed sampling procedure.

For the reasons exposed above, it has been chosen to work mainly with uniformly distributed variables (Figure 5.2) rather than with normally distributed ones (Figure 5.3).

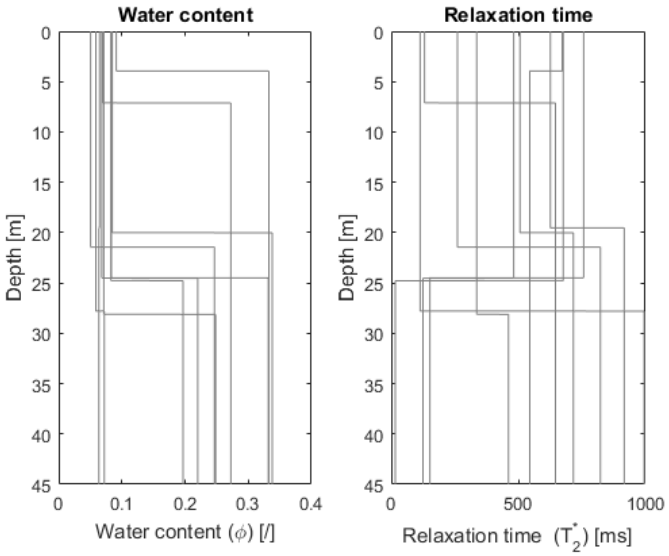

Figure 5.2: Examples of models generated using uniformly distributed variables.

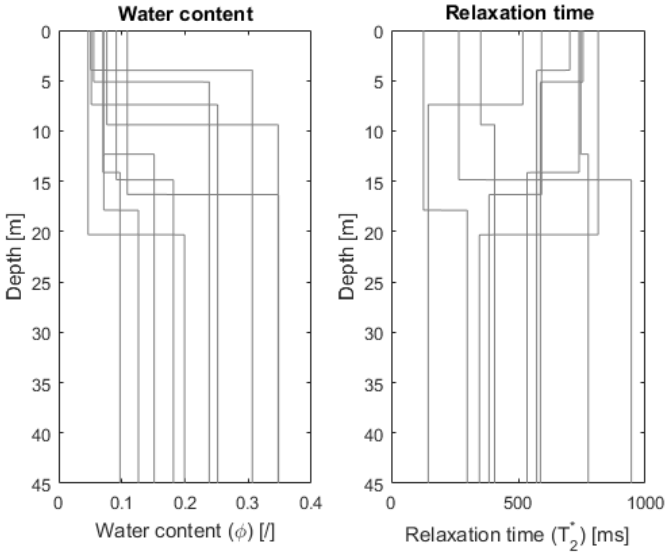

Figure 5.3: Examples of models generated using normally distributed variables.

Type of simulation	Time with constant resistivity	Time with variable resistivity
Single transmitter/ receiver loop	2 minutes	10.5 hours
Receiver outside transmitter loop	5 minutes	2.7 days
Receiver inside transmitter loop	6.5 minutes	4 days

Table 5.1: Estimated computation time for different forward modelings.

5.1.2 Model response

NOTE: The forward modeling as well as the kernel computation is performed using the dedicated functions in MRSmatlab (Müller-Petke et al., 2016).

The forward modeling of the FID response to a typical pulse moment q needs several elements. A first step is to generate the kernels corresponding to the experiment configuration. Then, using the kernels, the direct model is solved for each model. As the kernels only depend on the experiment configuration (size of loops, disposition) and the earth resistivity, it is only needed to compute their value once, as it has been chosen to fix the resistivity to a representative value of $100\Omega.m$. This hypothesis is comforted in the sensitivity analysis performed later in section 5.7 (Sensitivity analysis) and permits a significant gain of computation time. It has been measured that computing the kernels takes from 40 seconds for the simplest case (single transmitter/receiver configuration) to 200 seconds (transmitter inside the receiver loop) or even 350 seconds (transmitter outside the receiver loop) on an Intel i7-6700HQ. Since it has been said that 1000 random models will be simulated, choosing for a variable resistivity in the models will require a huge computation time, as shown in Table 5.1.

In order to correctly simulate the real field experiment, the general configuration of the experiment is retrieved from the "proclog" file generated by MRSmatlab when reading raw data (Müller-Petke et al., 2016). Therefore, the similarity between the configuration of the experiment and the numerical simulations is complete, enabling an efficient comparison between the simulated models and the real data.

Kernels for different configurations are shown in Figure 5.4. The kernels already inform us on the sensitivity of the signal to a given depth. Whereas the 30 m transmitter/30 m receiver configuration shows a sensitivity increasing in depth with pulse moment, the sensitivity to shallow layers is much higher in the two other configurations.

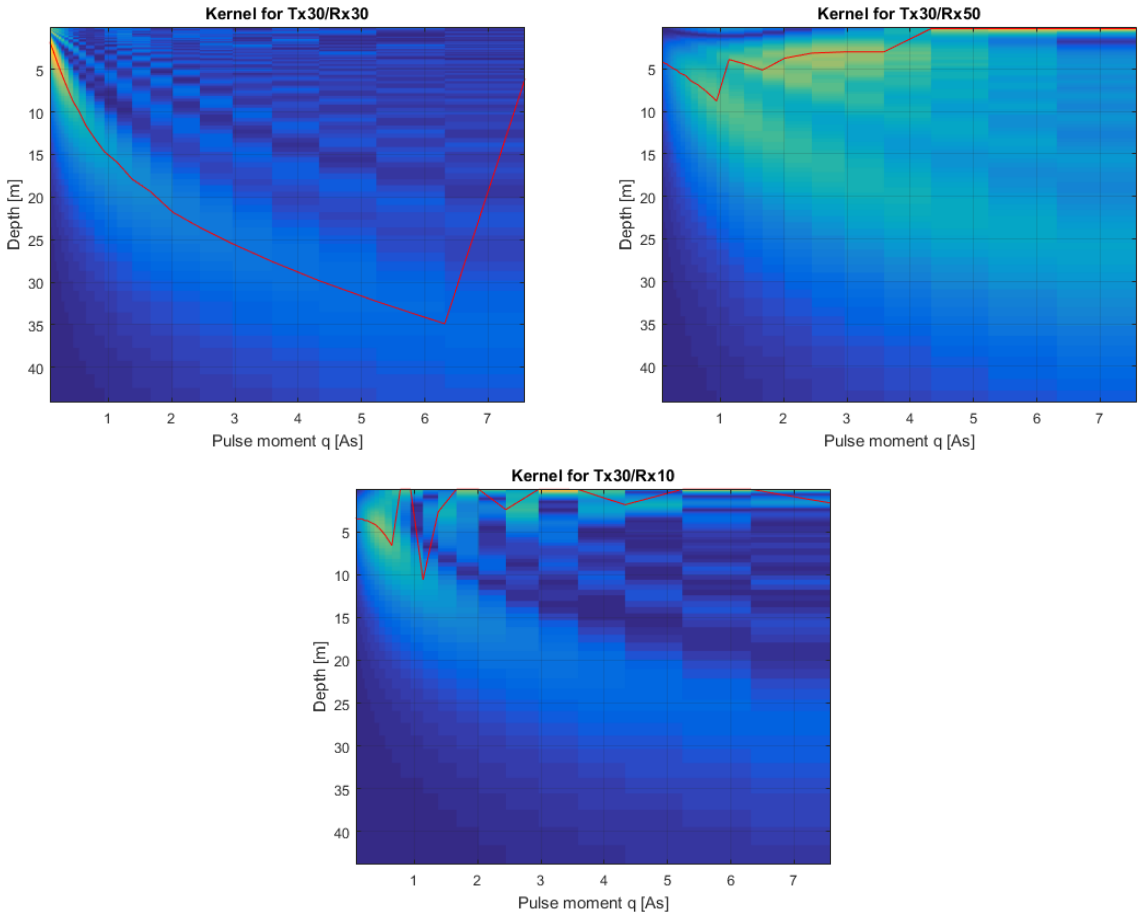

Figure 5.4: Kernels for different experimental configurations: transmitter loop diameter = 30 m and receiver loop diameter = 30 m (top left), 50 m (top right) and 10 m (bottom). The red line represents the maximum of sensitivity.

5.2 Reduction of the dimensionality (step 2)

Now that the different models are computed as well as their associated FID responses (step 1, Section 5.1) the dataset containing the model parameters and the FID response should be reduced. This step is not necessarily mandatory, but it will enable faster computation in the next steps of the process, because it enables to manipulate smaller datasets.

A first reduction of the dataset is performed using a principle component analysis (PCA, *pca* function in MATLAB) (Jolliffe, 2002). PCA seeks for orthogonal dimensions (linear combination of parameters) that maximize the explained variability in the dataset. The first principle components are the ones that describe most of the variability, whereas the last dimensions are the ones of less importance. This procedure has been applied to both the model parameters and the corresponding FID responses (whose real and complex parts

are separated prior to this operation) with mitigated results.

Whereas the PCA performed satisfyingly on the FID part of the problem, enabling a reduction of the dataset, from more than 50 000 dimensions to less than 10, keeping more than 99% of the variation (Figures 5.5 and 5.6), the method appeared less efficient for the model parameters.

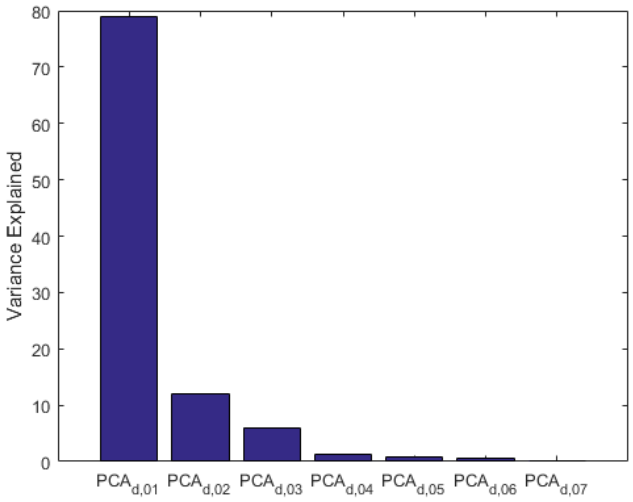

Figure 5.5: Results of the PCA on the FID: explained variance for the most significant dimensions.

From Figure 5.6, it can be observed that the highest load is always given to the first time-step of each pulse moment. This seems logical since the decay of the signal is quite rapid and thus, the main part of the information is found here. Choosing for a level of total explained variance above 99.9%, the initial 74 360 dimensions are explained with only seven principle components.

For the model parameters, the same "raw" process has been applied (Figure 5.7). Whereas no dimension reduction was expected due to the fact that every parameter in the model is significant (see Section 5.7 Sensitivity analysis), apparently, the five dimensions could be reduced to three, still keeping 99.9% of the variance explained. This could have been interesting, even if difficult to understand, but another problem with this process was pointed out: very few loads were given to the water contents, whereas those variables are the main outcomes of the developed process.

The reason for those low loads is probably that the water content values are very small compared to the other parameters. Another approach has thus been tested: the model parameters could be weighted according to the variance observed in each parameter. This method should overcome the low loads given to the low valued parameters. Whereas the low loads problem is significantly resolved using this approach (Figure 5.8), the loads given

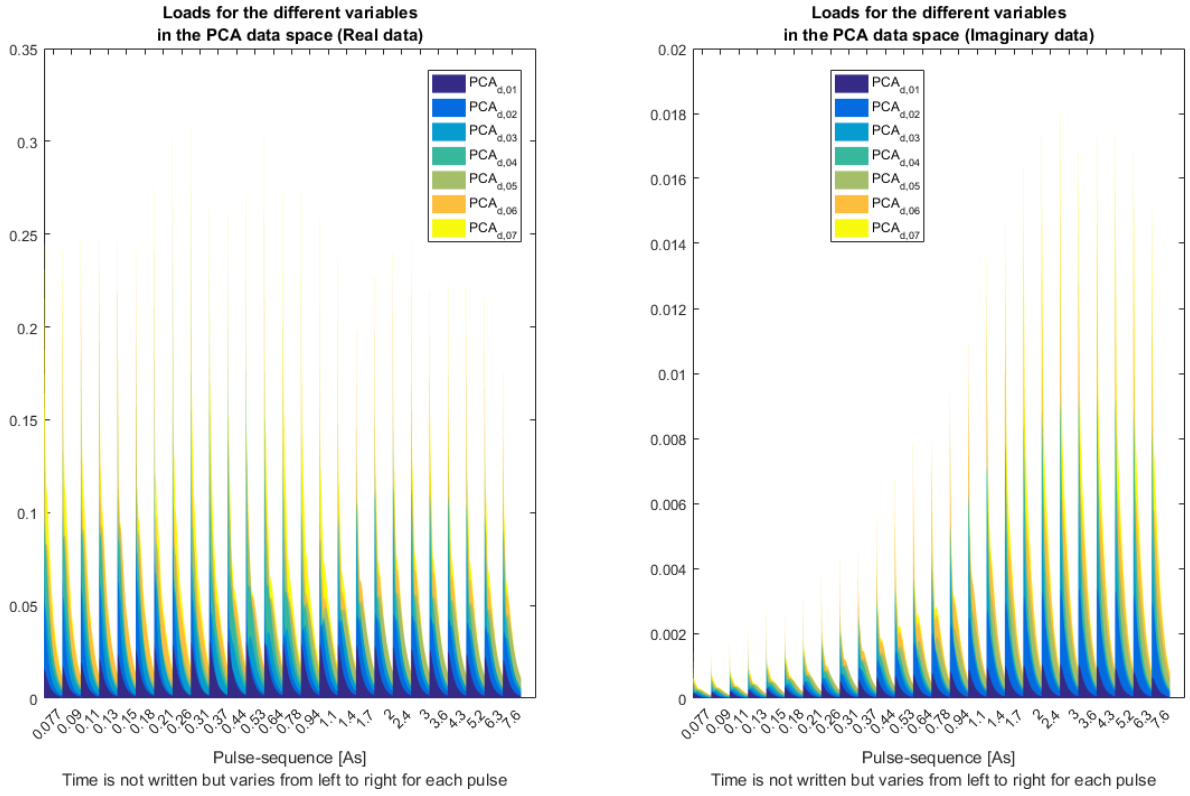

Figure 5.6: Results of the PCA on the FID: loads attributed to the main dimensions.

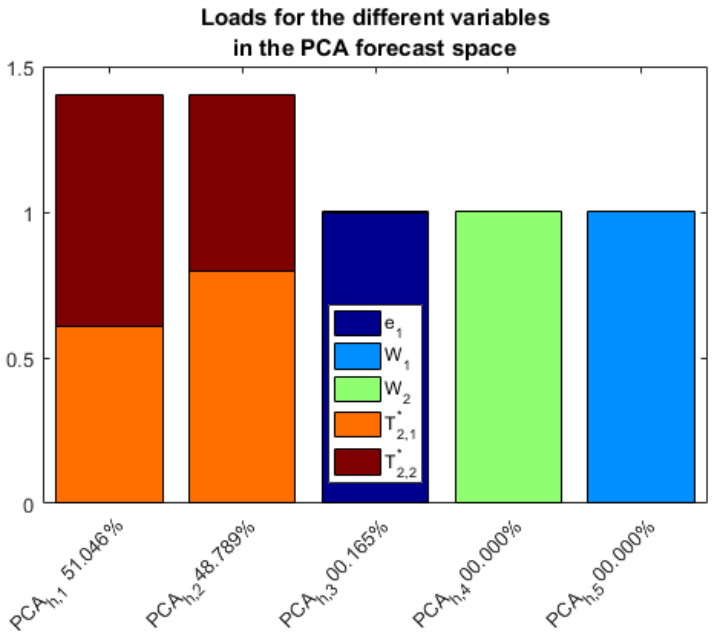

Figure 5.7: Results of the PCA on the model parameters:
loads attributed to the different dimensions.

to the water contents still remain low. Moreover, in order to keep a good level of explained variance, no reduction of the model parameters dimensions could be achieved.

Therefore, the choice has been made not to reduce the dimensions of this part of the problem. This remains possible seeing the very small number of parameters, but could trigger problems in further steps (for example when the other model generation method will be applied (see Section 5.1.1 Model generation)).

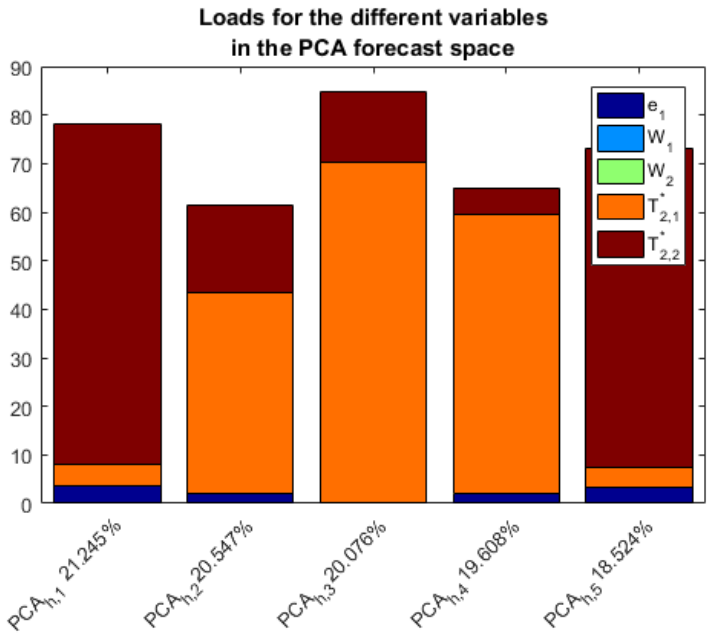

Figure 5.8: Results of the PCA on the model parameters weighted by their variance: loads attributed to the different dimensions.

5.3 Canonical correlation analysis (step 3)

Canonical correlation analysis (CCA, *canoncorr* function in MATLAB, Statistics and Machine Learning Toolbox) seeks for linear combinations of model parameters and data (in our case reduced data from PCA) that maximizes the canonical correlation (ρ^*) between the i-th components of the resulting model space and data space. The global aim is to get reduced variables that can be easily observed. Moreover, sometimes "simple" relationships can be found between the obtained variables (Jolliffe, 2002).

It turns out that in our case, the variables were clearly not associated through a linear relationship, nor were they with a more complicated law. Most of the dimensions of the problem seem to be scattered (Figure 5.9). Whereas a linear (or, at least a simple) relationship could be seen for the first dimensions, for the two last dimensions, a law relating $h^c_{4,5}$ to $d^c_{4,5}$ is impossible to target as the resulting points are scattered all along the space.

As a result, further steps of the PFA imaging had to be adapted to this reality. Instead of using the Gaussian regression model in later steps, which requires a high correlation and a linear trend between the variables, it was chosen to work with a kernel density function. This adaptation is critical for the PFA has it needs to perform satisfyingly, since the whole process relies on the constitution of this statistically-based relationship between the forecasts and the data.

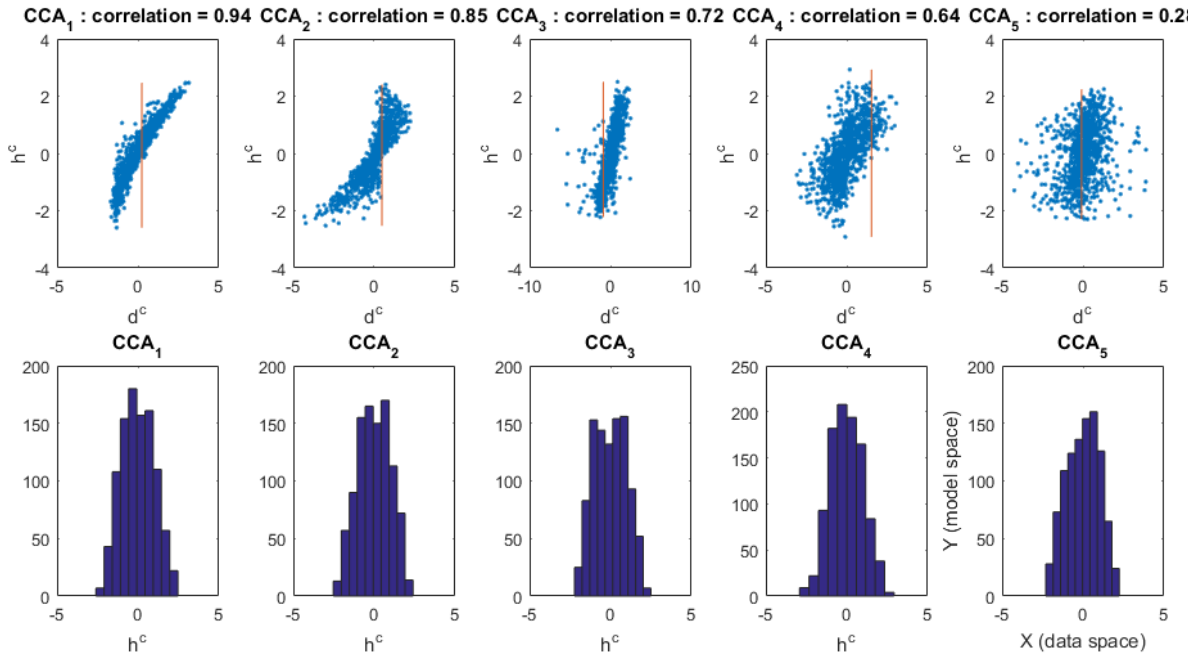

Figure 5.9: Example of results of the Canonical correlation analysis. The orange line represents the benchmark data of this example.

5.4 Constitution of the posterior distribution in reduced space (step 4)

As described in the previous section, the correlation between the canonically correlated variables is somewhat high, but the variables are not linearly linked. This leads to a problem to estimate the posterior distribution using the classical PFA process. Actually, if the variables were Gaussian in model space and the model space could be linked to the data space linearly, it was possible to associate a given value in the data space to a Gaussian distribution in the model space. Moreover, sampling a Gaussian distribution is fast and efficient, which reduces the computing time in further steps. This is the classical way to perform PFA (Hermans et al., 2016).

In our case, as the variables are scattered, it is unaccurate to perform such a computation. Therefore, it has been decided to use the kernel density (*ksdensity* function in MATLAB, Statistics and Machine Learning Toolbox) as a way to approach the posterior distribution . This method transforms a set of points in a 2-D space into a statistical probability density function, assigning to each point a multi-Gaussian distribution (Wand & Jones, 1993). More precisely, the algorithm computes, for a given position in the space, the sum of the contributions of all the points in the dataset. The contribution of each

point is defined as a multi-Gaussian distribution centered on that point. The concept is graphically presented for a 1-D dataset in Figure 5.10. From this 2-D distribution, it is easy to retrieve the conditional distribution of the model space, knowing the value of the field data in the reduced data space.

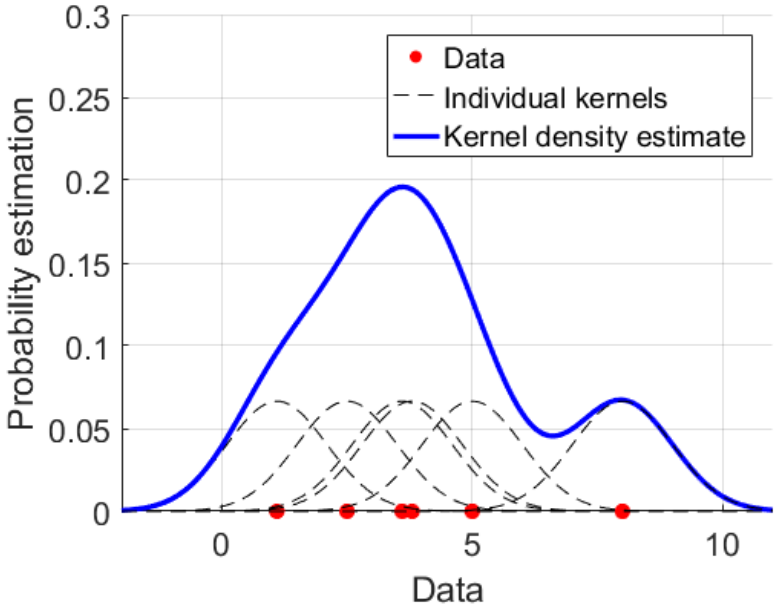

Figure 5.10: Illustration of the kernel density estimation for a 1-D dataset.

As a result, a full discretized probability density function of the posterior model space is obtained (Figure 5.11). This distribution can be Gaussian (as shown in the example) but is not constrained to this shape. This enables to take into account the non-linear aspect of the relationships.

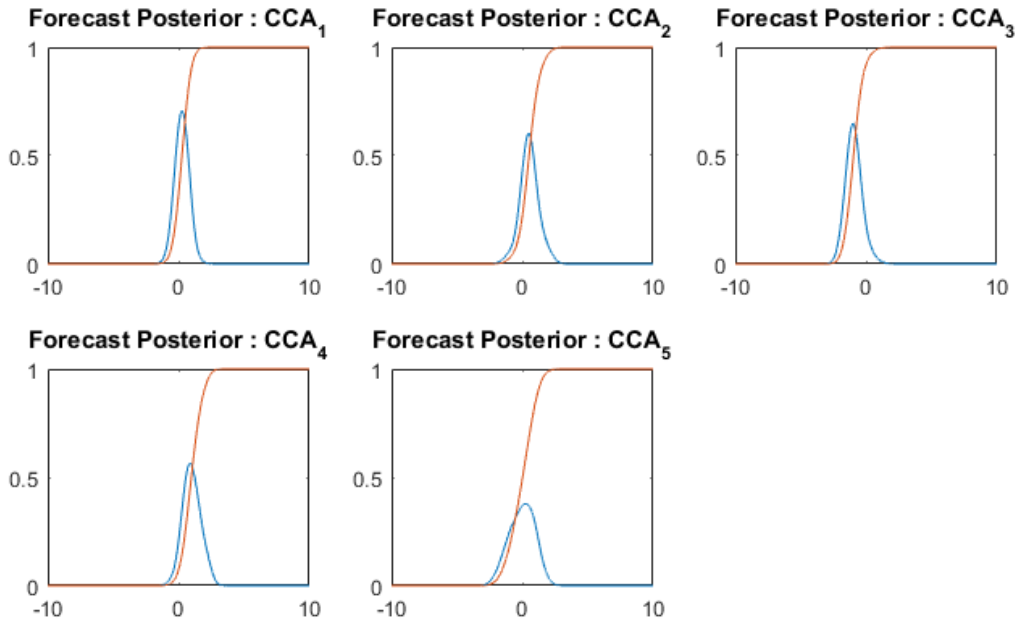

Figure 5.11: Posterior distribution on the canonical correlation space, the probability density function is shown in blue and the cumulative density function is displayed in orange.

5.5 Constitution of the posterior in parameter space (steps 5 and 6)

Then, from the posterior distribution in reduced model space, it is required to find the distribution of the posterior in the initial model space. This is done by sampling the cumulative distribution function associated to the probability density function of the posterior in reduced model space, transforming the obtained values in CCA-model space back into initial model space. This leads to the posterior distribution in model space. This posterior distribution is not restrained to a given shape.

The cumulative distribution function (cdf) defines the probability of a random variable to be below a given value. This probability is between 0 and 1. Hence, sampling the cdf requires to randomly select a value between 0 and 1 (*rand* function in MATLAB) and then, recover the associated value in the cdf (Figure 5.12). Once achieved for all the reduced variables, the obtained set can be related to the original space by using back-transformation.

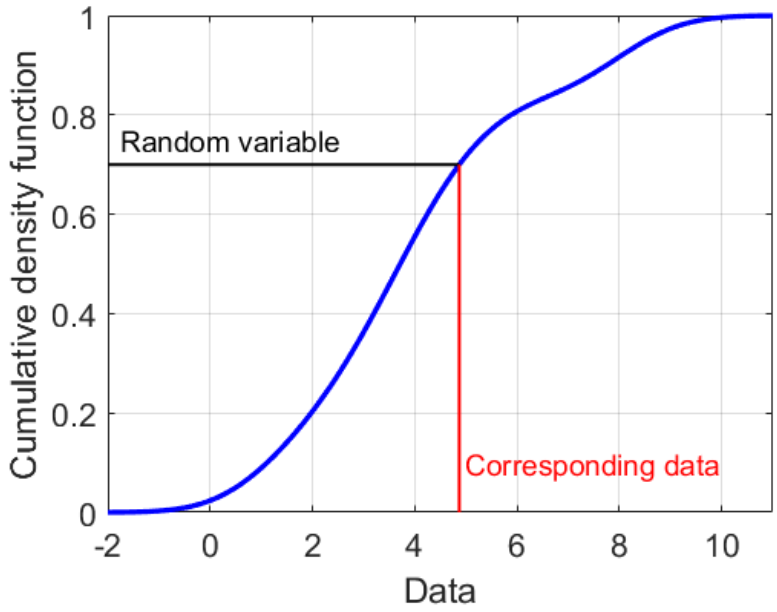

Figure 5.12: Illustration of the sampling process.

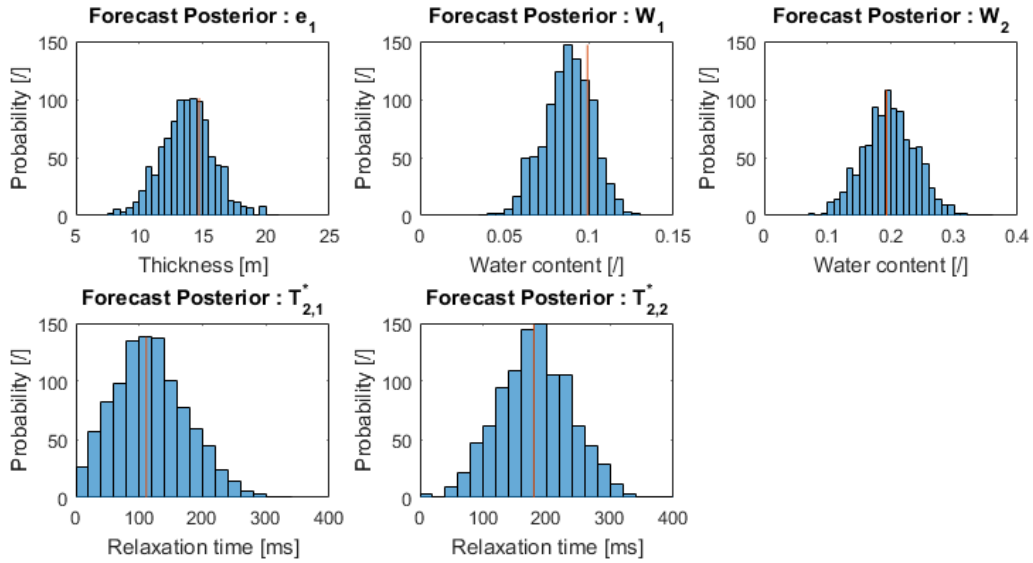

Figure 5.13: Estimated posterior distribution. The benchmark model for this example is represented by the orange lines.

5.6 Analysis of the results

Some models of the posterior model space are not physically consistent. This is due to the kernel density that in fact never reaches null values (a Gaussian distribution tends towards zero far from the mean). As a result, some models from the posterior must be discarded to obtain a physically consistent posterior model space. Globally, this is done by checking that no value of the model parameters is negative (thickness, water content and relaxation time are all defined positive). For mean models (models for which the parameters are in the middle of their possible values), this is not such a problem as few models from the posterior are non-physical, but this may cause issues for more exotic models, which are not especially well represented in the prior distribution.

Finally, the obtained results must be displayed in an efficient way. In order to assess the relevance of each model constituting the posterior, it has been decided to use a forward modeling and to compare the simulated data to the observed data. Although this is not required by PFA, it yields confidence in the obtained results. The root-mean squared (RMS, *rms* function in MATLAB) error is computed for each of the models. Then, all models are presented with a color associated to their RMS. Two examples of such results are presented in Figures 5.14 and 5.15.

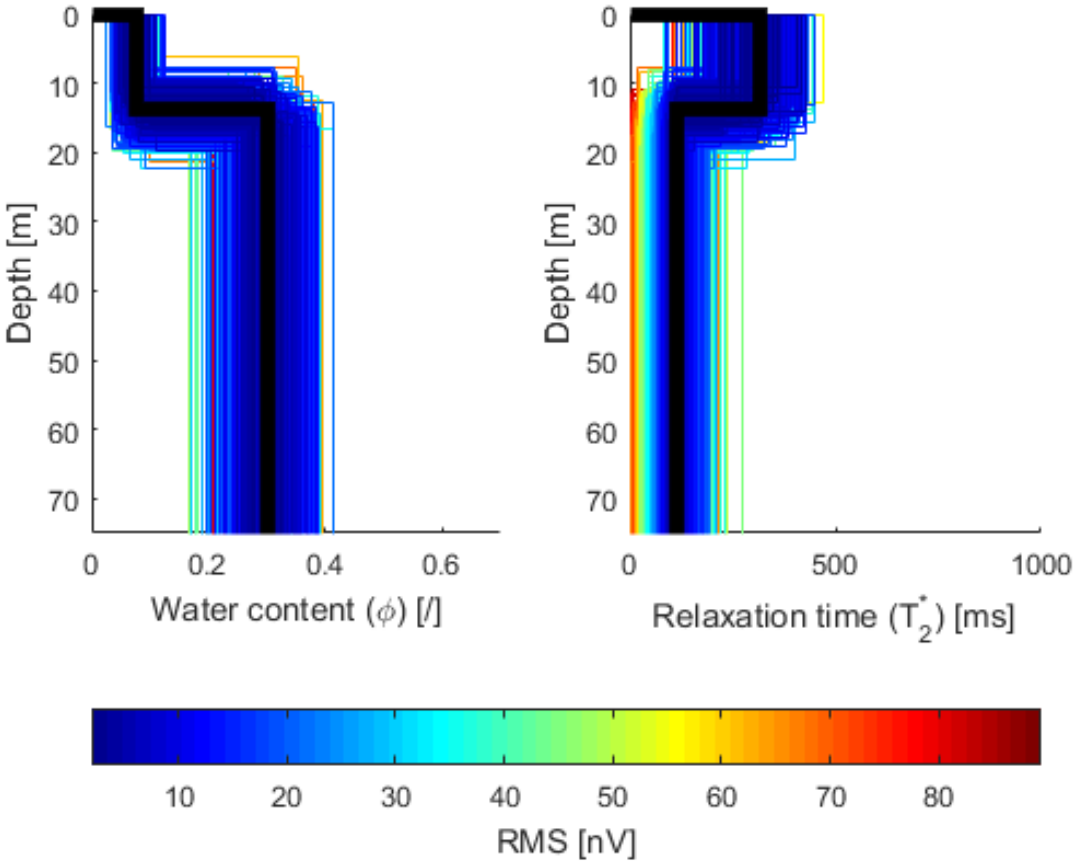

Figure 5.14: Estimated posterior distribution, user-friendly display (Example of model 96 out of 1000). The benchmark model for this example is represented by the black line.

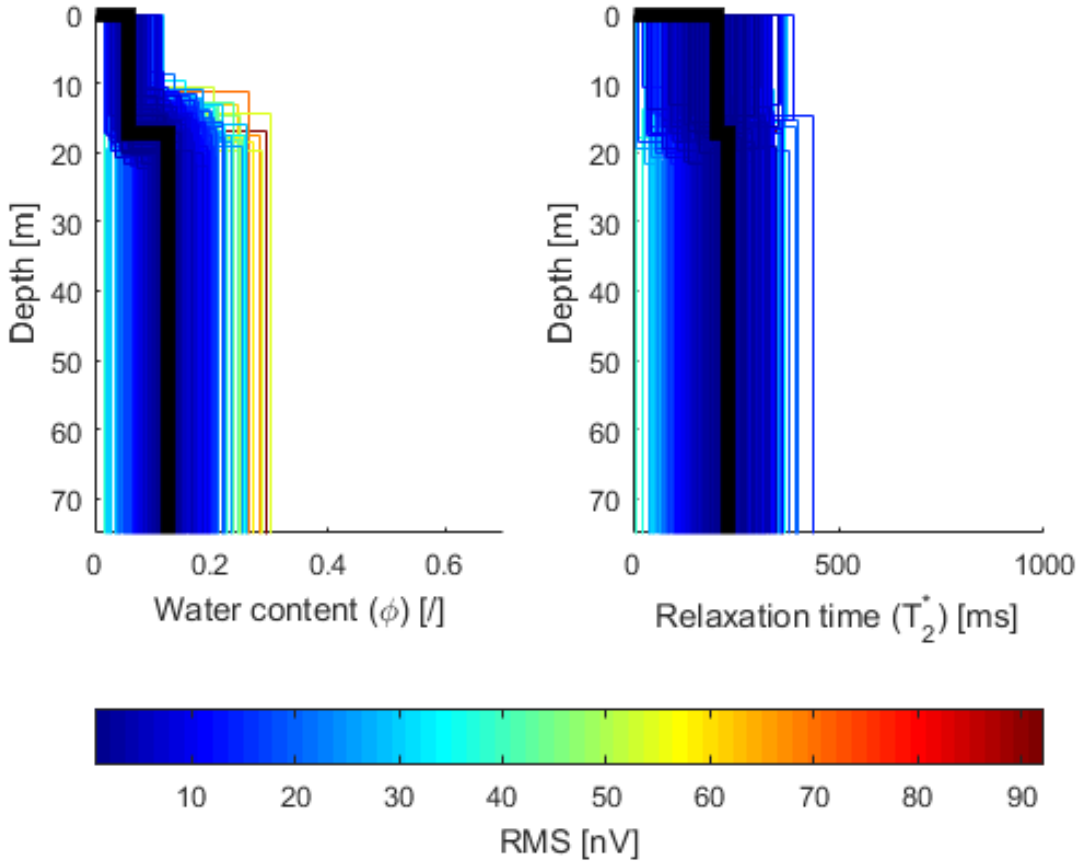

Figure 5.15: Estimated posterior distribution, user-friendly display (Example of model 446 out of 1000). The benchmark model for this example is represented by the black line.

5.7 Sensitivity analysis

AS multivariate sensitivity analysis has been performed using the *DGSA (Distance based global sensitivity analysis)* MATLAB toolbox provided by Stanford University (Park, Yang, Satija, Scheidt, & Caers, 2016) at: `https://github.com/SCRFpublic?tab=repositories`. This toolbox enables the multivariate analysis of the sensitivity of a response to a given parameter using a distance based sensitivity analysis. The method is built on clustering of models into groups that differ in response. Then, the distance between those groups is evaluated and summarized into a Pareto index (Park et al., 2016).

Multivariate sensitivity analysis concerns the first part of BEL on experimental design, ensuring that an experiment is sensitive to the parameters of interest (Scheidt et al., 2018). Since experimental design was not the main objective of this work, this part on the sensitivity analysis is mainly an introduction to the methodology. The sensitivity analysis will be conducted on synthetic 2-layer models with multiple loops configuration. It is introduced in this section, since the different configurations presented in the real case field study (Section 7.3) are explored for an illustrative purpose.

As a result from this sensitivity analysis, made on all the six responses to a model (two possible transmitters and three receivers), the impact of a variation in a parameter is explored, both individually as well as conditionally.

From Figure 5.16, one can observe that the order of significance of each parameter is nearly always the same:

$$T^*_{2,1} > W_1 > e_1 > W_2 > T^*_{2,2}$$

Despite some differences between the scenarios, a general rule is that the characteristics of the first layer always influence the results in a very significant way, whereas the FID response is less sensitive to the second layer characteristics. Nonetheless, except in the case with a 30 m transmitter/receiver where the water content of the second layer is less influencing (important parameter), the whole set of parameters are classified as critical. This classification is performed regarding the localization of the Pareto bars compared to the confidence interval (Park et al., 2016).

Globally, one can also observe that the sensitivity to in-depth parameters decreases when the receiver loop is smaller. This is logical since the depth of investigation is empirically linked to the loop diameter.

When analyzing the combined effect of the different parameters, the DGSA toolbox displays what is called a "Bubble plot". Those so-called bubble plots present both the main effect due to a parameter, as well as its conditioned/conditioning aspect. The size of the bubbles indicates the main effect, whereas the relative distance of bubbles indicates their interaction, either as a conditioning parameter (purple bubbles) or a conditioned

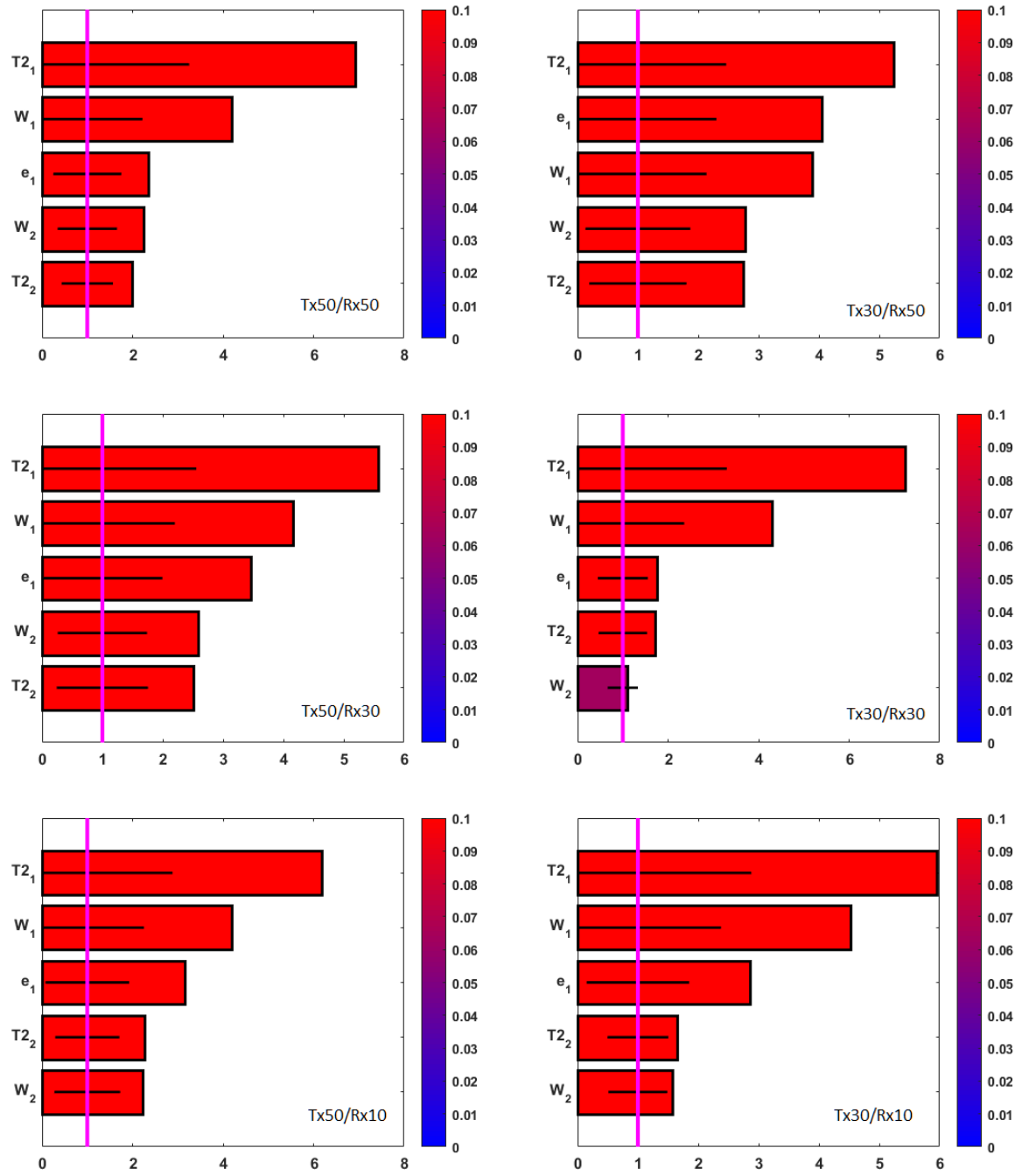

Figure 5.16: Pareto plots with confidence bars for the different experimental scenarios: 50 m transmitter loop (left column) and 30 m transmitter loop (right column), with a 50 m (first row), 30 m (second row) and 10 m (last row) receiver loop.

parameter (green bubbles) (Park et al., 2016). Those graphs are presented in Figure 5.17.

In Figure 5.17, its is shown that the combined effects are mainly observed between parameters defining the first layer. On the other hand, no conditioning (or conditioned) effects are observed between the second layer parameters. This is probably due to the limited sensitivity of the models to those parameters. Another observation is that the main effects are larger when the transmitter is the same as the receiver.

As a conclusion, the FID response is mainly controlled by the shallow part of the ground (as a reminder, the first layer is defined here with a maximal thickness corresponding to the diameter of the transmitter loop). This was already deduced from the computed kernels (Figure 5.4 in section 5.1.2 Forward modeling) where the kernels showed lower values in depth, especially for the in/out-loop configurations. Conditioning and conditioned effects seem relatively similar, inducing a probable symmetry in the system.

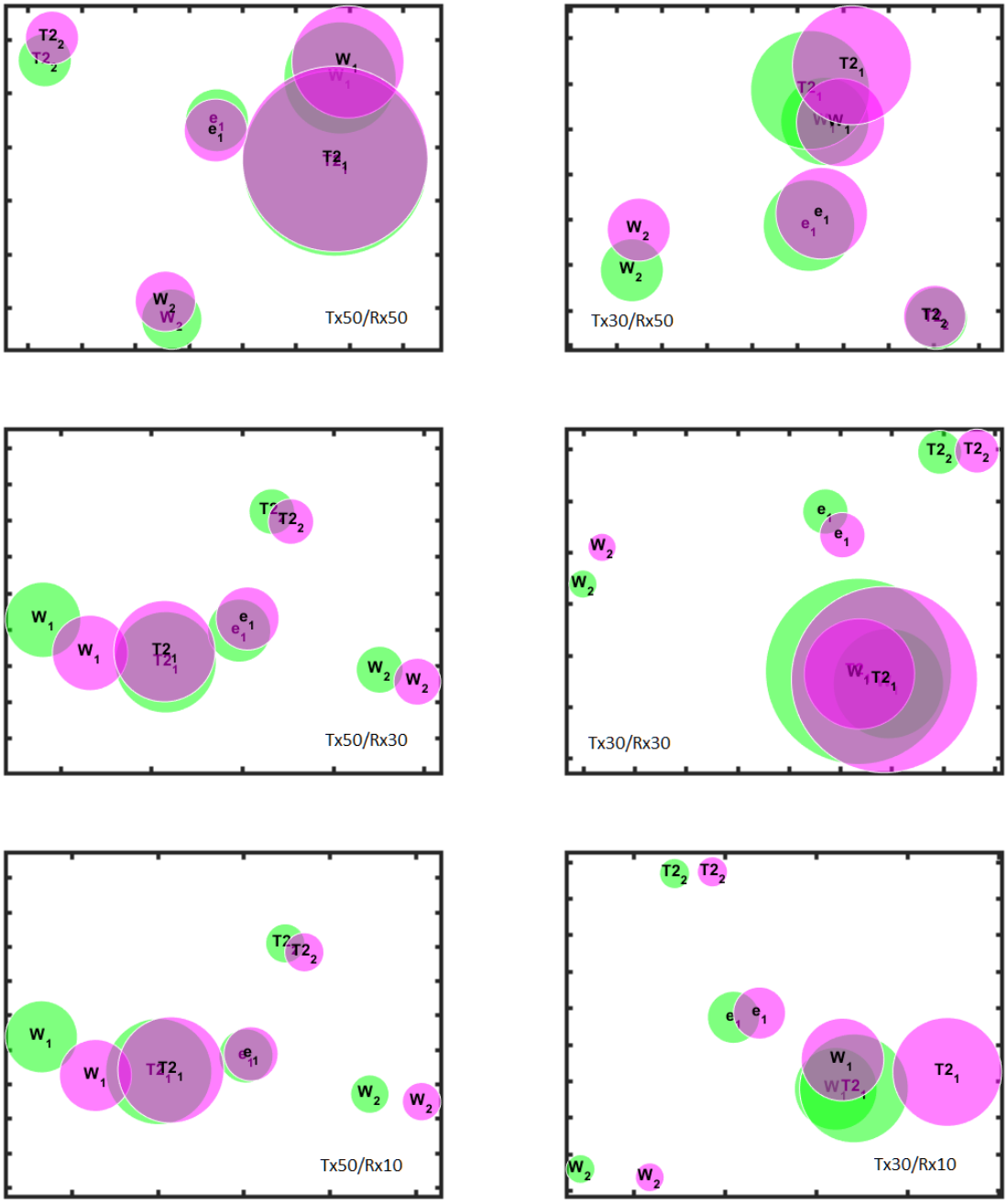

Figure 5.17: Bubble plots for the different experimental scenarios: 50 m transmitter loop (left column) and 30 m transmitter loop (right column), with a 50 m (first row), 30 m (second row) and 10 m (last row) receiver loop.

5.7.1 Sensitivity to resistivity

As mentioned before, it has been chosen, mainly for computing time reasons, that the resistivity of the synthetically generated models should neglect variations in resistivity. This enabled a relatively fast computation of the forward modeling and seemed to provide acceptable results. Nonetheless, this hypothesis needs to be comforted. Therefore, the sensitivity analysis exposed in the previous part has been applied to the case where the transmitter loop has a 50 m diameter and is the same as the receiver loop, but this time with the resistivity that may change in a given, large, interval ($\rho \in [50 \dots 1000]\ \Omega.m$). The forward modeling has been performed in order to get a FID response corresponding to all those models.

The results showed that the FID response was not significantly impacted by resistivity changes, nor was it by combined effects (Figure 5.18).

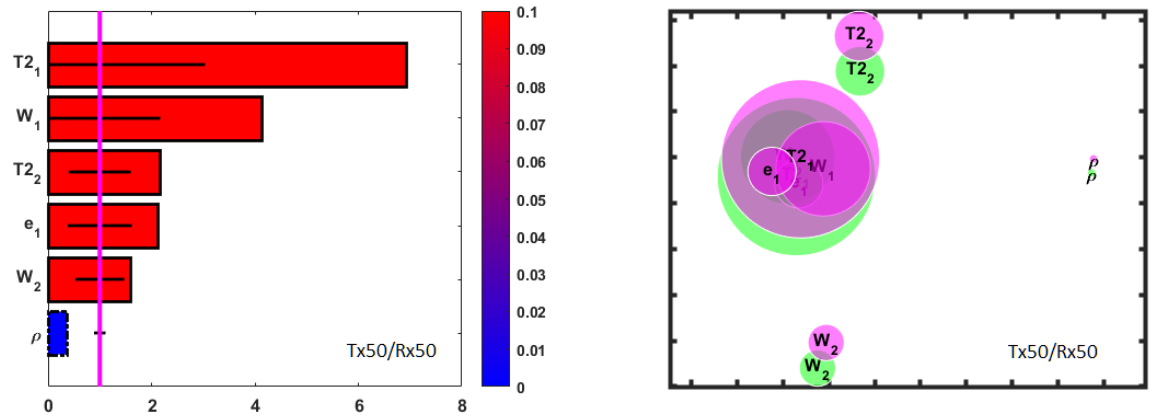

Figure 5.18: Sensitivity analysis of FID response to changes in model resistivity. The left graph presents a Pareto plot with the main effect of all parameters independently, whereas the right graph shows the combined effects.

The left graph in Figure 5.18 clearly shows that the main effect of the resistivity is very small, in absolute value as well as compared to other parameters sensitivity. The right graph proves, on the other hand, that there are no interactions between ρ and the other parameters.

Chapter 6

The multi-central loop configuration

In 2016, Behroozmand et al. published a paper establishing the bases for the use of coaxial receiver loops in the acquisition of SNMR data (for 1-D soundings). In the article, they showed that the use of central loops was beneficial, especially in the improvement of the signal-to-noise ratio. With numerical and field examples, they showed that the central loop lead to similar or stronger sensitivities compared to the classically exploited coincident loops, when accounting for noise. Moreover, a stronger sensitivity to the shallowest part of the soil was noticed for higher pulse moments. However, it was also demonstrated that the use of central loops achieved lower depth resolutions.

From those observations, Kremer et al. (2018) proposed a possibility to benefit from the advantage of such configurations to their full extent. The proposed idea suggested that, instead of only using the data originating from the central loop to retrieve information on the groundwater distribution, it could be interesting to explore the use of multiple coaxial loops in a bigger dataset that contains both coincident and central loops. The use of outer coaxial loops was also proposed. This new method allows to maximize the acquired information in one field, permitting the combined use of multiple datasets with different sensitivities. Figure 6.1 graphically shows this sensitivity advantage, without taking into account the fact that the inner-loops datasets are subject to lower noise levels. It is clear that the merged case has the highest sensitivity.

However, to properly benefit from the increased sensitivity of those multiple datasets, it is required to adapt the QT inversion process, the weighting of the data originating from different loops, as well as the used bootstrap algorithms. Among those three issues, only the first one will be discussed in this work.

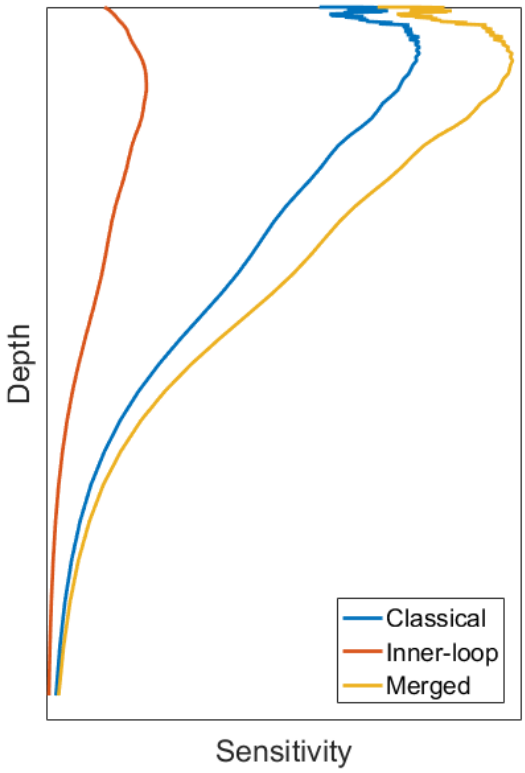

Figure 6.1: Illustration of the sensitivity gain from the use of the multi-central configuration. This gain is purely retrieved from the sensitivity kernels and therefore does not take into account the gain originating form the signal-to-noise ratio improvement.

6.1 QT inversion for multiple loops SNMR data

The adaptation of the QT inversion method requires to specifically assemble the kernels and the datasets. This needs to be consistently performed, as each adaptation in the kernels definition will impact the datasets format and reversely. In this section, the adaptations of the kernels and the datasets are stated.

6.1.1 Assembly of kernels

It has been previously shown that the kernel and the data are linearly linked (if the time dependency is properly expressed, see Chapter 3). Therefore, the assembly of data/kernel is straightforward, but attention needs to be paid to the actual computability of the kernels with extended models, in the case of small receiver loops combined with large transmitter loops.

As a reminder, the time-independent kernels for a unique receiver are in the form presented in Equation 6.1.

$$\begin{array}{c} \\ z_1 \\ z_2 \\ z_3 \\ \vdots \\ z_k \end{array} \begin{array}{c} \begin{array}{ccccc} q_1 & q_2 & q_3 & \cdots & q_l \end{array} \\ \begin{bmatrix} K_{1,1} & K_{1,2} & K_{1,3} & \cdots & K_{1,l} \\ K_{2,1} & K_{2,2} & K_{2,3} & \cdots & K_{2,l} \\ K_{3,1} & K_{3,2} & K_{3,3} & \cdots & K_{3,l} \\ \vdots & \vdots & \vdots & \ddots & \\ K_{k,1} & K_{k,2} & K_{k,3} & & K_{k,l} \end{bmatrix} \end{array} \tag{6.1}$$

The form is exactly the same for the cases where the loop acts as a transmitter and a receiver and when the loop only acts as a receiver. To adapt the kernels to multiple receiver loops, one should only use the other loop as a new set of pulse moments (q_i). The issue with such an approach is the fact that, in order to be consistent, the depth model must be exactly the same for all kernels, since the merged kernels that result from the assembly only takes one depth model (z_j) into account.

This issue results in a trade-off between depth information and shallow layers discretization. Actually, problems occurred when trying to compute the kernel values for cases with large transmitter/small receiver configurations (or the reverse). The values are too small to be stored within machine precision, which leads to errors in the integration process for in-depth values. It is therefore required to limit the depth to an acceptable level, constrained by the smallest receiver loop. This limits both the available information in depth and possibly the accuracy of the results, due to the ignorance of the possible response from in-depth water. As shown by Kremer et al. in 2018, the main advantage of the multi-central

configuration is observed when searching for shallow boundaries; therefore, this problem should not represent such an issue in the next steps.

Nonetheless, it is required to quantify the maximal investigated depth as a function of the experimental configuration. To do so, multiple experimental configurations have been tested, from basic cases (relatively similar transmitter and receiver loops) to extreme configurations with opposite sizes for receivers and transmitters (all in the range between 5 and 150 meter diameter). The maximal depth for the model discretization has been chosen as a multiple of the size of the transmitter loop.

An attempt was made to compute the kernels for each case presented in Table 6.1 with the pulse moments corresponding to a given specific experiment. If the kernel was successfully computed (i.e. MATLAB did not return an error), it was recorded as a success (1) and, on the other hand, if the computation failed (i.e. MATLAB returned an error), it was registered as a fail (0).

d_{Rx} [m]	From 5 to 150 by steps of 5
d_{Tx} [m]	From 5 to 150 by steps of 5
Multiplier [/]	From 0.1 to 2.0 by steps of 0.1

Table 6.1: Parameters for the search of kernel computability.

As a result of this exploration, it turns out as expected that the extreme cases were the most problematic (Figure 6.2 and Appendix A for more details). In further steps, it will thus be required to check the computability of the kernel previously to any computation. As the computability of the kernel is dependent on the loops configurations but also on the sequence of pulse moments chosen, which can vary from one experiment to another, it is impossible to assess the computability of kernels only from the loops configuration (which would only require a simple verification in a previously acquired matrix). A converging algorithm needs to be applied.

This algorithm simply tries to compute the kernel until the deepest useful position (typically $1.5 \times d_{TX}$) and if the computation fails, the number of layers of the earth model is diminished. The suppression of the last layers decreases the actual depth computed until computation is possible. Then, the uncomputed layers are replaced by zero values. In short:

1. Set the maximal depth (classically $1.5 \cdot d_{TX}$) for the global model discretization.
2. Try to compute the kernel with this z model.
   (a) If the computation succeeded:
      i. Exit loop
      ii. Replace all uncomputed values by zeros

(b) If the computation failed:

i. Remove the last layer of the discrete z model.

ii. Repeat from item 2.

With this method, we enable the use of very large transmitter loops (hence, large perturbed zones) coupled with small receiver loops, without limitations on the depth computed for the kernel.

Finally, the assembled time-independent kernels are of the form presented in Equation 6.2. In this equation, the indices n, k and l_i correspond respectively to the number of transmitters/receivers couples, the number of layers in the discrete model and the number of pulse moments of the i-th transmitter/receiver couple. Thus, the component K_k^j, i corresponds to the value of the discrete time-independent kernel for the i-th pulse moment of

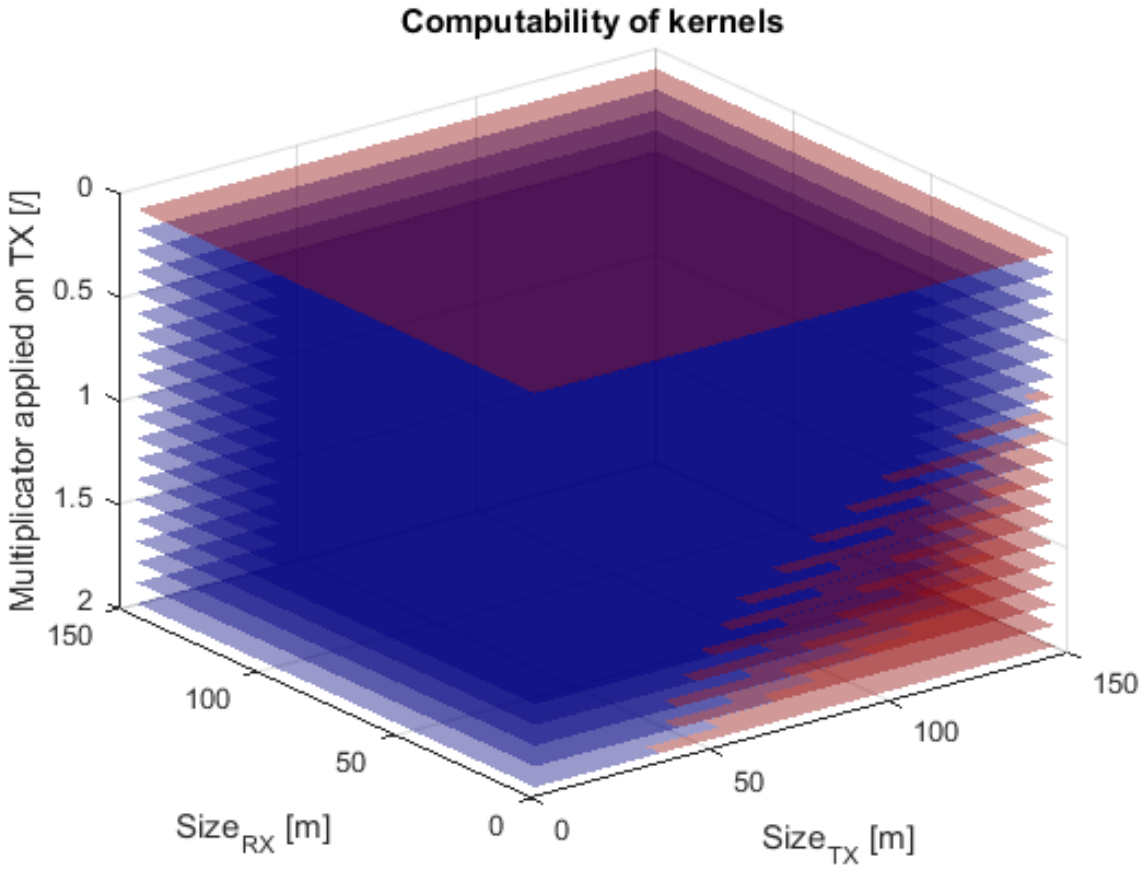

Figure 6.2: Computability of the kernels for different experimental configurations. Blue represents kernels that are computable and red, kernels that are not computable. For more details, see Appendix A.

the j-th transmitter/receiver couple at the k-th layer of the discrete model.

$$\begin{array}{c} \\ z_1 \\ z_2 \\ z_3 \\ \vdots \\ z_k \end{array} \begin{array}{c} \begin{array}{ccccccccccc} q_1^1 & \cdots & q_{l_1}^1 & q_1^2 & \cdots & q_{l_2}^2 & \cdots & q_1^n & \cdots & q_{l_n}^n \end{array} \\ \begin{bmatrix} K_{1,1}^1 & \cdots & K_{1,l_1}^1 & K_{1,1}^2 & \cdots & K_{1,l_2}^2 & \cdots & K_{1,1}^n & \cdots & K_{1,l_n}^n \\ K_{2,1}^1 & \cdots & K_{2,l_1}^1 & K_{2,1}^2 & \cdots & K_{2,l_2}^2 & \cdots & K_{2,1}^n & \cdots & K_{2,l_n}^n \\ K_{3,1}^1 & \cdots & K_{3,l_1}^1 & K_{3,1}^2 & \cdots & K_{3,l_2}^2 & \cdots & K_{3,1}^n & \cdots & K_{3,l_n}^n \\ \vdots & \ddots & \vdots & \vdots & \ddots & \vdots & \vdots & \vdots & \ddots & \vdots \\ K_{k,1}^1 & \cdots & K_{k,l_1}^1 & K_{k,1}^2 & \cdots & K_{k,l_2}^2 & \cdots & K_{k,1}^n & \cdots & K_{k,l_n}^n \end{bmatrix} \end{array} \tag{6.2}$$

6.1.2 Assembly of data

As the assembly of kernels simply uses new transmitter/receiver couples as if they were new pulse moments, the merging of data needs to be performed under the same assumption. Therefore, the data is formatted as if each transmitter/receiver couple acted as a set of new pulse moments. The assembled data is presented in Equation 6.3, where the $\mathbf{V}_i^j$ represents vectors containing the data of the i-th pulse moment of the j-th couple transmitter/receiver.

$$\begin{bmatrix} \mathbf{V}_1^1 \\ \vdots \\ \mathbf{V}_{l_1}^1 \\ \mathbf{V}_1^2 \\ \vdots \\ \mathbf{V}_{l_2}^2 \\ \vdots \\ \mathbf{V}_1^n \\ \vdots \\ \mathbf{V}_{l_n}^n \end{bmatrix} \tag{6.3}$$

6.2 PFA imaging adaptations for multiple loops

The PFA imaging algorithm is adaptable to multiple loops data. It only requires to format the data specifically, in order to merge the different datasets in a way that could enable multiple transmitters/receivers to be taken into account. This adaptation is similar to the one performed in the assembly of data made for the QT inversion. Actually, each pulse moment from a given loop can be assumed as if it was a pulse moment from the experiment, as soon as the corresponding kernel is correctly computed. As the computation of the

kernels does not need the same discretization for each couple, contrarily to the adaptation of the QT inversion algorithm, no particular attention is drawn on this last point.

The adaptation of the algorithm leads to some issues. The fact that multiple datasets are merged leads to significantly larger memory needs for the storage of the simulated free induction decays from the numerous models used. The principle component analysis on the data also requires a significant amount of random access memory (RAM). Therefore, the specifications of the computer happen to be very important. My computer (Intel Core i7-6700HQ CPU and 8Gb of RAM) was barely sufficient for the computation of the posterior distribution using the PFA algorithm on the Schillerslage dataset (Chapter 7, Section 7.3). Hence, further research could be necessary to reduce the memory used during computation.

Chapter 7

Results

This chapter will present different results obtained with the PFA and the multiple loops configurations. At first, synthetic models are explored. As the PFA imaging developed in this work was never applied to SNMR data (and thus, to multiple loops configurations as well), a large part of this section will be dedicated to confirmation of the exposed process. To do so, a benchmarking is proposed on synthetic models and their associated data. The use of the process on noise-free data will be explored. Then, the effect of the addition of Gaussian noise to the datasets will be tested, and a synthetic model with noise will be studied. Finally, a synthetic multiple loops example will be investigated. This example will be interpreted using both the QT inversion and the PFA imaging, in order to demonstrate the advantage of the proposed configuration.

Later, a first real dataset will be explored. This dataset corresponds to a simple two-layer model, which makes it easy to analyze. The interpretation will be performed using both the QT inversion and the PFA imaging.

Finally, both processes are applied to a real multiple-loop dataset acquired at a hydrogeological test site (Germany), where previous deterministic inversions have been conducted (Dlugosch, 2014).

7.1 Synthetic

In this section, synthetic examples are proposed to test the QT inversion method as well as the PFA imaging, as exposed in Chapter 5. Since the QT inversion has already been proven efficient in multiple synthetic and real scenarios in the case of simple configurations (see, for example, Müller-Petke (2009), Yaramanci and Müller-Petke (2009), Grombacher and Auken (2018) or Dlugosch (2014)), no synthetic data on classical configurations were interpreted using the latter. The PFA imaging needs to be validated for the interpretation

of SNMR data and its efficiency to retrieve well-known models.

Therefore, this section mainly proposes a statistical analysis of numerous results on synthetic simple-loops SNMR data interpretation with 2-layer and 3-layer models. Moreover, a synthetic example is exposed and explored in its full complexity, containing data from one single transmitter but three receivers. This last example will be analyzed using both the QT inversion and the PFA imaging.

7.1.1 Benchmarking PFA for SNMR using synthetic models and data

7.1.1.1 Use on synthetic noise-free data

To begin with, no noise was applied in order to test the applicability and the efficiency of the obtained results on very simple models. This has been done on 2-layer and 3-layer models.

One thousand models randomly generated have been tested. Those models are sampled into a uniformly distributed prior model space. The first layer (between 10 and 20 meters thick) has a low saturation (water content between 3 and 10%) and the second layer is saturated (water content between 10 and 35%). The relaxation time ranges from 5 to 350 ms for both layers. The different results were then assessed using the RMS on modeled data (Figure 7.1).

The first analysis that has been performed aims at observing the different representative RMS values. Those consist of the percentiles 5, 25, 50, 75 and 95 (Figure 7.1). The higher the percentile, the larger the spreading of the RMS values. Whereas the RMS values for the 5^{th} percentile are all between 4.46 and 16.19 nV, with a range of 11.73 nV, the 95^{th} percentile shows values ranging from 29.18 to 81.59 nV (i.e. a total range of 52.41 nV).

One could thus search for a reason for the goodness of the fit (low or high RMS values). From the methodology that has been applied, extreme models should lead to worse results, due to the lack of models in this part of the model space. Consequently, a definition of eccentricity had to be set. Eccentricity could be defined both in model space and in data space.

In the model space, eccentricity should be defined as a function of the whole set of parameters, which means that different units will be mixed. Thus, a conversion to dimensionless values should be performed first. As an outcome of this, a definition of eccentricity

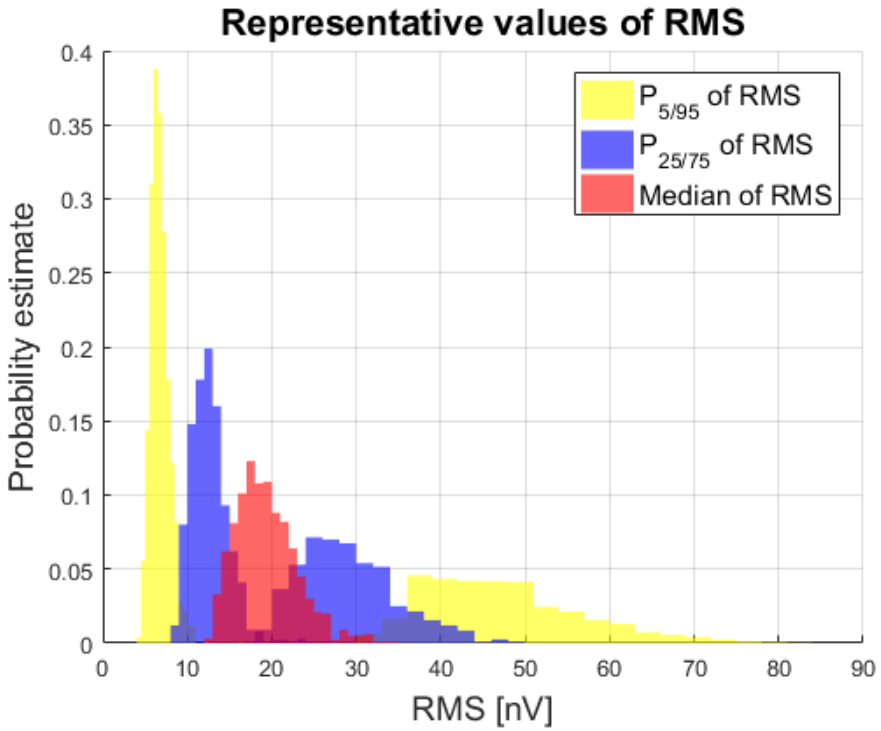

Figure 7.1: Estimated probability density functions of the representative RMS values for all 1000 models (2-layer model).

in model space is set to the expression:

$$E_h = \left|\frac{e_1 - \overline{e_1}}{1\ m}\right| + \left|(W_1 - \overline{W_1}) \times 100\right| + \left|(W_2 - \overline{W_2}) \times 100\right| + \left|\frac{T^*_{2,1} - \overline{T^*_{2,1}}}{10\ ms}\right| + \left|\frac{T^*_{2,2} - \overline{T^*_{2,2}}}{10\ ms}\right| \tag{7.1}$$

The same definition can be constructed for eccentricity in data space. In this case, the dimensionality issue does not exist and the definition can simply be:

$$E_d = \int_0^{t_{register}} \left[FID(t) - \overline{FID}(t)\right] \tag{7.2}$$

In equations 7.1 and 7.2, each parameter (or value) is compared to the mean value ($\overline{value}$). Therefore, a model that lies in the middle of the space will get a low eccentricity and vice-versa.

In order to better understand the following developments, a model has been randomly chosen among the 1000 explored and is always displayed in black above all the other models

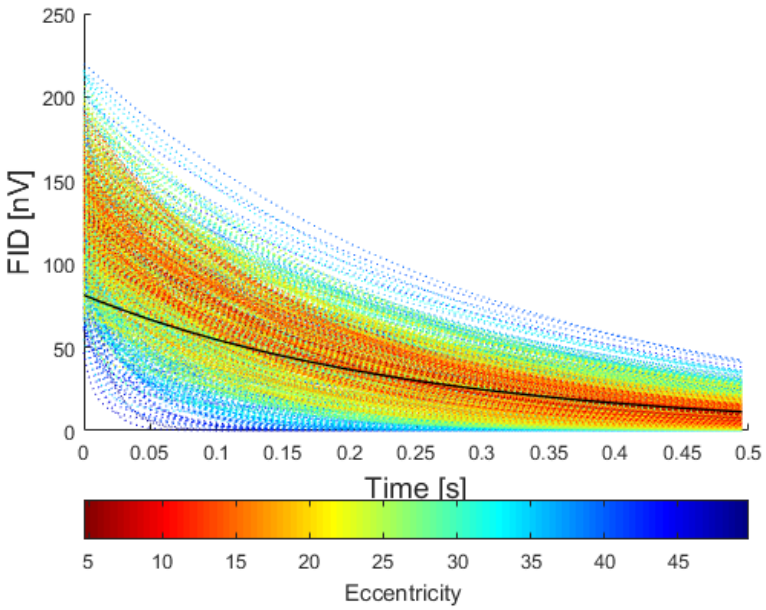

Figure 7.2: Effect of eccentricity in model space (h) on localization of FID (data space d).

in the graphs (Figures 7.2 to 7.8). This model is only displayed for continuity but has no particular features.

In a first attempt to understand the behavior of PFA imaging, Figure 7.2 shows that the least extreme models (warmer colors) are the ones that are close to the median data. On the opposite side, high eccentricity tends to lead to either very slow or very rapid decays (cooler colors). However, this is not seen in the scatter plot representing eccentricities in model space versus data space (Figure 7.3).

The influence of those eccentricities on the RMS values is then explored. Scatter plots showing the RMS percentiles versus the eccentricities as defined above are presented in Figures 7.4 and 7.5. The correlations between eccentricities and RMS are always low. This means that, even if a model is extreme, both in model and data space, this does not necessarily lead to a bad resolution of the problem. On the other hand, one can observe that, for the highest percentiles (namely 75, 95 and 100), the models that get the largest RMS values are systematically in the upper part of the graphs, which means they correspond to extreme models. This can be expressed as follows: badly resolved models correspond to extreme models, whereas the opposite is untrue.

In terms of correlation, it seems that eccentricity in the data space achieves better correlations with RMS values than the eccentricity in the model space. This is logical since the RMS error is relative to the data misfit, defined in the same units as the data. Although higher, these correlations are still below significant levels for correlations.

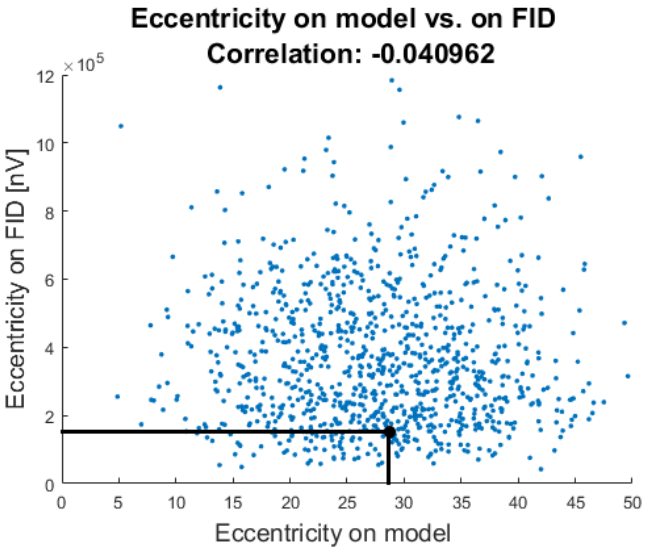

Figure 7.3: Effect of eccentricity in model space (h) on eccentricity in data space d.

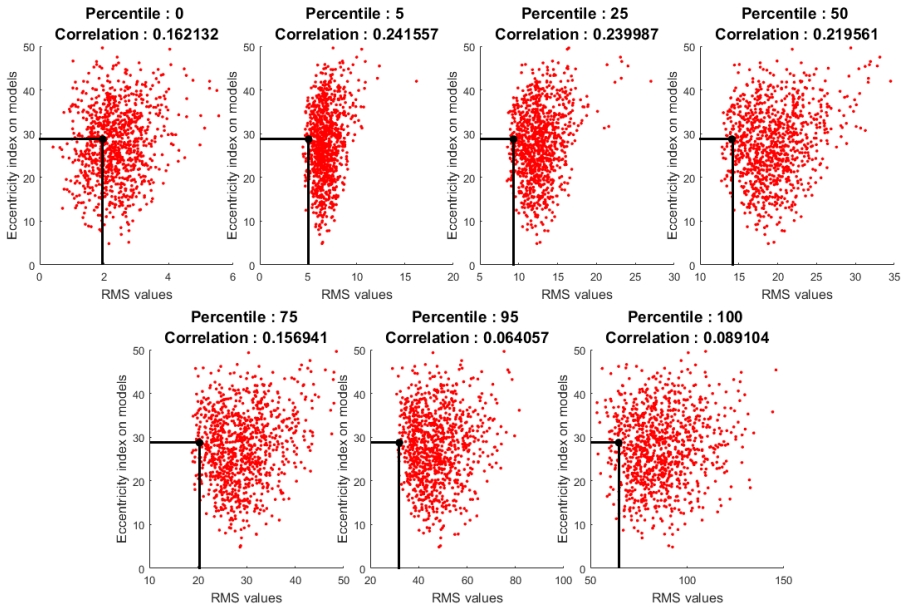

Figure 7.4: Effect of eccentricity in model space (h) on the goodness of the results (2-layer models).

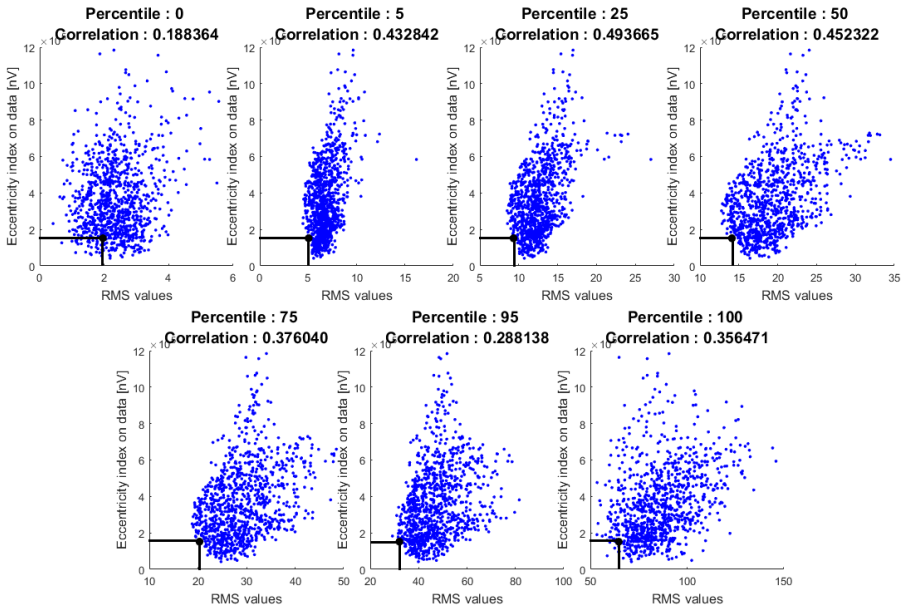

Figure 7.5: Effect of eccentricity in data space (d) on the goodness of the results (2-layer models).

The same analysis has been performed with data originating from 3-layer models. Globally, the results were very similar, with no statistical evidence that the methodology performed worse on one category than on the other.

Whereas the RMS values for the 5^{th} percentile are still reasonable, with values ranging from 5.47 to 18.27 nV, it is observed that those values are slightly higher than in the 2-layer case. The 95^{th} percentile is on the other hand very similar in the 2-layer and in the 3-layer cases with values ranging from 31.32 to 74.70 nV. Taking the extreme values originating from the process does not provide evidence of similarities but the 10^{th} and 90^{th} percentile of the 95^{th} percentile showed that the ranges are very similar in the two explored cases.

The same analysis as the one performed with the 2-layer models has been applied. It turns out that the link between extreme models and bad resolution is slightly lower than in the previous case. This means that even models that are located in the middle of the model space could be badly resolved (see Figure 7.7). The same conclusion can be reached when analyzing the graphs presenting the effect of eccentricity in data space on RMS (Figure 7.8): badly resolved models do not necessarily mean that the model is extreme in data space.

All those results imply a possible issue with the exposed process: the model space is not sufficiently explored. As the number of layers increase, the number of parameters increase as well. This means that, with the same number of models randomly sampled from the model space, fewer parts of the space are explored. To overcome this possible impediment,

one could use a larger model space sampling.

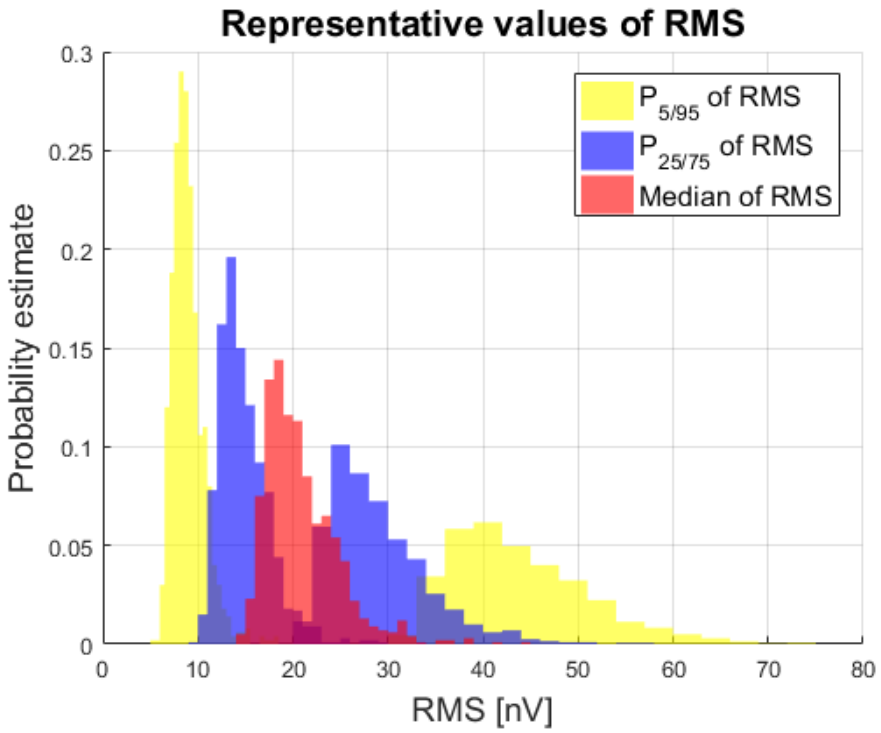

Figure 7.6: Estimated probability density functions of the representative RMS values for all 1000 models (3-layer models).

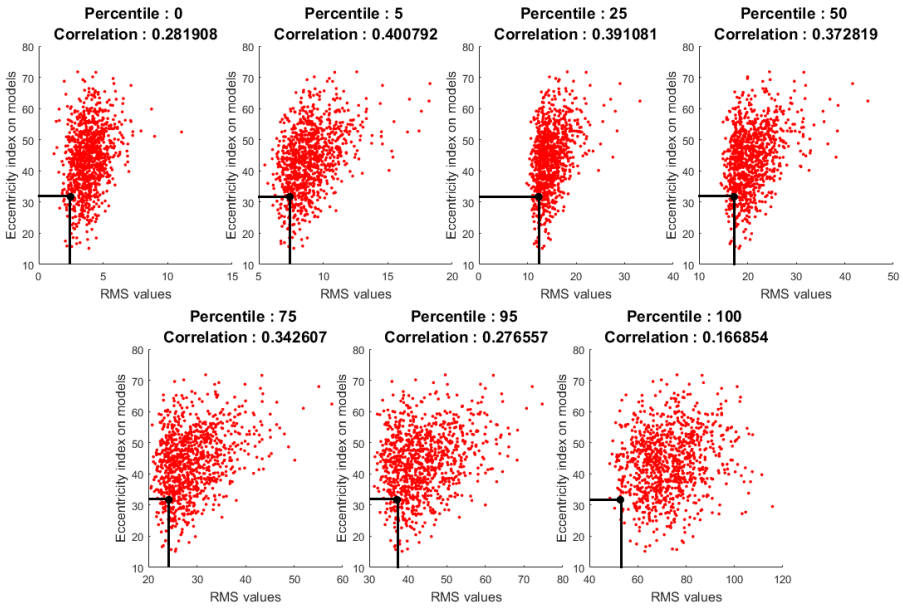

Figure 7.7: Effect of eccentricity in model space (h) on the goodness of the results (3-layer models).

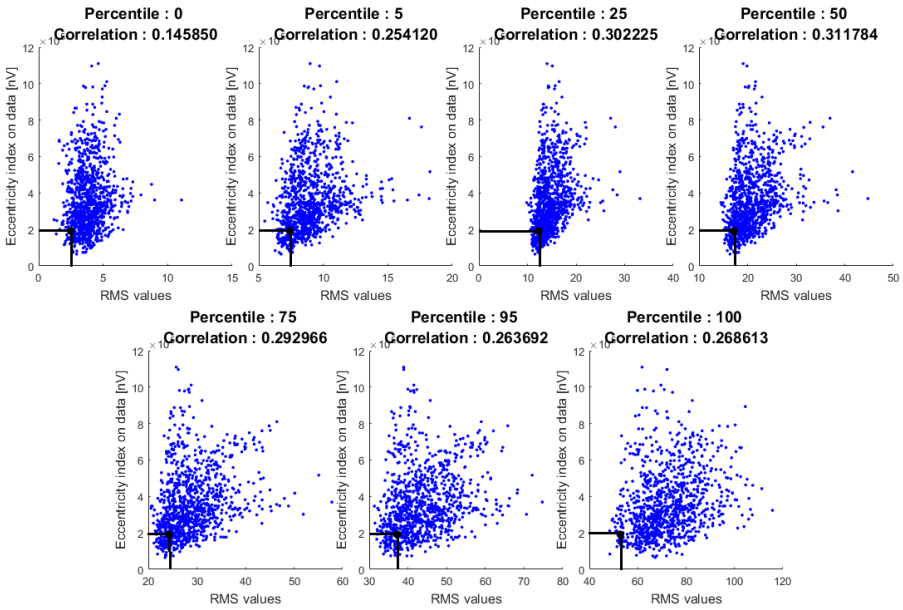

Figure 7.8: Effect of eccentricity in data space (d) on the goodness of the results (3-layer models).

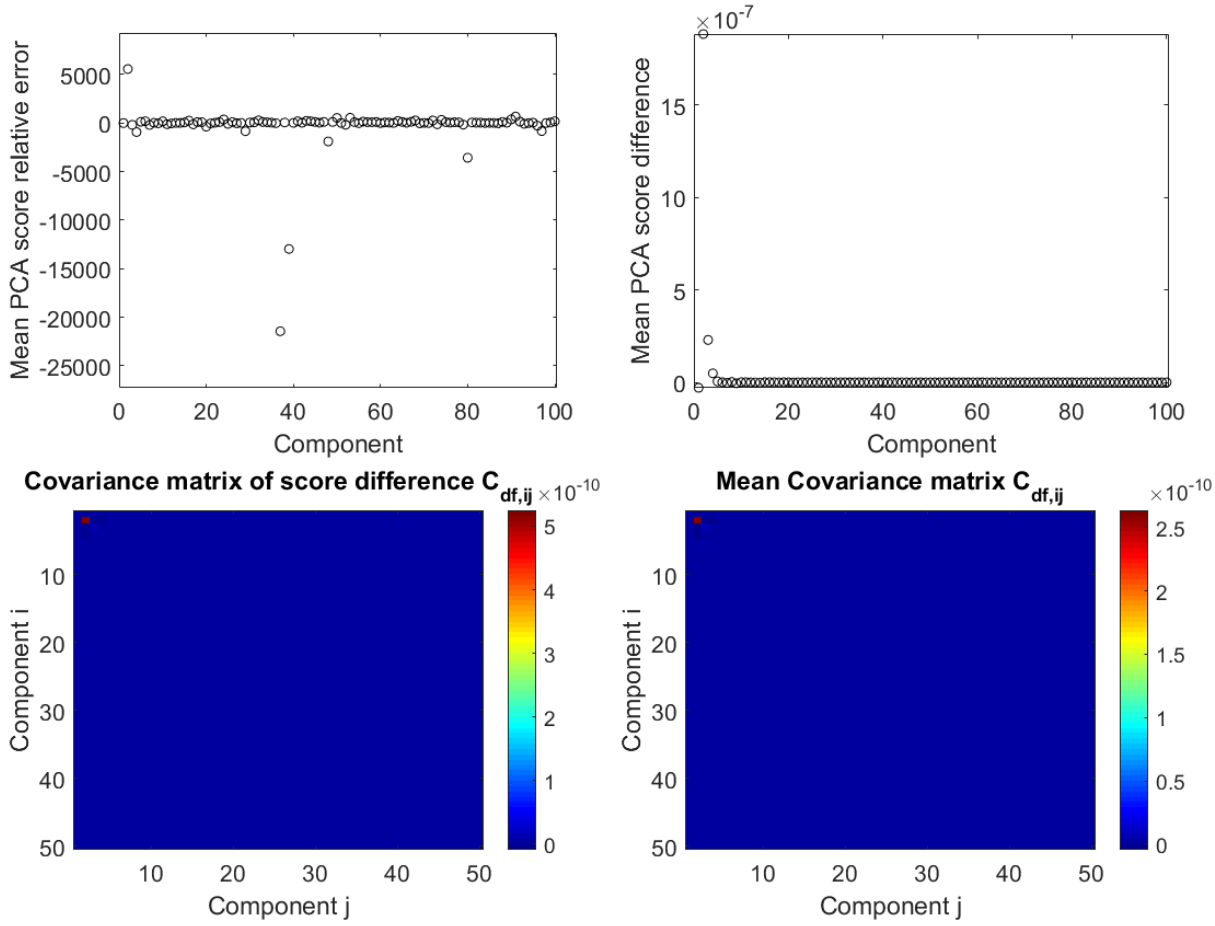

Figure 7.9: Propagation of noise in PCA scores: relative error on mean PCA score (upper left), difference in mean PCA score (upper right), covariance of score differences (lower left) and covariance of scores (lower right).

7.1.1.2 Noise contaminated datasets

Here, we will analyze the noise propagation in the PFA imaging. This is done by analyzing the variation of the PCA scores (i.e. the factors constituting the linear combination of the principle component analysis) when noise is added in the data (Hermans et al., 2016). To do so, 500 out of the 1000 models from the previous section (Subsection 7.1.1.1) have been exploited. A random Gaussian noise has been added to the data corresponding to each model. The tested noise level is 200 nV (standard deviation of the noise), which is already significant for NMR data acquired in good conditions (the amplitude of the signal is of the same order), but remains in a reasonable range.

From the graphs in Figure 7.9, even if the relative error on PCA score is significant, it turns out that the covariance of the scores is very small (less than 5×10^{-10}). This is insignificant and therefore, the noise has a negligible effect on the PCA scores. This finally

means that no particular attention should be drawn to the noise, as long as it is Gaussian (preprocessing of data is still recommended to remove spikes and harmonics).

In the light of this, an attempt to test noisy synthetic data was performed. The used model consists of a 2-layer model with its characteristics given in Table 7.1. The transmitter and receiver loops are the same and consist of a 50 m diameter loop. The noise level is set to 100 nV. The prior model space is defined as follows (uniform distributions):

- Thickness:
  - Layer 1: [10 20] m
- Water content:
  - Layer 1: [0.035 0.1]
  - Layer 2: [0.035 0.35]
- Relaxation time:
  - Layer 1: [5 350] ms
  - Layer 2: [5 350] ms

	Thickness [m]	Water content [%]	T_2^* [ms]
Layer 1	15	5	50
Layer 2	Inf	25	200

Table 7.1: Noisy model description.

The obtained posterior distribution is presented in Figure 7.10 and the corresponding models with their RMS are displayed in Figure 7.11.

From the results, it is observed that the water content is satisfactorily solved (the first layer, even better than the second), whereas the relaxation time distribution still remains wide. The true parameters are always present in the posterior distribution, proving the consistency of the applied scheme. The error on the estimated data originating from the models (RMS) is of the order of magnitude of the noise level, which again means that the model is well solved. On the obtained distributions of the parameters, the main effect of the PFA scheme is (1) to reduce the range of possible values and (2) to turn the prior uniform distributions into posterior Gaussian distributions. Therefore, the global uncertainty on the model parameters is actually reduced for all the parameters, even if the range of the posterior is as wide (or wider due to the use of kernel density) as the prior in some cases.

In order to demonstrate the ability of the PFA imaging process to handle Gaussian noise properly, it has been chosen to also present the results of the PFA imaging applied to

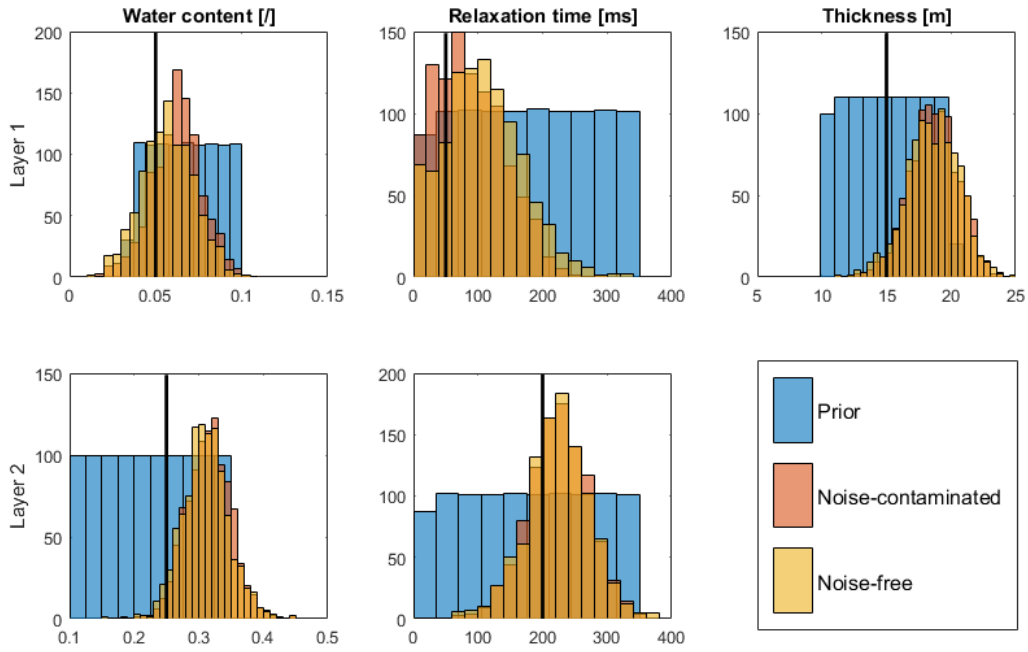

Figure 7.10: Posterior distribution for the 2-layer synthetic model. The solid black lines correspond to the true parameter values. Both the results from the clear and contaminated data are presented.

noise-free data from the same model. The obtained posterior distributions are displayed in Figure 7.10, where both results from the noise-free and the noise-contaminated datasets are presented. It appears that the two sets of distributions are very similar. This is consistent with the negligible impact of Gaussian noise on the process.

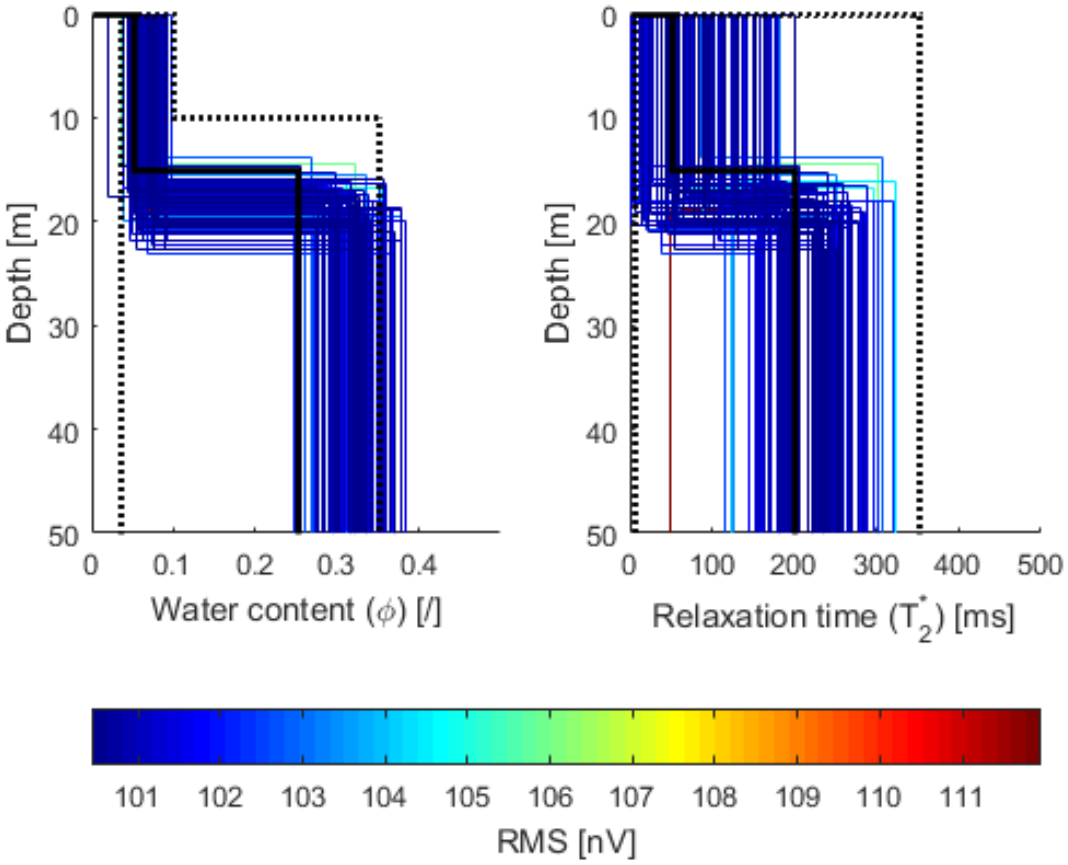

Figure 7.11: Models from the posterior distribution for the 2-layer noisy synthetic model. The true model is presented in solid black lines and the extent of the prior model space is defined with the dashed black lines.

7.1.2 Synthetic multiple loops

The example presented in this part is a 3-layer model (Table 7.2). The particularity of this synthetic data consists in the imposed acquisition context, which has been determined as a noisy environment (standard deviation of the Gaussian noise is 50 nV for the largest loop), with a proposed experimental configuration described in Table 7.3. The measured ambient magnetic field is the default one (48 000 nT) and the resistivity is constant across the model and equal to 100 Ω.m.

Layer	1	2	3
Depth [m]	5	30	Inf
Water content [%]	5	30	10
Relaxation time [ms]	100	200	50

Table 7.2: Synthetic multiple loops example: description of the model.

Loop	1	2	3
Diameter [m]	100	50	10
Transmitter	✓		
Receiver	✓	✓	✓
Noise level [nV]	50	12.5	1

Table 7.3: Synthetic multiple loops example: acquisition parameters.

This model will explore the advantages of the multiple-loop configuration discussed in Chapter 6. The first layer is very shallow and should therefore benefit from the increased sensitivity of the inner loops kernels in this zone.

Seven different configurations are possible, as presented in Table 7.4.

Name	Receiver		
	100 m	50 m	10 m
Independent 1	✓		
Independent 2		✓	
Independent 3			✓
Joint 1	✓	✓	
Joint 2	✓		✓
Joint 3		✓	✓
Joint 4	✓	✓	✓

Table 7.4: Possible configurations for the synthetic example.

The corresponding sensitivity kernels for this experimental configuration are presented in Figure 7.12. They show the classical characteristics of kernels. The Tx100/Rx100 kernel

has a unique depth sensitivity for each pulse moment, whereas the two others show a bimodal behavior for larger pulses with an increased sensitivity for shallow depth.

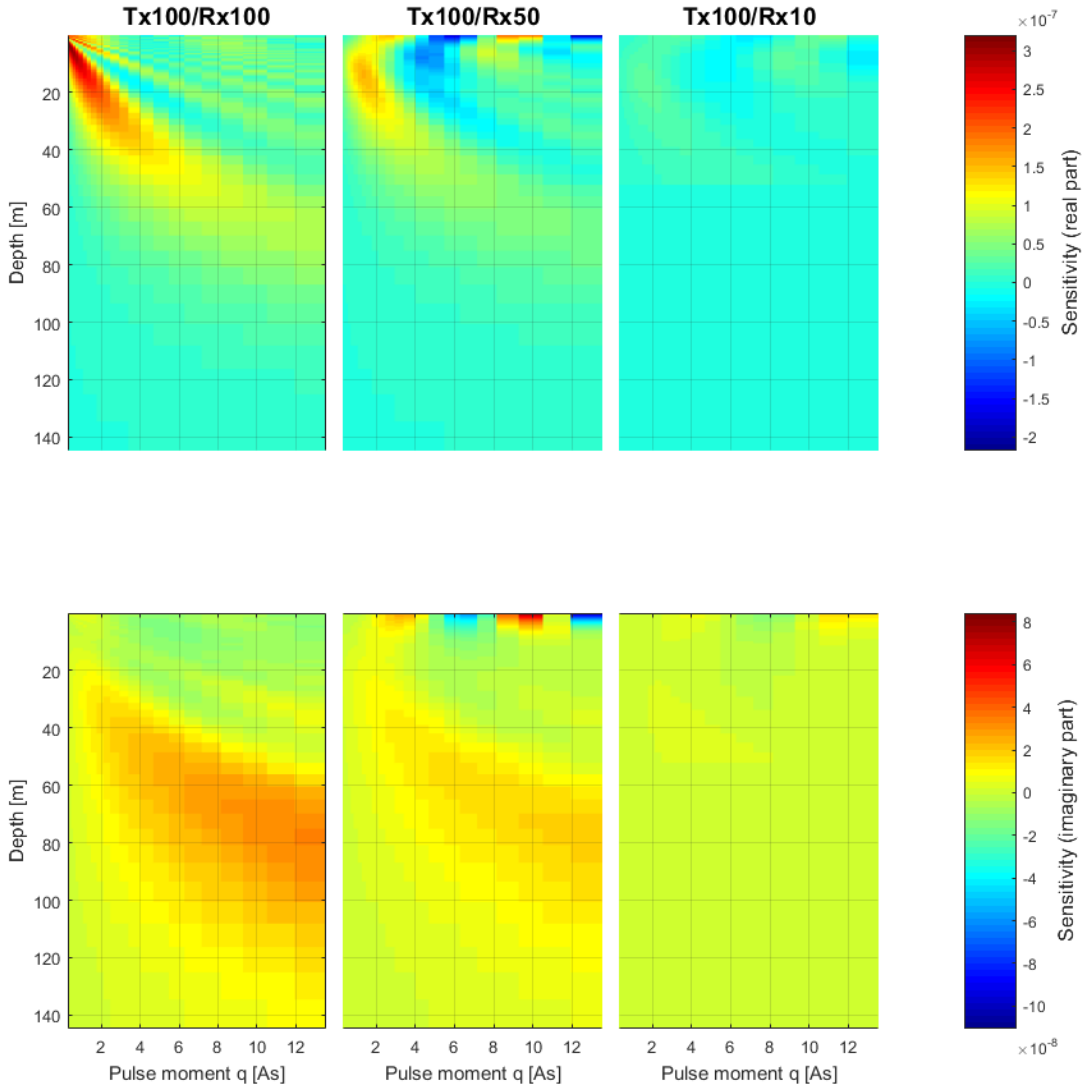

Figure 7.12: Sensitivity kernels for the multiple loops synthetic example. The sensitivity values are scaled to the diameter of the receiver loop for visualization.

7.1.2.1 QT inversion

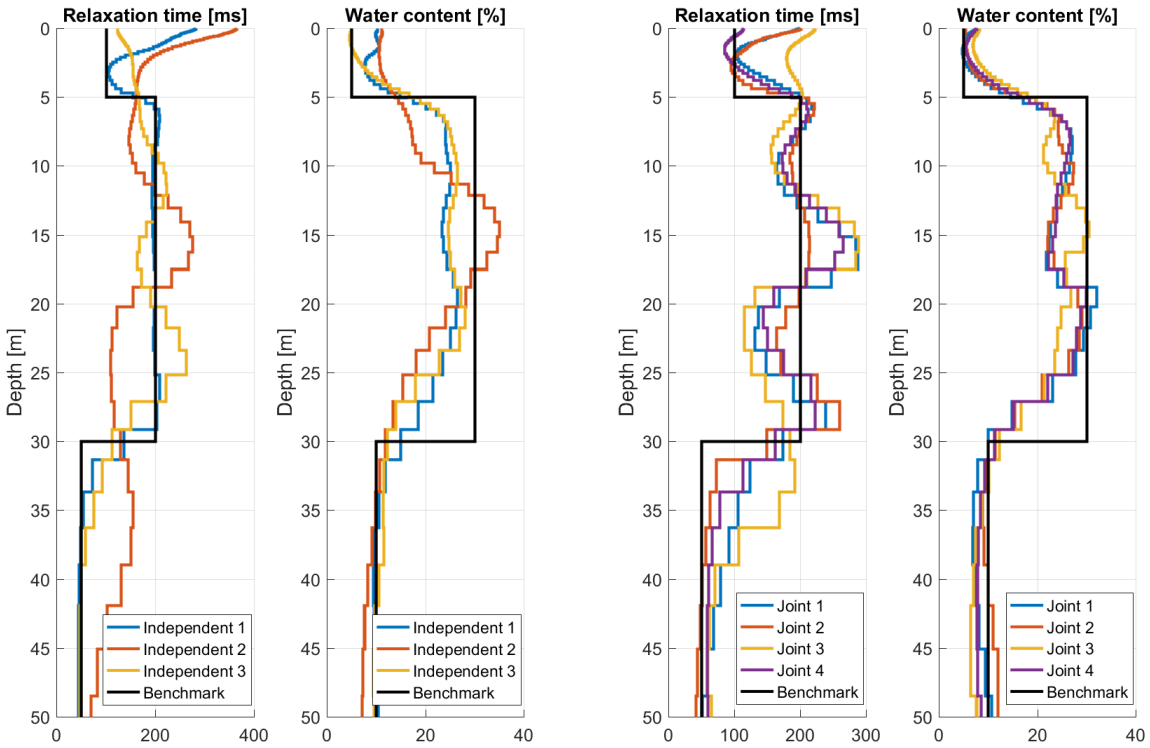

Figure 7.13: Results of the QT inversion applied to the synthetic data simulated from the model described in Table 7.2. The black lines correspond to the true model. On the left, the results of independent inversions (one transmitter/one receiver) are presented. On the right, the results of the joint inversions (one transmitter/multiple receivers) are presented (see Table 7.4 for configuration details).

The choice of the regularization parameter (Table 7.5) was made in order to provide a similar amplitude on the norm on the data error and the norm on the model, combined with the L-curve criteria (when consistent).

The results are presented in Figure 7.13. The "Independent" inversions perform poorly on the determination of the first transition (5 m depth) and present an inconsistent relaxation time distribution. The "Independent 1" (100 m transmitter/100 m receiver) and "Independent 2" (100 m transmitter/50 m receiver) are unable to provide accurate information on the shallowest part of the model. On the other hand, the "Independent 3" (100 m transmitter/10 m receiver) inversion provides information highlighting the low water content of the first meters of the subsurface. Globally, it seems that from all the independent inversions, the "Independent 3" (10 m receiver) leads to the most satisfactory

Configuration	Regularization parameter
Independent 1	5000
Independent 2	15 000
Independent 3	2000
Joint 1	8000
Joint 2	2500
Joint 3	10 000
Joint 4	15 000

Table 7.5: Regularization parameters for the multiple loops synthetic example.

results, yielding consistent water content and relaxation time distributions, even at shallow depth where other inversions provide too high water contents. This is logical, since this latter configuration benefits from a good sensitivity from 0 to 40 meters with a relatively high sensitivity at shallow depths. In terms of goodness of the fit on the simulated data, the χ^2 values are all slightly above 1, with the highest misfit attributed to the "Independent 2" and its 1.2 χ^2. This latter misfit is otherwise observed in the water content distribution where the obtained model shows a deeper unsaturated layer and a larger water content in the second layer.

The "Joint" inversions provide a more accurate distribution of the water content. The obtained results are very similar, at the exception of the "Joint 3" inversion (50 and 10 m receivers) that provides a too large relaxation time for the first layer, this latter inversion once again provides the highest misfit with a χ^2 value of 1.12, slightly above the others with values below 1.08. From all the inversions, it appears that the "Joint 4" is superior to all other results because it properly solves all the aspects of the model, without producing an artefact at surface (large relaxation time).

7.1.2.2 PFA imaging

The PFA imaging on the synthetic data presented above (Table 7.2) requires the definition of a prior model space. We will assume well-known that the subsurface can be separated into 3 layers. The thickness, water content and relaxation time of the three layers are uniformly distributed in the intervals presented below:

- Thickness:
  - Layer 1: [2.5 7.5] m
  - Layer 2: [20 30] m
- Water content:

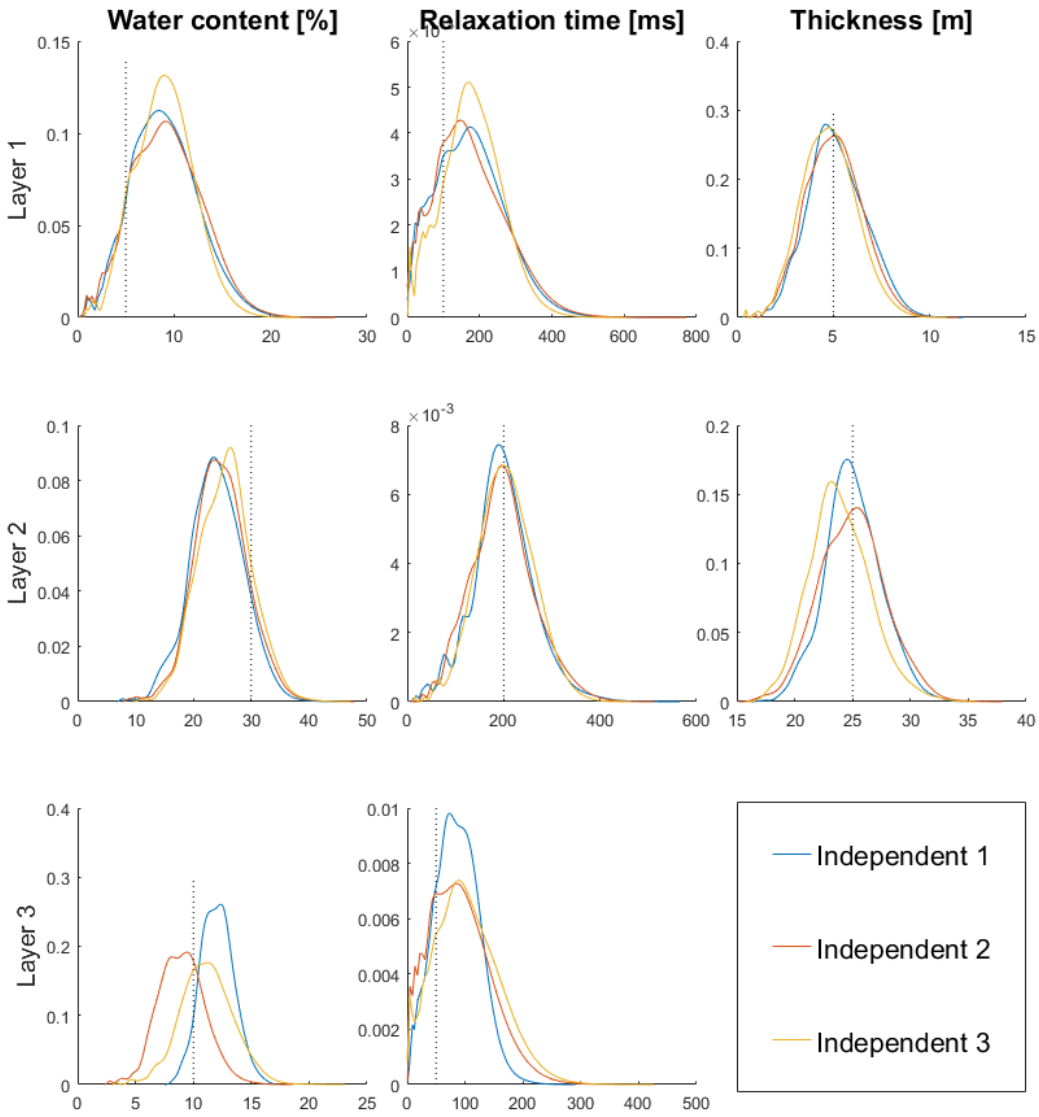

Figure 7.14: Posterior distributions after PFA imaging on the synthetic data, results from the "Independent" imaging.

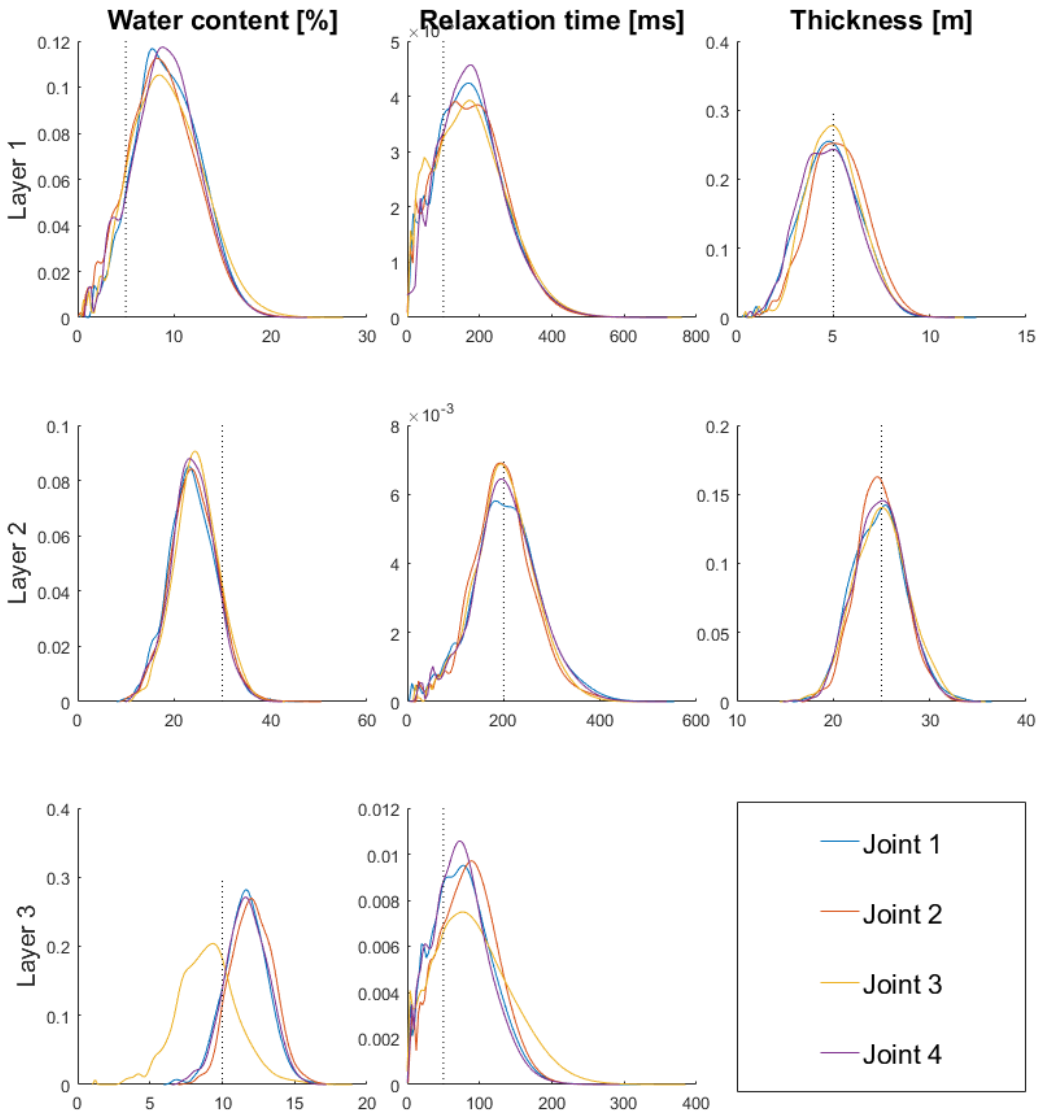

Figure 7.15: Posterior distributions after PFA imaging on the synthetic data, results from the "Joint" imaging.

  - Layer 1: [0.035 0.15]
  - Layer 2: [0.035 0.35]
  - Layer 3: [0.035 0.15]

- Relaxation time:
  - Layer 1: [5 350] ms
  - Layer 2: [5 350] ms
  - Layer 3: [5 350] ms

The results (Figures 7.14 and 7.15) show that the PFA imaging is able to provide consistent posterior distributions for all the parameters, but deliver very similar distributions with all configurations in the case of this low noise example. When analyzing the obtained distributions in terms of mean values and standard deviations, the values are barely changing with the different configurations, as opposed to the deterministic QT inversion results. This is demonstrated in Figure 7.16 where one can observe that the normalized standard deviation values are very close and that no configuration seems superior to the others.

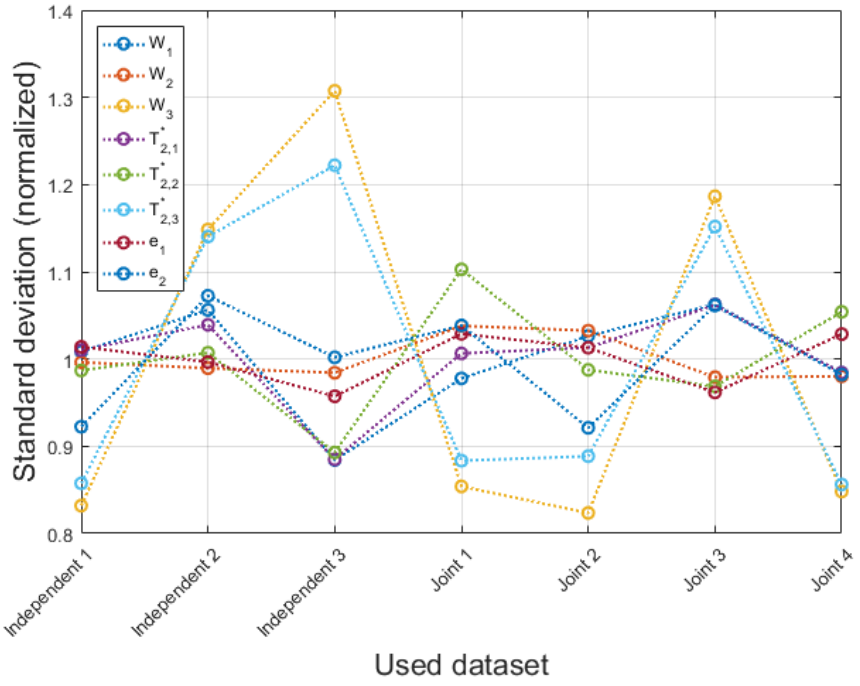

Figure 7.16: Evolution of the standard deviation of each posterior distribution, normalized to the mean value of the standard deviation of each result for each parameter.

The fact that all the distributions are already very similar brings the conclusion that each dataset has the same information level on the parameters, hence, no significant reduction should be obtained by merging the different datasets. As expected from this observation, the only parameter for which the distributions are not identical in the "Independent" configuration, $T^*_{2,3}$, is globally better resolved in the "Joint" imaging.

The results presented in this section showed once again that the innovative PFA imaging process is working properly, even on noisy data. On synthetic models and datasets, the PFA imaging always produced consistent posterior distributions of parameters, with a narrowing of the ranges and a transformation from uniform to Gaussian distributions.

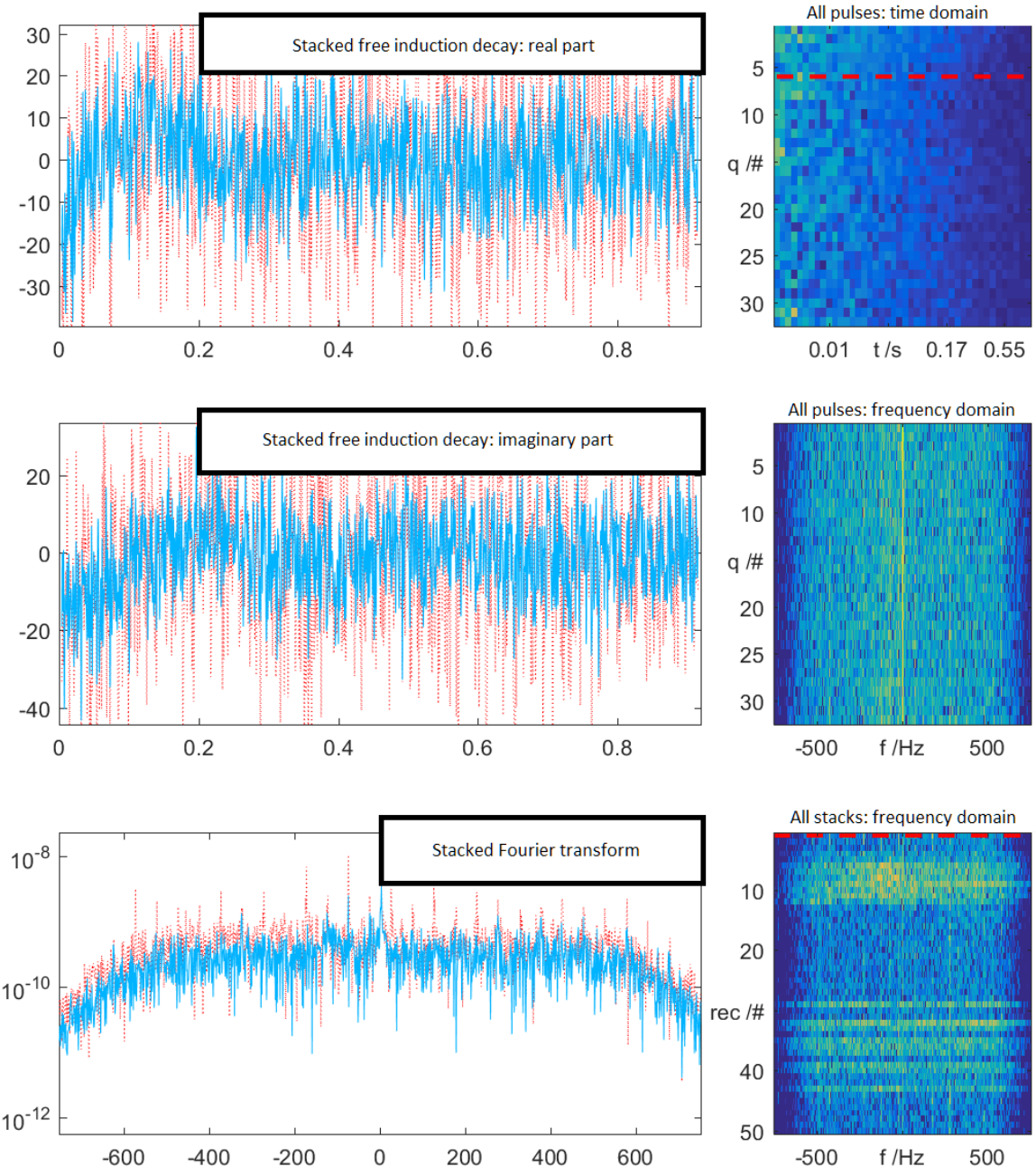

Figure 7.17: Data after noise processing at the Mont Rigi.

7.2 Real classical data: The case of Mont Rigi

The geological context of the Fagnes (Gilson, Briers, Ruthy, & Dassargues, 2017) offers a unique opportunity to test a two-layer model set-up. As peat exhibits high water contents (total porosity of 90% and 10 to 30% of effective porosity (Wastiaux, 2008)), we should get a significant response from this. On the other hand, in this specific geological context, the peat layer is lying on a Cambrian bedrock (La Venne formation) which is known as an aquiclude with very low water content (Gilson et al., 2017).

NMR is, therefore, a good candidate to retrieve the thickness of the peat layer and has been tested in February 2018. The data (Figure 7.17) showed a low noise level (about 13 nV for a 20 m diameter loop).

The kernel for this experiment (Figure 7.18) already shows us that the experimental design was probably not that efficient to retrieve information for shallow layers: the sensitivity to the first meters of soil is very small. Therefore, the results in terms of water content and relaxation time for the first layer might be inconsistent. However, the sensitivity to in-depth water is important, which means that the second layer should be reasonably resolved.

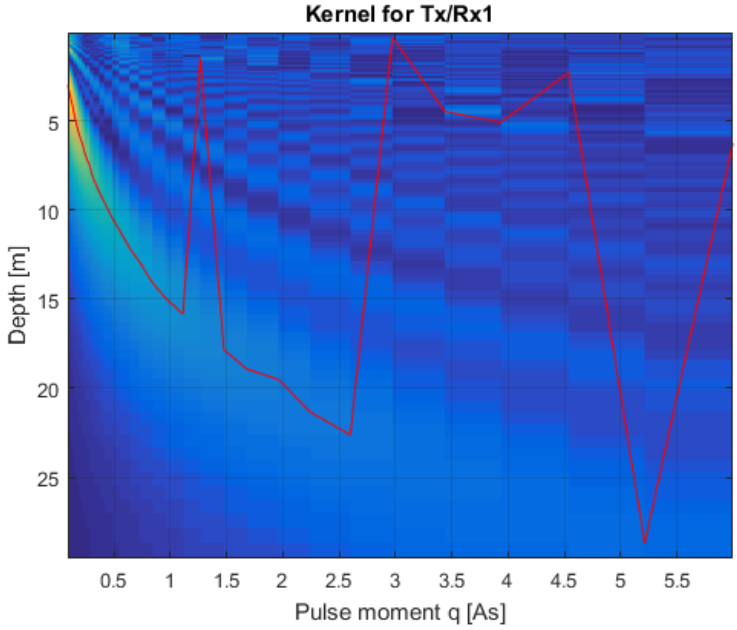

Figure 7.18: Kernel for the Mont Rigi experiment (Tx = Rx = 20 m diameter).

7.2.1 QT inversion of the Mont Rigi data

Standard processing of the data has been applied using despiking and noise removal from a reference loop available on the field (Müller-Petke et al., 2016). No further treatment was needed due to the exceptionally low noise level on site. Inversion using gate integration gave much better results than inversion on the raw data. This is due to the fact that the signal is very low and therefore, gate integration enables to retrieve more efficiently trends for the observed decay (noise has less impact on gated data than on raw data). Therefore, the use of gate integration has been chosen in further developments.

The kernel computation (Figure 7.18) was made under the assumption that the earth was resistive (infinite resistivity), which leads to a zero imaginary part of the kernels. This is not problematic in our case, as the shown signal is very low and the use of the imaginary part of the complex signal would significantly increase the noise in the dataset (the amplitude of the imaginary part is systematically lower, but the noise in the imaginary part and the real part of the signal are of similar amplitudes).

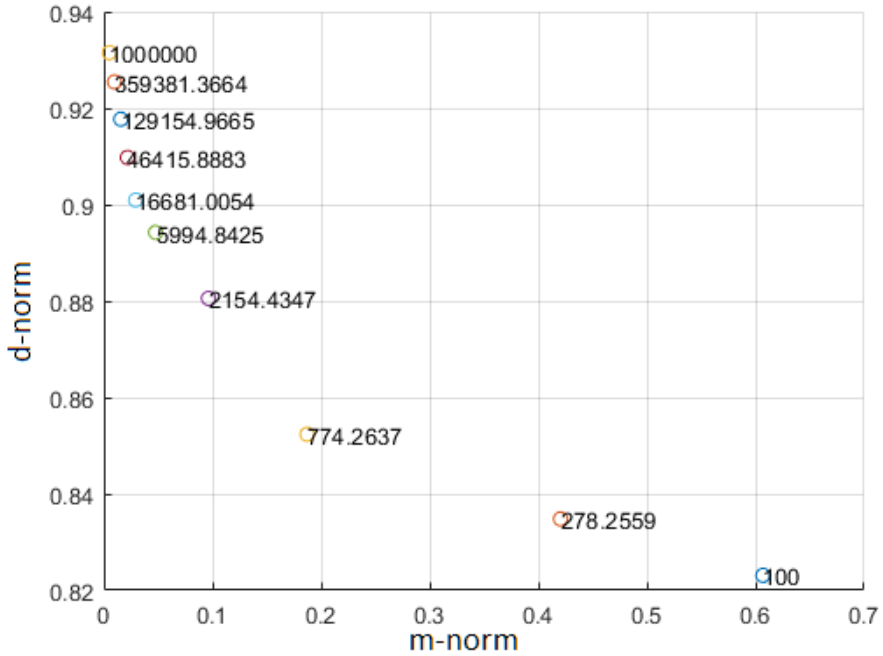

Figure 7.19: L-curve for the Mont Rigi dataset.

The optimum regularization parameter was obtained according to the L-curve criteria (the maximum of curvature in the curve corresponds to the best regularization parameter) and is around 775 (Figure 7.19).

The results of the deterministic inversion are shown in Figure 7.20 (black curve). The deterministic result clearly shows a two-layer structure with the first layer depth around

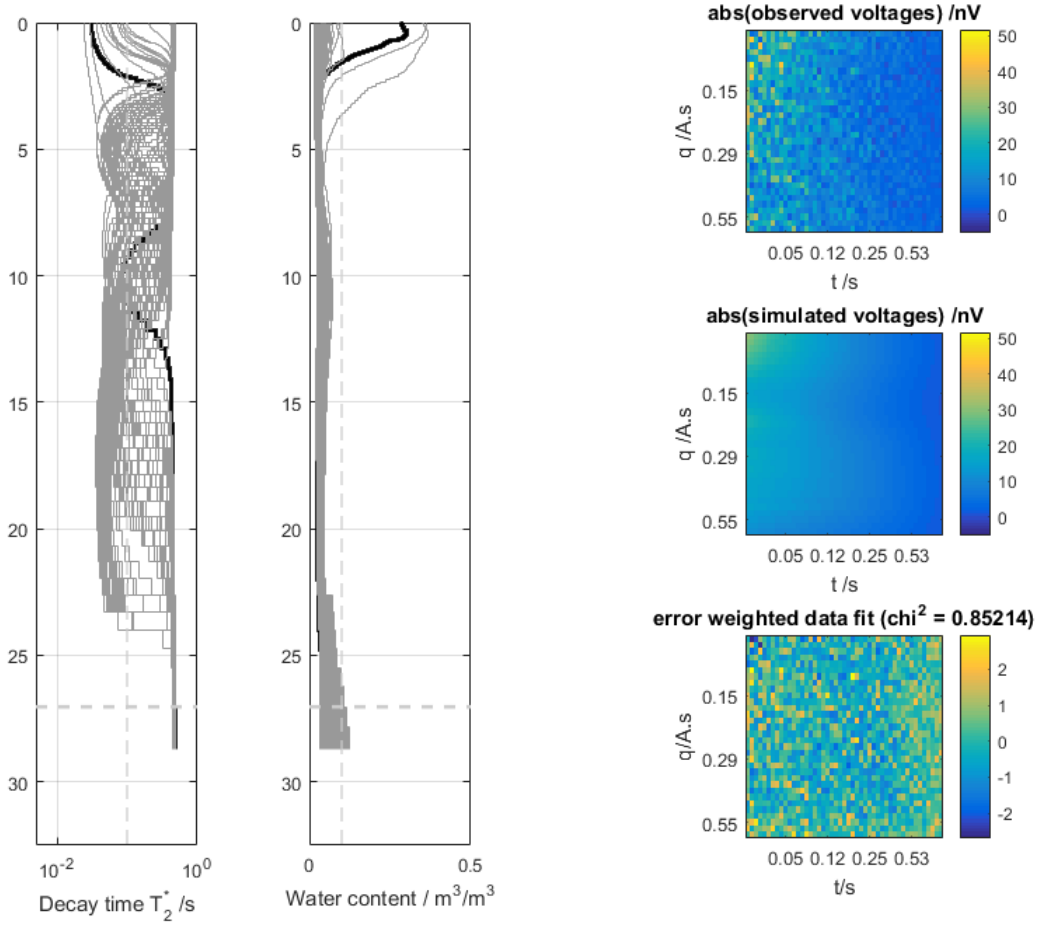

Figure 7.20: Left: QT Inversion results for the Mont Rigi data. The black curve represents the deterministic inversion results and the grey curves show the results of bootstrap inversion (first approximation of the uncertainty). Right: Forward model and error associated to the deterministic inversion result.

2 meters. Moreover, decay time tends to present another structure in depth (10 m) that could be linked to fractures filling or other unknown geological features.

The bootstrap inversion (testing numerous subsamples of the dataset) shows that the presence of the layer is highly uncertain (even if, from previous geological studies, we know that a peat layer is present with a high water content).

As a conclusion, it appears that the dataset is probably not containing enough information about the first meters to precisely demonstrate the presence of the peat layer using NMR. Nonetheless, the purely deterministic inversion seems to demonstrate the presence of a first layer with a thickness around 2 meters, even if its characteristics are uncertain.

This is coherent with the presence of a peak at Larmor frequency in the Fourier transform of the FID signal (Figure 7.17), that implies the presence of water.

7.2.2 PFA imaging of the Mont Rigi data

PFA imaging based on the dataset acquired in the Mont Rigi has been performed with the prior defined in Table 7.6.

	Thickness [m]	Water content [%]	T_2^* [ms]
Layer 1	$[0, 5]$	$[0.035, 0.35]$	$[5, 500]$
Layer 2	Inf	$[0.035, 0.1]$	$[5, 500]$

Table 7.6: Prior model space for Mont Rigi.

The results from this experiment are presented for the PFA in Figure 7.21. From a prior uncertainty on the thickness of the peat layer from 0 to 5 meters, the PFA scheme obtained a slightly smaller range with a Gaussian distribution instead of the uniform distribution of the prior. The water content of the second layer is also well solved: between 0.03 and 0.10, which is plausible regarding the context of the site.

The predicted values for the relaxation time, as well as the water content of the first layer are way more spread. This is caused by two different effects. The first layer is badly resolved due to the lack of sensitivity of the experiment to the first 2 meters (cfr. kernel, Figure 7.18). For the relaxation time, the large range of observed values may be caused by the very low water content, leading to an intrinsic insensitivity to this parameter (Appendix B). It is also observed that the posterior distribution for those parameters is wider than the prior distribution. This is due to the use of the kernel density function that naturally widens the distributions in CCA space.

Finally, the RMS values are slightly higher than the noise level (10 nV) with values between 10 and 20 nV.

The results obtained in this section proved that the discussed schemes to exploit SNMR data (QT inversion and PFA imaging) are reliable. They produced relevant results, even if the amplitude of the registered signal was very low. A major divergence between the two approaches is already observed: the QT inversion provides a deterministic result (which can be somewhat extended to a first approximation of uncertainty using the bootstrap inversion), whereas the PFA imaging provides a full posterior distribution of parameters, hence, a full image of the uncertainty. The results of the QT inversion are included in the distributions obtained through the PFA imaging.

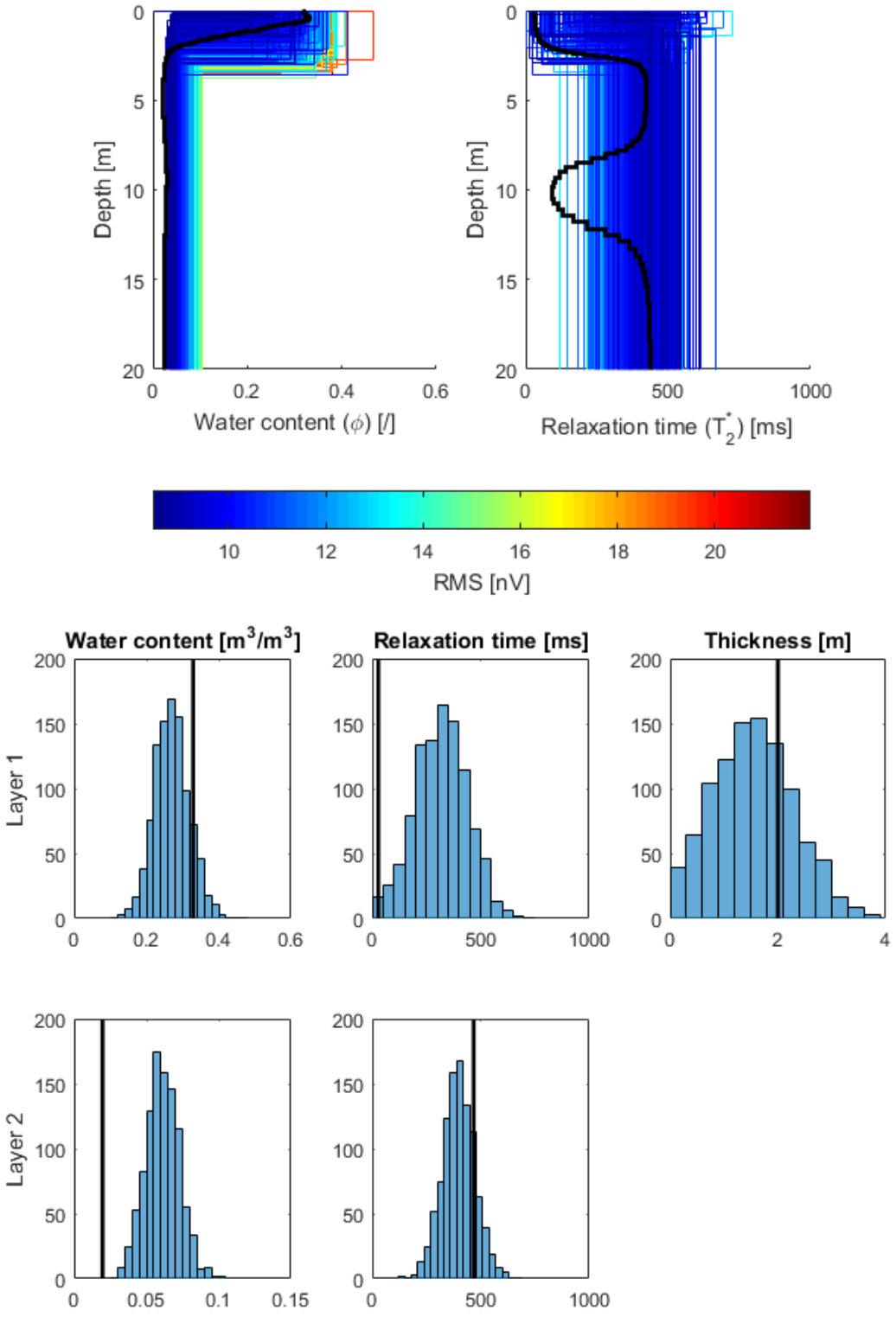

Figure 7.21: Results for the Mont Rigi experiment.
Top: Model distributions, Bottom: Parameters distributions. The black lines represent the QT inversion results.

7.3 Real multi-loops data: The Schillerslage site (Germany)

The Schillerslage hydrogeophysical test site is located in Germany, near Hanover. It has been studied since 2009 by the Liebniz Institute for Applied Geophysics (LIAG) (Dlugosch, 2014). The site is equipped with multiple boreholes and is widely studied using several geophysical techniques, among which electromagnetic, induced polarization, ground penetration radar and seismic measurements (Holland et al., 2011). Surface Nuclear Magnetic Resonance has been used on this site previously (Dlugosch, 2014) combined with ERT measurements (Figure 7.22).

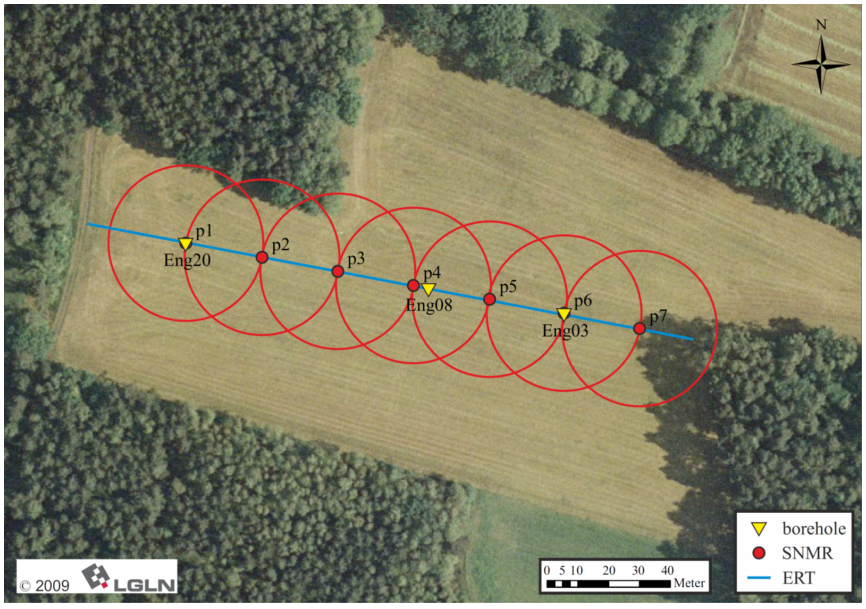

Figure 7.22: Configuration of the NMR experiments lead by Dlugosch (2014).

The geology of the site consists of a succession of sub-horizontal layers from the glacial periods Elsterian, Saalian and Weichselian above a marl bedrock from the Late Cretaceous (Binot, 2008). Three lithological profiles are available at the boreholes Eng20, Eng08 and Eng03. They show few vertical variations (less than 1 meter changes for interfaces) and could therefore be summarized in one lithological profile. The lithological profile (Figure 7.23) can be described as follows (from top to bottom):

- Medium sand from the Weichselian for 5 meters (+/- 1 meter)
- Fine to medium sand from the Saalian for 5 meters (+/- 2 meters)
- Silt, sand and gravels from the Elsterian for 5 meters (+/- 1 meter)

- Till and boulder clay from the Elsterian for 3 meters (+/- 1 meter)
- Medium to coarse sand from the Elsterian for 5 meters (+/- 1 meter)
- Marl bedrock from the Late Cretaceous of unknown thickness

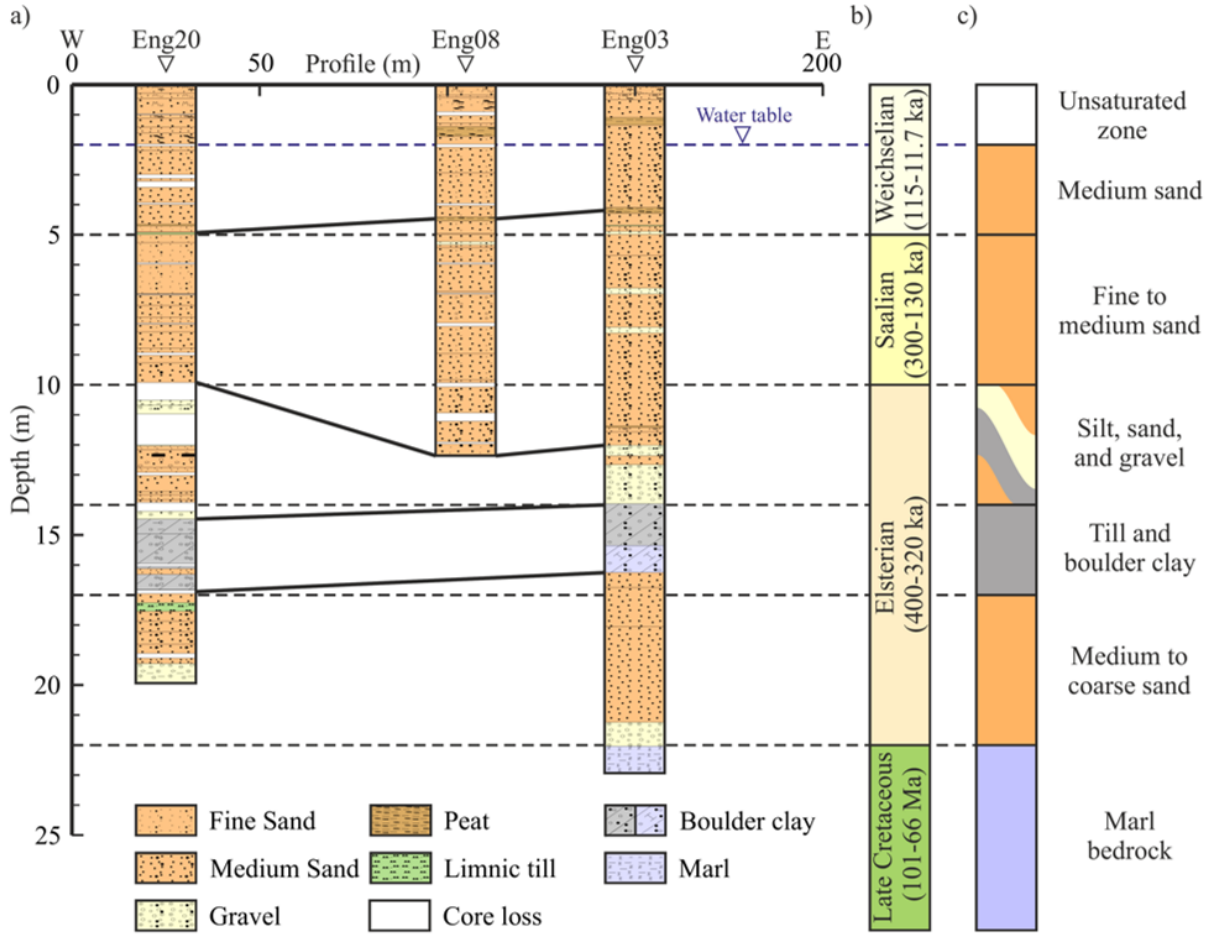

Figure 7.23: Summary of the lithological profiles from the boreholes on the Schillerslage test site (see Figure 7.22 for the localization of the boreholes) (from Dlugosch, 2014).

Hydrogeologically, the soil is characterized by a shallow unsaturated zone (2 meters +/- 0.5 meter inter-seasonal variations) and is then saturated until the bedrock (which is also saturated). The aquifer is split into two different zones by the clay layer from the Elsterian (on the site, this acquiclude is present around 15 meters depth) but on a large area, the confining layer is sometimes not present and its thickness can vary widely.

The dataset analyzed in this work has been acquired approximately at the location of the Eng20 borehole, where previous water content measurements were available (Dlugosch,

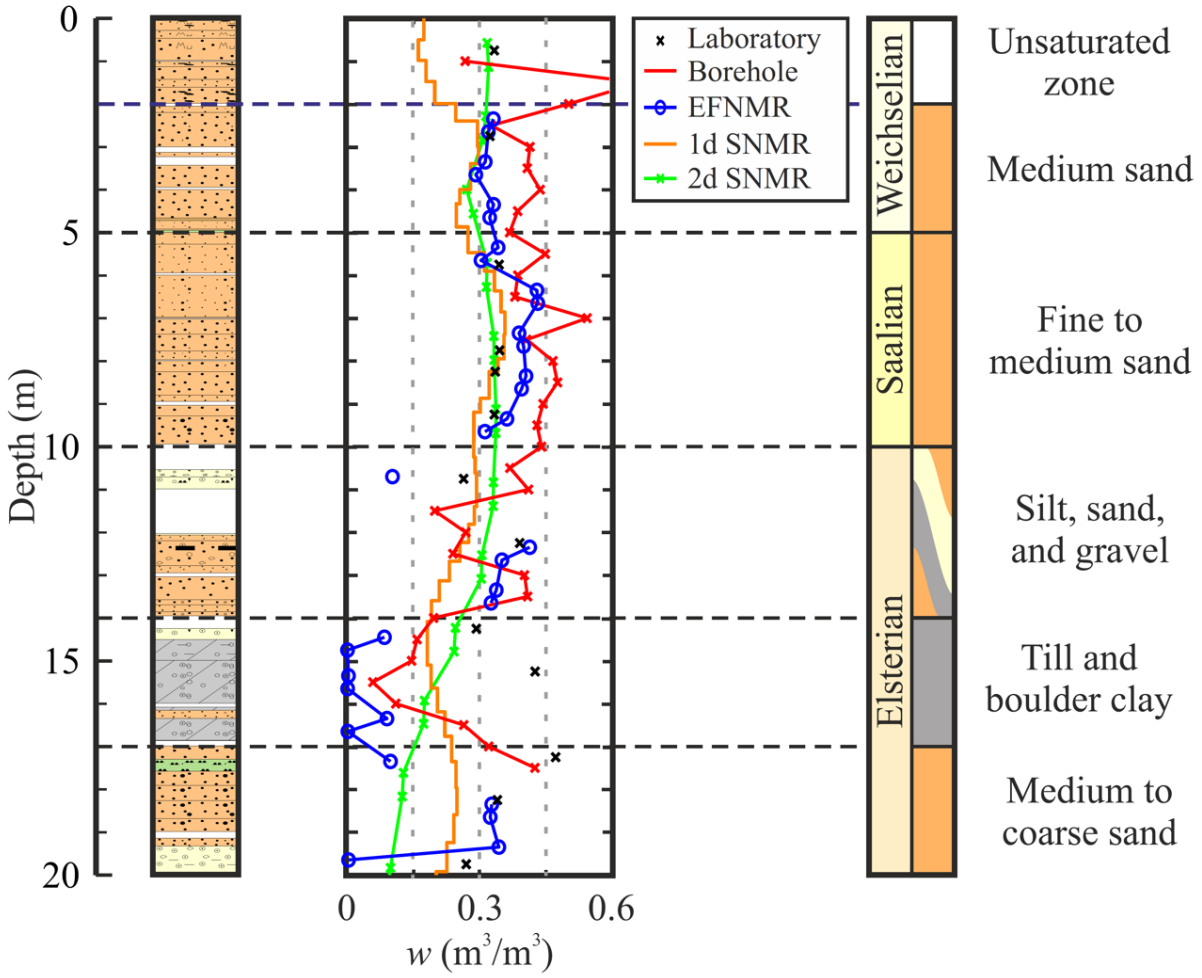

Figure 7.24: Different water contents obtained with different NMR methods (from Dlugosch, 2014).

2014). Those water contents are presented in Figure 7.24. The experimental configuration consisted of three loops disposed concentrically and one reference loop for the noise acquisition (Figure 7.25).

Three sequences of acquisition have been tested:

1. Injection on the 50 m loop and reception of the signal on the 50, 30 and 10 m loops with pulse length of 20 ms.

2. Injection on the 50 m loop and reception of the signal on the 50, 30 and 10 m loops with pulse length of 10 ms.

3. Injection on the 30 m loop (two turns instead of one previously) and reception of the signal on the 50, 30 and 10 m loops with pulse length of 20 ms.

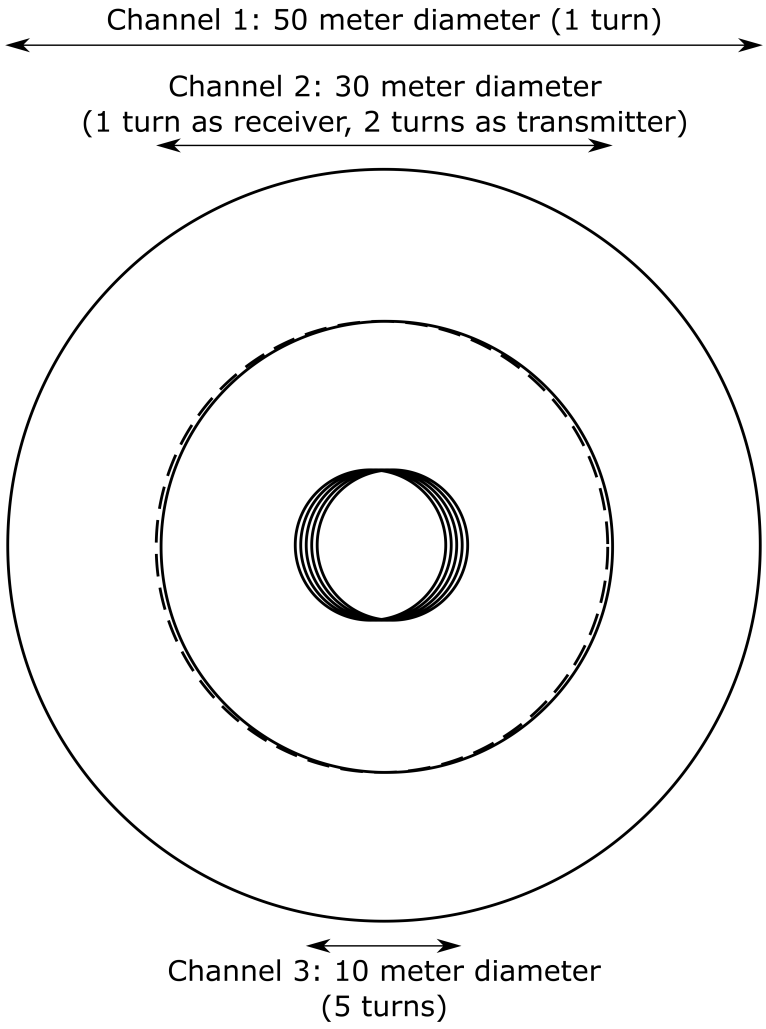

Figure 7.25: Multiple loops experimental configuration used on the Schillerslage test site.

The different configurations were not all explored in this work. Actually, the dataset originating from the 10 ms acquisition (2) showed less precise peaks around the Larmor frequency, meaning they were less trustful. Therefore, this latter has been discarded in further developments and the acquisitions with pulse length of 20 ms (1 and 3) were the only ones kept for analysis.

One can enumerate the different options for the configurations of the datasets. This is performed in Table 7.7. In total, there are 21 possible transmitter/receiver combinations to interpret. Normally, all those combinations should lead to similar models, even if the sensitivity changes with the configuration. Different types of configurations are proposed:

Name	Transmitter		Receiver		
	50 m	30 m	50 m	30 m	10 m
Independent 1	✓		✓		
Independent 2	✓			✓	
Independent 3	✓				✓
Independent 4		✓	✓		
Independent 5		✓		✓	
Independent 6		✓			✓
Joint 1	✓		✓	✓	
Joint 2	✓		✓		✓
Joint 3	✓			✓	✓
Joint 4	✓		✓	✓	✓
Joint 5		✓	✓	✓	
Joint 6		✓	✓		✓
Joint 7		✓		✓	✓
Joint 8		✓	✓	✓	✓
General 1	✓	✓	✓		
General 2	✓	✓		✓	
General 3	✓	✓			✓
General 4	✓	✓	✓	✓	
General 5	✓	✓	✓		✓
General 6	✓	✓		✓	✓
General 7	✓	✓	✓	✓	✓

Table 7.7: Possible configurations on the Schillerslage dataset.

- Independent: one transmitter combined with one receiver (6 possibilities)
- Joint: one transmitter but multiple receivers (8 possibilities)
- General: multiple transmitters and one or multiple receivers (7 possibilities)

Each proposed configuration will be interpreted using the classical QT inversion algorithm as well as the newly proposed PFA imaging process. The addition of new data will be discussed and the usefulness of each inversion will be demonstrated. The main object of this research is to prove the superiority of the "General" configuration in terms of sensitivity and results, compared to the classically used independent inversion.

7.3.1 Sensitivity kernels at Schillerslage

In order to compute the kernels, the experimental design must be taken into account as well as the characteristics of the site. On-site measurements have shown that the ambient

Earth's magnetic field (B_0) has an intensity of 49 380 nT. The inclination is of 68°(Dlugosch, 2014).

Dlugosch (2014) measured the electrical resistivity on-site using ERT. The results showed that no particular structures were present except for the ones identified in the 1-D lithological profiles (Dlugosch, 2014). Therefore, the resistivity model obtained in this experiment (Figure 7.26) can be transformed into a 1-D model of the subsurface resistivity.

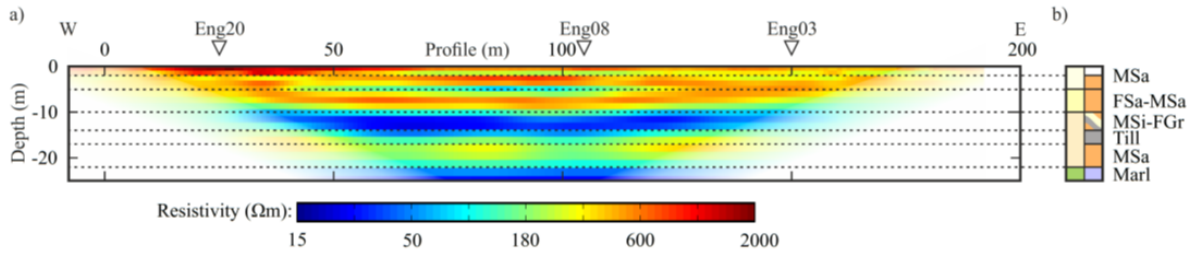

Figure 7.26: 2-D resistivity profile at the Schillerslage experimental site (Dlugosch, 2014).

The 1-D resistivity profile can be described as follows (from top to bottom, Dlugosch (2014)):

- 500 $\Omega.m$ from 0 to 4.5 meters (Weichselian sand)
- 300 $\Omega.m$ from 4.5 to 10 meters (Saalian sand)
- 85 $\Omega.m$ from 10 to 16 meters (Elsterian silt, sand, gravels and clay)
- 200 $\Omega.m$ from 16 to 22 meters (Elsterian sand)
- 20 $\Omega.m$ from 22 meters to an undefined boundary (Late Cretaceous marl bedrock)

As it has been shown that the kernels are sensitive to resistivity values below 100 $\Omega.m$ (Behroozmand et al., 2015), our case will require the use of a consistent (even if not exact) resistivity model to compute the sensitivity kernels. In the absence of a resistivity model, the results of the experiment could slightly differ. For example, if the choice was to use a resistive earth model, the imaginary part of the kernels would have been non-existent. On the other hand, the use of a constant 100 $\Omega.m$ resistivity could still provide efficient results, but the accuracy could change, since the value of the kernels would differ, especially in the imaginary part (the most sensitive to resistivity).

From those kernels, it is easy to compute the cumulative sensitivity of a given configuration method with depth. This already provides a first insight of the advantages and the superiority of a method above another. The sensitivity here is simply defined as the sum along all pulse moments of sensitivity kernels for each depth. This is presented in Figure 7.29.

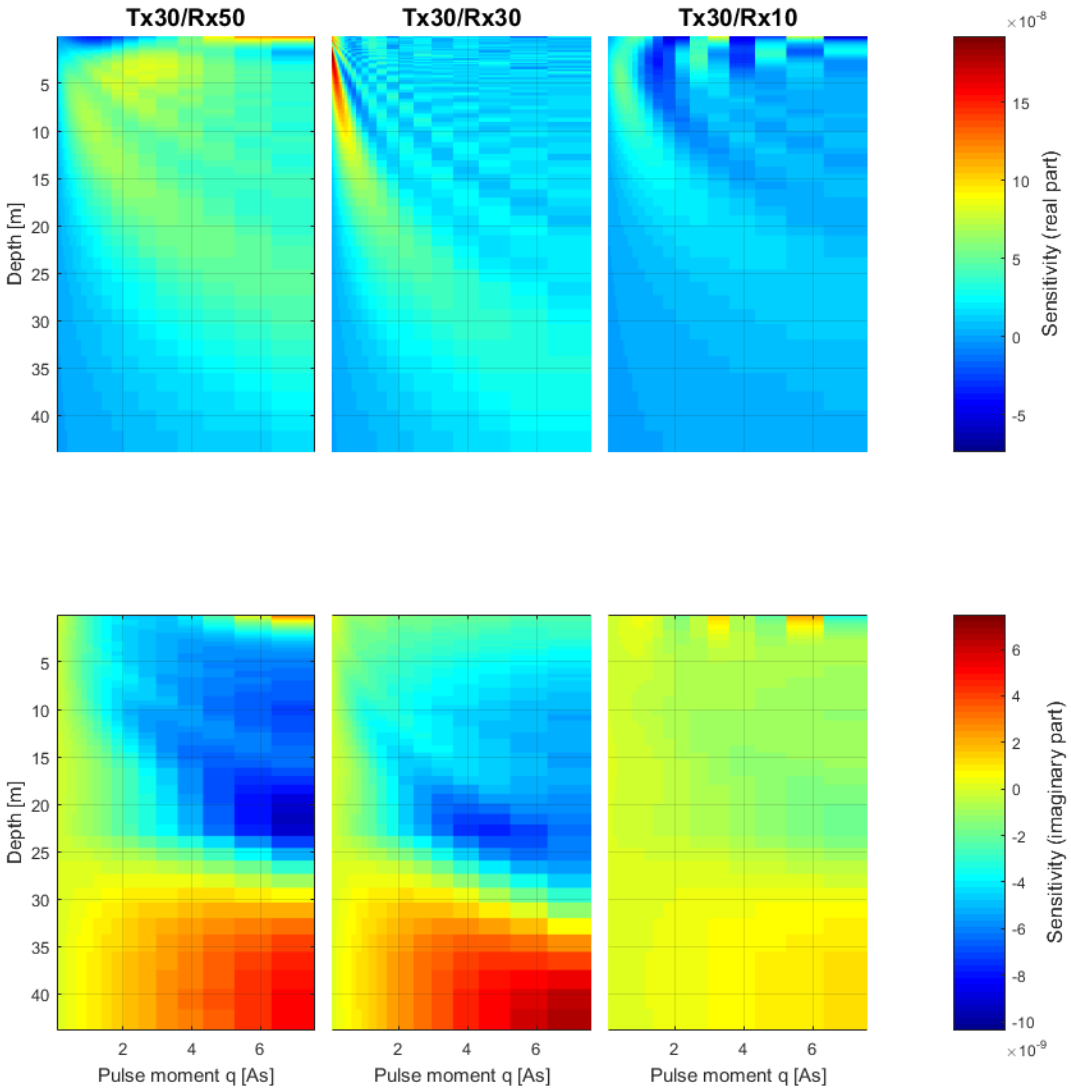

Figure 7.27: Sensitivity kernels (in V/m) for the different receiver loops with the 30 m transmitter loop.

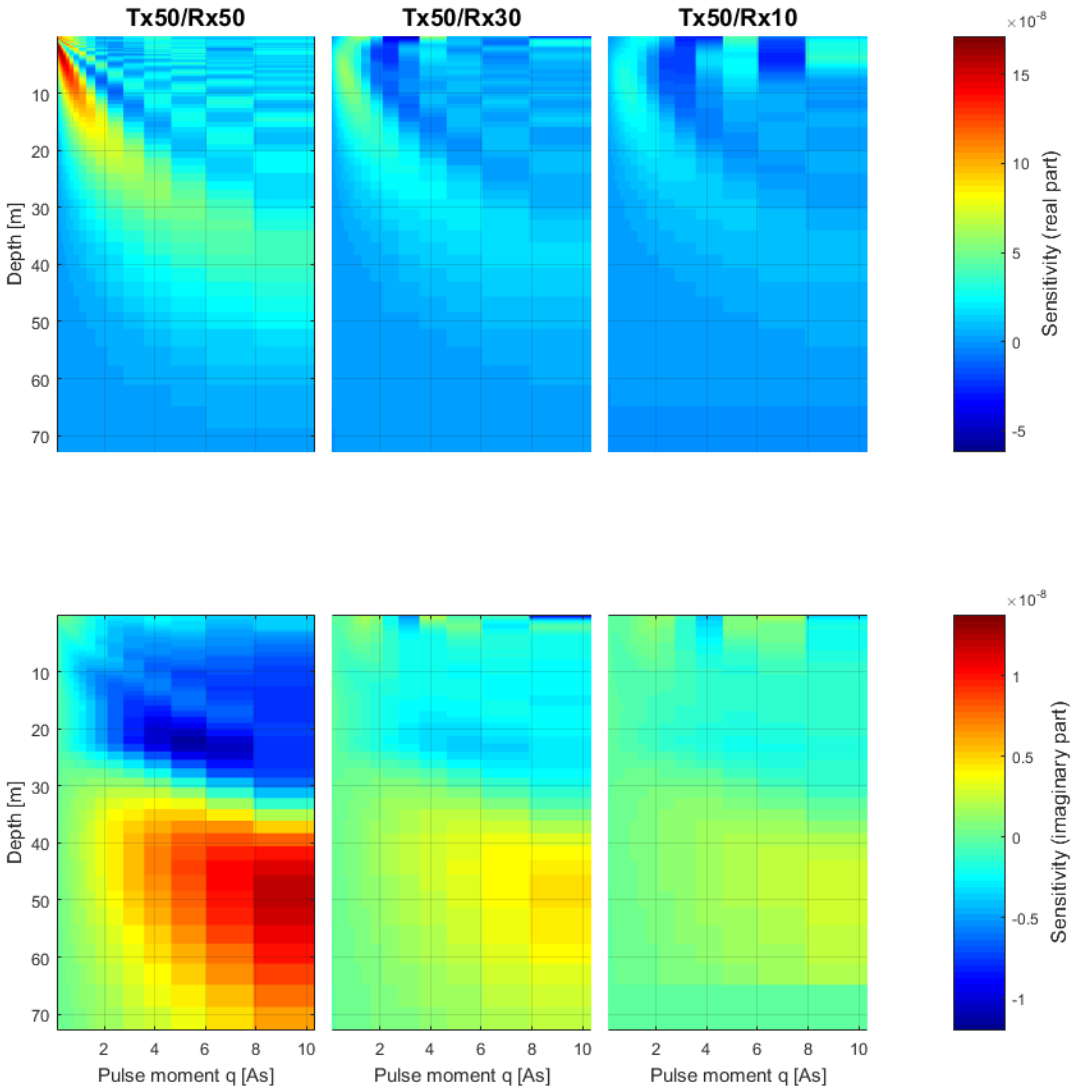

Figure 7.28: Sensitivity kernels (in V/m) for the different receiver loops with the 50 m transmitter loop.

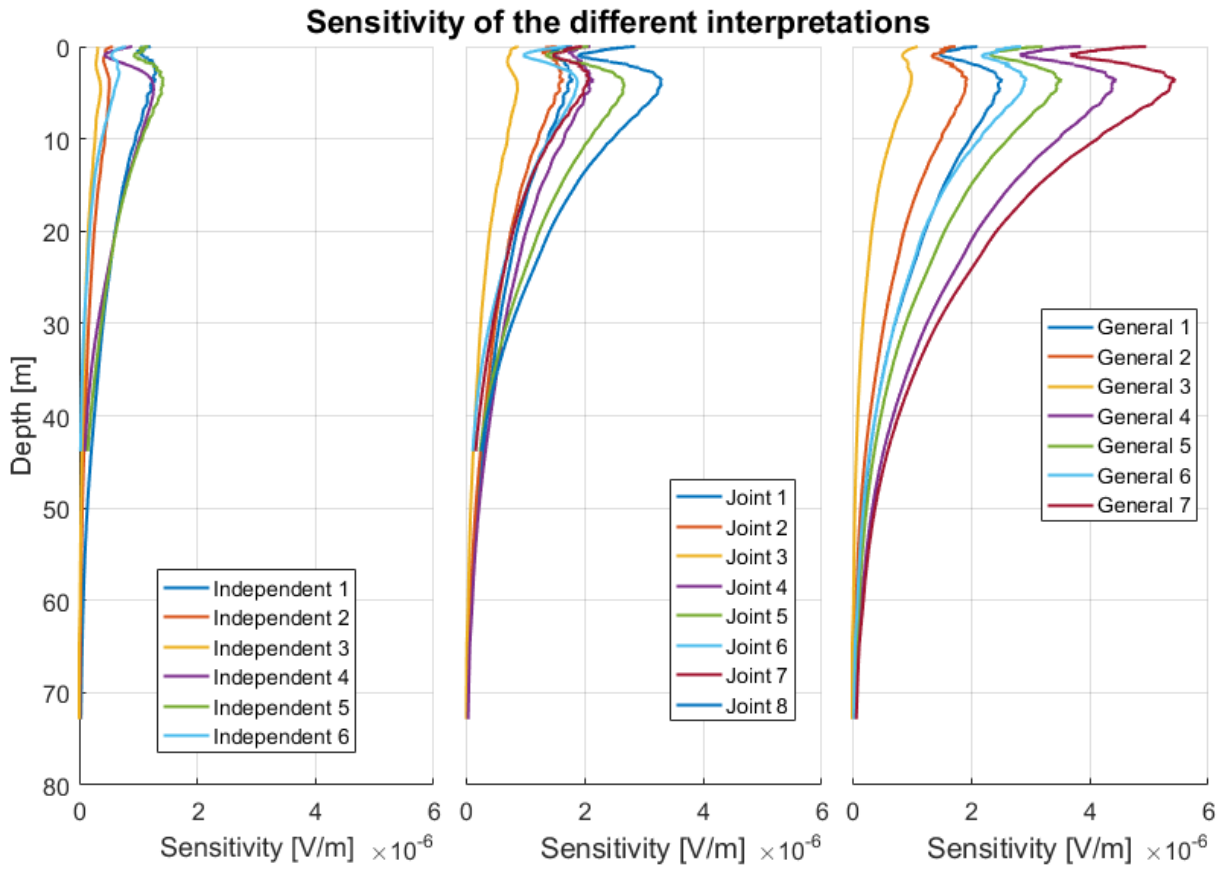

Figure 7.29: Sensitivity of the different configurations proposed according to the sensitivity kernels (absolute value), the names of the configuration refers to names presented in Table 7.7.

From Figure 7.29, it is easily understood that the so-called general inversion is supposed superior to every other type of inversion explored. It gives a much larger sensitivity to the whole depth. The joint inversions with the 30 m loop as unique transmitter tends to show that this configuration gives more load to the shallow layers. This makes sense since the perturbed volume of soil is shallower.

The sensitivity is globally one order of magnitude higher in the real part than in the imaginary part of the kernels. Nonetheless, it is observed that the in-depth sensitivity is larger for the imaginary part than for the real part of the signal. This is due to the highly conductive marl bedrock ($20\Omega.m$).

A further analysis of the sensitivity kernels reveals that the sensitivity as a function of the pulse moments is not straightforward in the cases where the receiver (Rx) is not of the same size as the transmitter (Tx). According to Figures 7.27 and 7.28, the sensitivity tends towards a bimodal distribution as a function of depth, with a first peak in the shallowest

zones and a second peak in the lower part, closer to the path of the sensitivity attributed to the case where the transmitter and the receiver are of the same size. This is also observed in the sensitivity plots (Figure 7.29) where a first peak is observed at 0 meter and then, a second one (of slightly larger amplitude) takes place around 5 meters. Therefore, we can assume that the experimental design gives us access to more detailed information about those two zones.

Proportionally, it is observed that the 30 meter diameter transmitter (Independent 4 to 6 and Joint 5 to 8) results in higher sensitivities than the 50 meter one (Independent 1 to 3 and Joint 1 to 4).

7.3.2 QT inversion

7.3.2.1 Independent inversion: 1 transmitter/1 receiver

The results of the independent inversions are displayed in Figure 7.30. Some characteristics of those results are presented in Table 7.8.

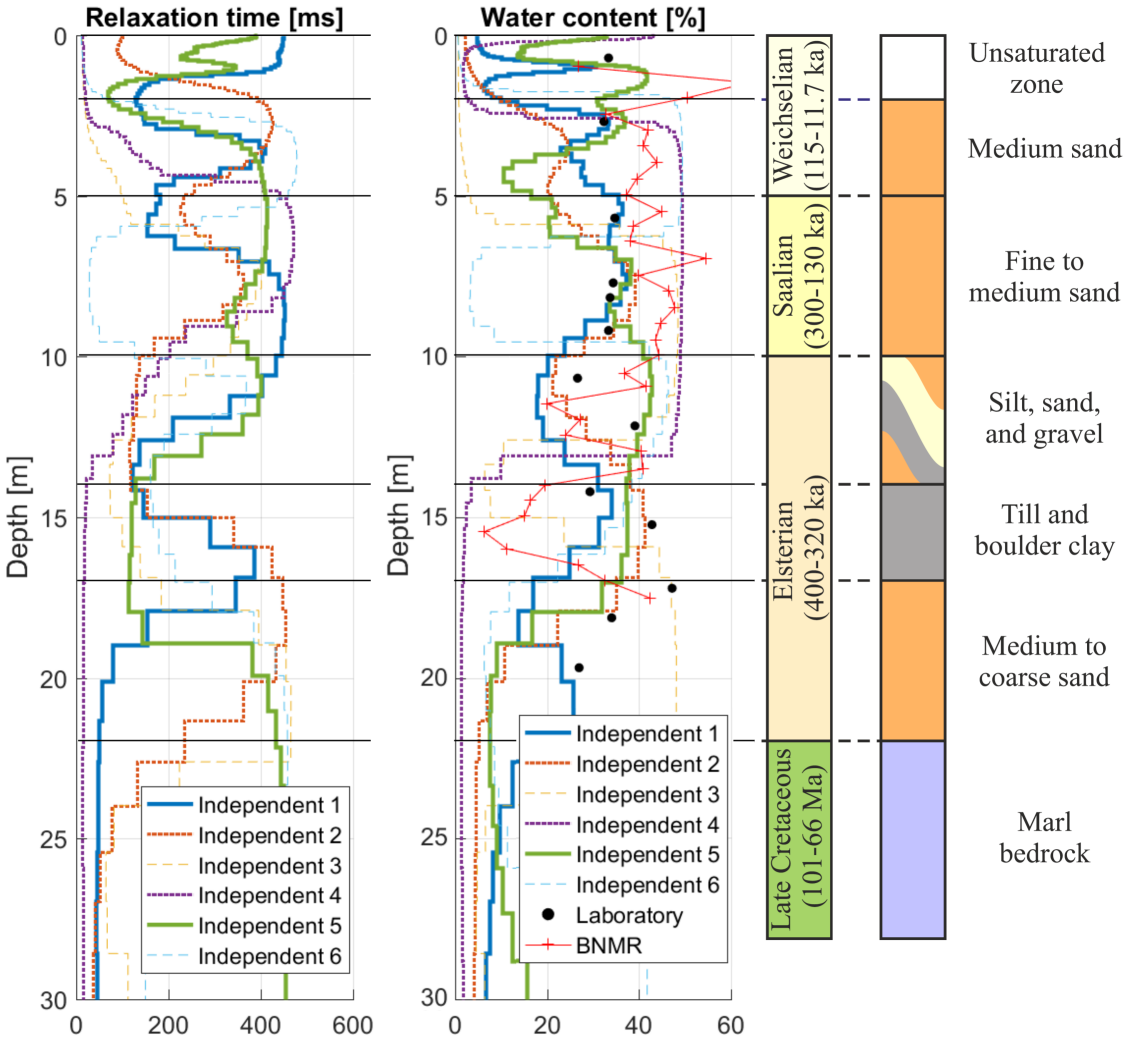

Figure 7.30: Results for the "Independent" inversions. The names of the configurations refer to names presented in Table 7.7. The results are compared to the simplified 1-D geological profile proposed by Dlugosch (2014) and laboratory and borehole measurements of the water contents exposed by Dlugosch (2014).

Name	Regularization	Noise	Error						
			Minimum		Maximum		Mean		χ^2
		nV	%	nV	%	nV	%	nV	/
Independent 1	50	28.35	1.1	0.3	1010.6	214.8	43.9	26.4	1.13
Independent 2	100	10.33	1.5	0.1	5026.9	89.8	55.3	9.5	1.09
Independent 3	25	7.59	1.0	0.1	2269.6	97.0	43.9	8.8	1.52
Independent 4	25	23.95	1.7	0.3	533.3	218.5	36.1	32.2	1.54
Independent 5	100	22.70	0.4	0.4	933.2	200.3	24.0	23.2	1.14
Independent 6	80	7.30	0.3	0.2	1557.4	104.2	54.3	20.4	3.15

Table 7.8: Characteristics of the independent inversions results. The χ^2 value is the one given by MRSmatlab and may therefore differ from the value induced by the different parameters presented in this table.

From those results, it appears that none of the inversion methods can pretend to produce a full and consistent image of the subsurface. Whereas the depth to the first aquifer is reasonably well solved in two cases ("Independent 4" and "Independent 6"), it is very badly reproduced by the four others. The "Independent 1" and "Independent 5" are the configurations classically used (hence, the same transmitter/receiver). However, it has been previously shown that the kernel corresponding to those experimental designs did not present a high sensitivity for the very first meters, hence, for the unsaturated layer. The observed high water content for the first two meters of the profile is probably due to this lack of sensitivity, resulting in the creation of artefacts. In contrast, the "Independent 3" behaviour is more problematic, as the proposed model tends to present an unsaturated zone which is thicker than what is geologically expected, whereas the sensitivity is supposedly much higher in this area due to the bimodal shape of the kernels.

However, according to Table 7.8, the results from the "Independent 6" method (30 m transmitter and 10 m receiver) are more an artefact than a result from the data. This is for example proven by the χ^2 value which is very high (3.15) but also the value of the mean error (20.4 nV) compared to the very low noise level observed on this loop. Therefore, even if the unsaturated zone seems very well solved, if no borehole was present, the operator using this configuration could not trust this result. As none of the 10 m diameter receiver loops from the experimental designs produced trustable results, which is probably due to the very low amplitude of the recorded signal and perhaps also to issues in the dataset, those two datasets are withdrawn from further interpretations. This choice is also supported by the resolution matrices, computed according to Müller-Petke and Yaramanci (2008). The matrices showed that the inversion of dataset originating from 10 m receiver loops were leading to significantly smaller confidence depth and large spreading of the resolution along the diagonal (for more details on the resolution matrices, refer to Appendix C). This means that only 9 configurations remain:

- Independent 1 : 50 m transmitter and 50 m receiver
- Independent 2 : 50 m transmitter and 30 m receiver
- Independent 4 : 30 m transmitter and 50 m receiver
- Independent 5 : 30 m transmitter and 30 m receiver
- Joint 1 : 50 m transmitter and 50 m/30 m receiver
- Joint 5 : 30 m transmitter and 50 m/30 m receiver
- General 1 : 50 m/30 m transmitter and 50 m receiver
- General 2 : 50 m/30 m transmitter and 30 m receiver
- General 4 : 50 m/30 m transmitter and 50 m/30 m receiver

7.3.2.2 Joint inversion: 1 transmitter/multiple receivers

The results of the two remaining joint inversions are presented in Figure 7.31. The corresponding parameters are presented in Table 7.9.

Name	Regularization	Noise	Error						
			Minimum		Maximum		Mean		χ^2
		nV	%	nV	%	nV	%	nV	/
Joint 1	150	19.34	1.3	0.1	4862.1	225.2	51.0	18.7	1.15
Joint 5	200	23.32	0.5	0.2	784.2	238.4	34.7	33.9	1.69

Table 7.9: Characteristics of the joint inversions results. The χ^2 value is the one given by MRSmatlab and may therefore differ from the value induced by the different parameters presented in this table.

From both inversions, multiple structures are observed. The depth to the saturated zone seems reasonably solved (the interface is placed 0.5 meter higher than the measured depth to the aquifer issued from the borehole but this remains in a reasonable range for seasonal variations (Dlugosch, 2014)). Moreover, other structures are observed in Figure 7.31. For example, the transition between the Saalian and the Elsterian is well marked in the "Joint 1" configuration. One could also argue that the interface between the clayey layer and the medium to coarse sand is observable in both "Joint 1" and "Joint 5" configurations.

Globally, none of those inversions provides a satisfactory profile. Both spot the presence of the unsaturated layer relatively precisely (even if the associated relaxation time does not converge to a unique value). On the other hand, the clayey layer (Elsterian) results in mitigated distributions. It is observed that the water content of this layer is not significantly different from the other layer; however, the relaxation time is drastically reduced, which is consistent with the physics of the problem. Moreover, compared to the previously obtained

profiles using the "Independent" inversions, the results tend to converge towards similar profiles, which is consistent since the profile is supposed to be exactly the same.

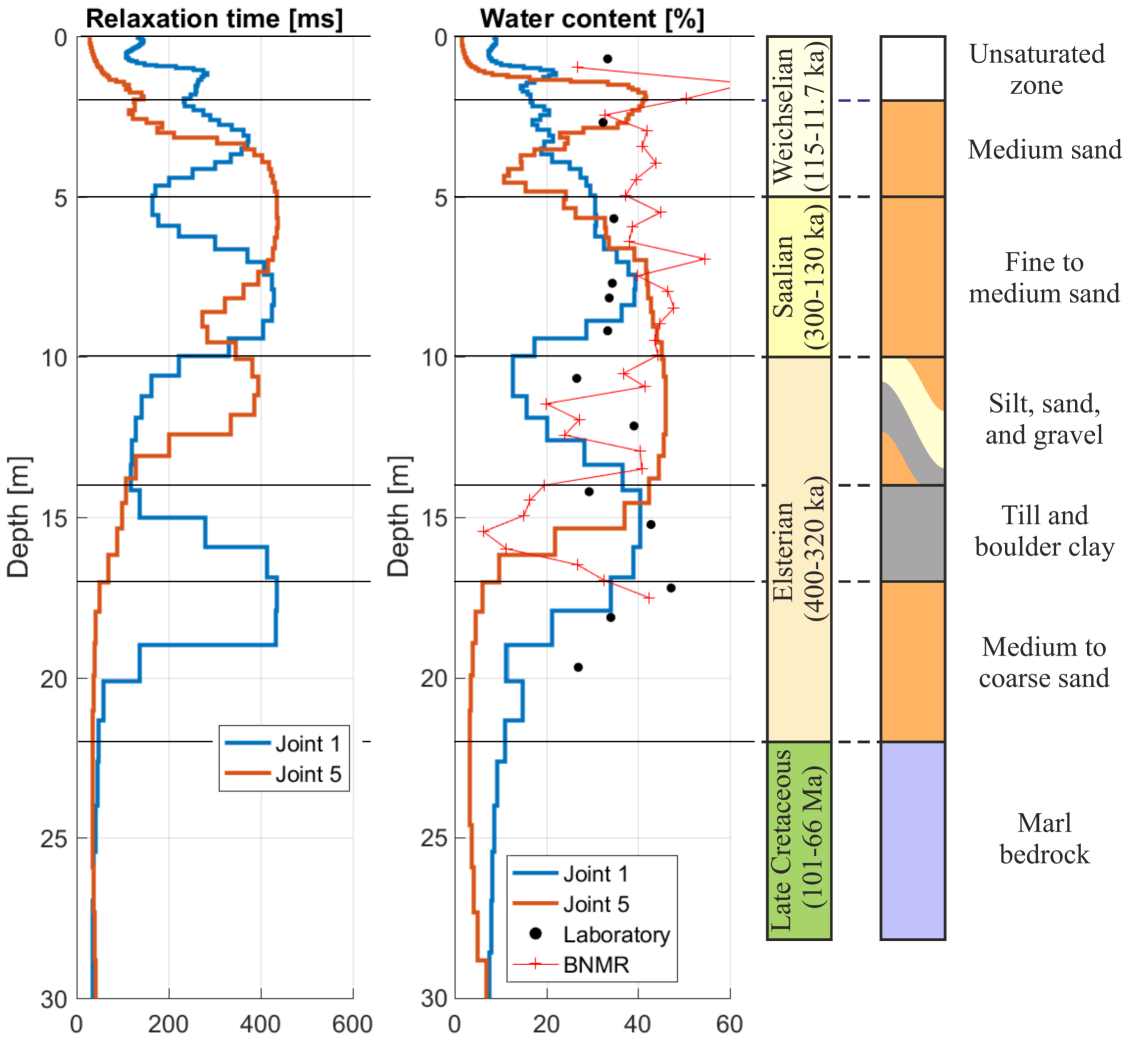

Figure 7.31: Results for the "Joint" inversions. The names of the configurations refer to names presented in Table 7.7. The results are compared to the simplified 1-D geological profile proposed by Dlugosch (2014) and laboratory and borehole measurements of the water contents exposed by Dlugosch (2014).

7.3.2.3 General inversion: multiple transmitters/multiple receivers

Name	Regularization	Noise	Error						
			Minimum		Maximum		Mean		χ^2
		nV	%	nV	%	nV	%	nV	/
General 1	50	25.90	1.4	0.3	1586.0	220.5	40.3	32.4	1.48
General 2	350	17.35	0.5	0.2	6369.1	180.0	48.4	22.1	1.43
General 4	500	21.62	0.6	0.1	5192.7	266.8	45.9	29.9	1.58

Table 7.10: Characteristics of the general inversions results. The χ^2 value is the one given by MRSmatlab and may therefore differ from the value induced by the different parameters presented in this table.

Three "General" inversions are proposed:

- General 1 : 50 m/30 m transmitter and 50 m receiver
- General 2 : 50 m/30 m transmitter and 30 m receiver
- General 4 : 50 m/30 m transmitter and 50 m/30 m receiver

Each of those inversions produces different results presented in Figure 7.32 with the corresponding characteristics in Table 7.10.

The results are very similar whatsoever the dataset used, at the exception of the relaxation time of the lower part. The "General 2" and "General 4" cases are the most precise to determine transitions. The "General 1" seems slightly worse, with the beginning of the saturated layer displaced lower and the transition between the clayey layer and the sand from the Elsterian slightly upward.

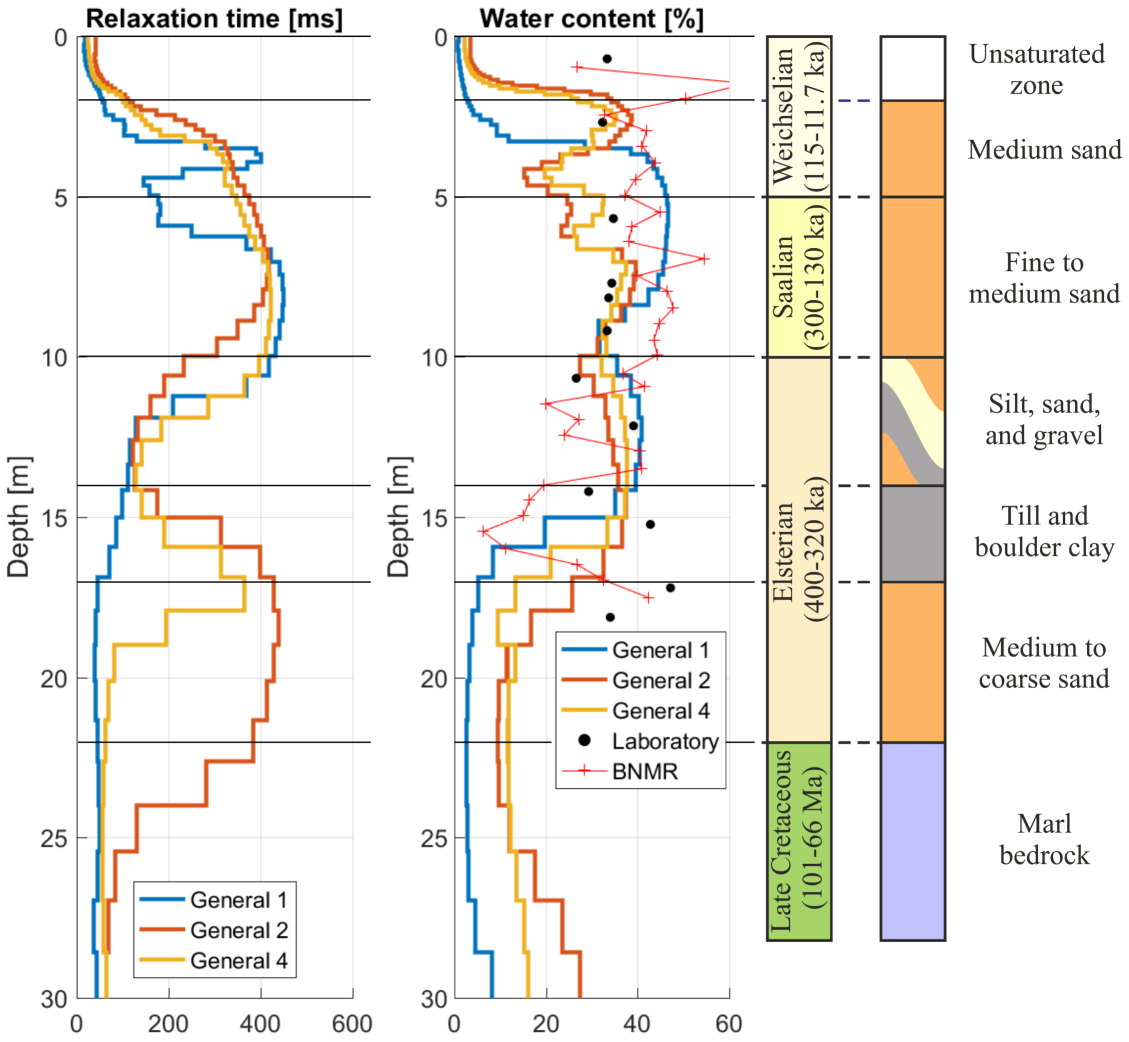

Figure 7.32: Results for the "General" inversions. The names of the configurations refer to names presented in Table 7.7. The results are compared to the simplified 1-D geological profile proposed by Dlugosch (2014) and laboratory and borehole measurements of the water contents exposed by Dlugosch (2014).

7.3.3 PFA imaging

In order to perform a PFA imaging on the Schillerslage dataset, it is first required to define the prior model space. This is done using the data from the borehole. An uncertainty on the thickness of the layers is set to +/- 2 meters (at the exception of the unsaturated layer, for which the uncertainty had been set to +/- 1 meter). The other parameters are chosen in a reasonable range according to the available data. A description of the prior model space is presented in Figure 7.33

A sampling was then made in the model space. Five thousand models were randomly sampled using the latin-hypercube sampler, ensuring a good coverage of the whole model space. The different configurations made in the Subsection 7.3.2 are repeated in this part of the work. Hence, nine imagings are performed: 4 "Independent" configurations, 2 "Joint" and 3 "General" (for more details on the names and corresponding characteristics of the used configurations, refer to Table 7.7).

The PFA imaging was performed with the same parameters for each type of configuration:

- The data were used in absolute value (amplitude of the signal)
- The resistivity was set in the kernels and has not been re-computed for each model
- The models parameters were not reduced using PCA (cfr. issue with the load given to the water content discussed in Chapter 5, Section 5.2)
- When the dataset falls outside the explored space in CCA-space, the full distribution is used (no reduction)

7.3.3.1 Independent: 1 transmitter/1 receiver

The results of the prediction-focused approach imaging on the independent datasets is presented in Figure 7.34.

Those results showed that the main outcome of the process is to transform the uniformly distributed variables from the prior model space into Gaussian (or Gaussian-like) distributions. Basically, few to no reduction of the possible ranges of values for the parameters is observed, but in each and every case, the distribution is centered (not necessarily on the mean value of the prior distribution) and there is a reduction of the standard deviation.

For some of the parameters, the obtained distributions are very similar whatever the used dataset. This is the case for the characteristics of the first layer (the unsaturated part of the log) and for the thickness of the layers at the exception of the first. On the other hand, the resulting distributions for the remaining parameters are spread along the possible values. Sometimes, different configurations converge towards similar distributions,

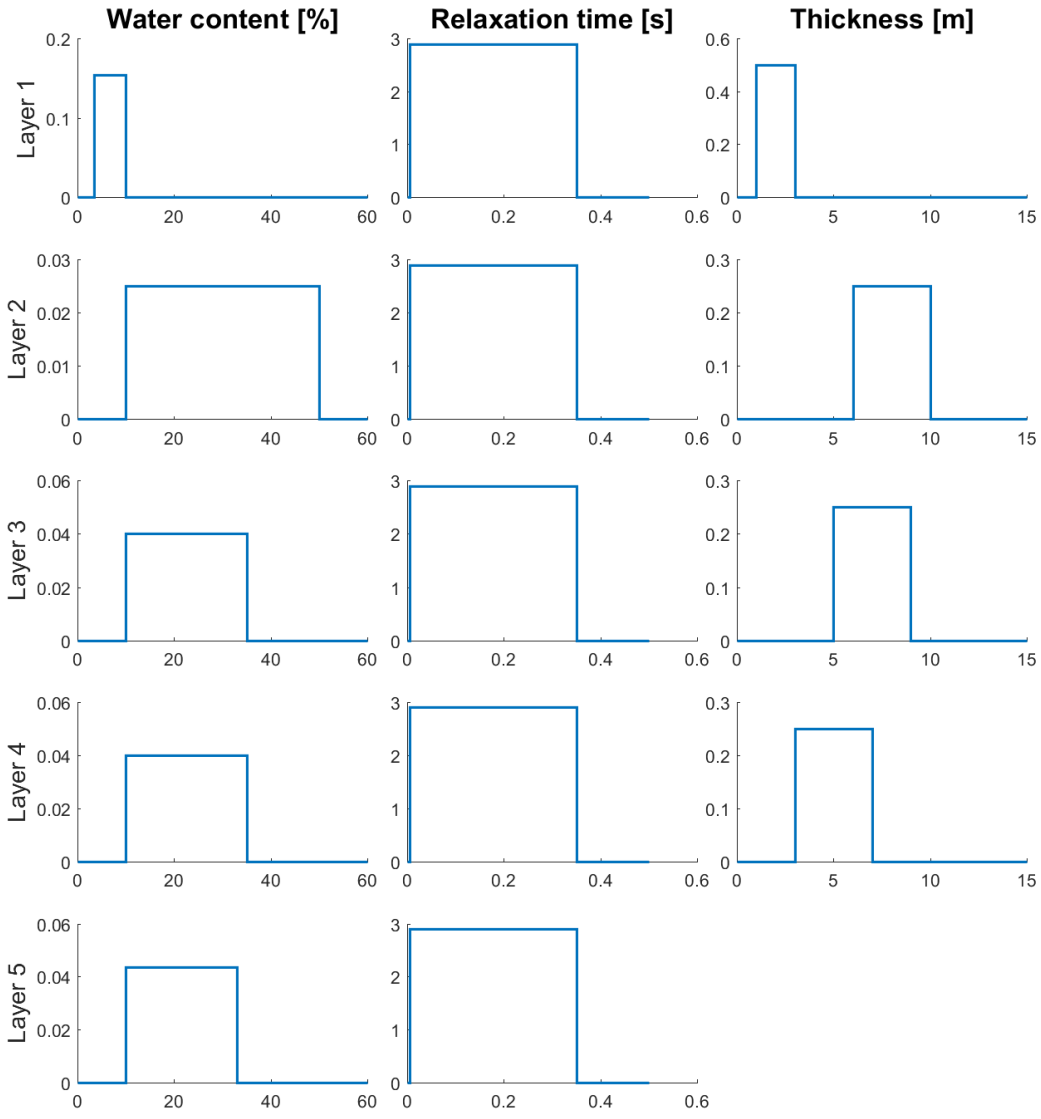

Figure 7.33: Description of the prior model space inspired by the knowledge of the geology of the site and informations from the deterministic inversions.

but globally, different datasets provide different distributions. Otherwise, it is important to notice that all the obtained distributions are somewhat overlapping, which is absolutely required since they all represent the same parameter.

In a nutshell, the obtained distributions can be summed up in terms of mean values and standard deviations (assuming a Gaussian distribution). This is presented in Table 7.11.

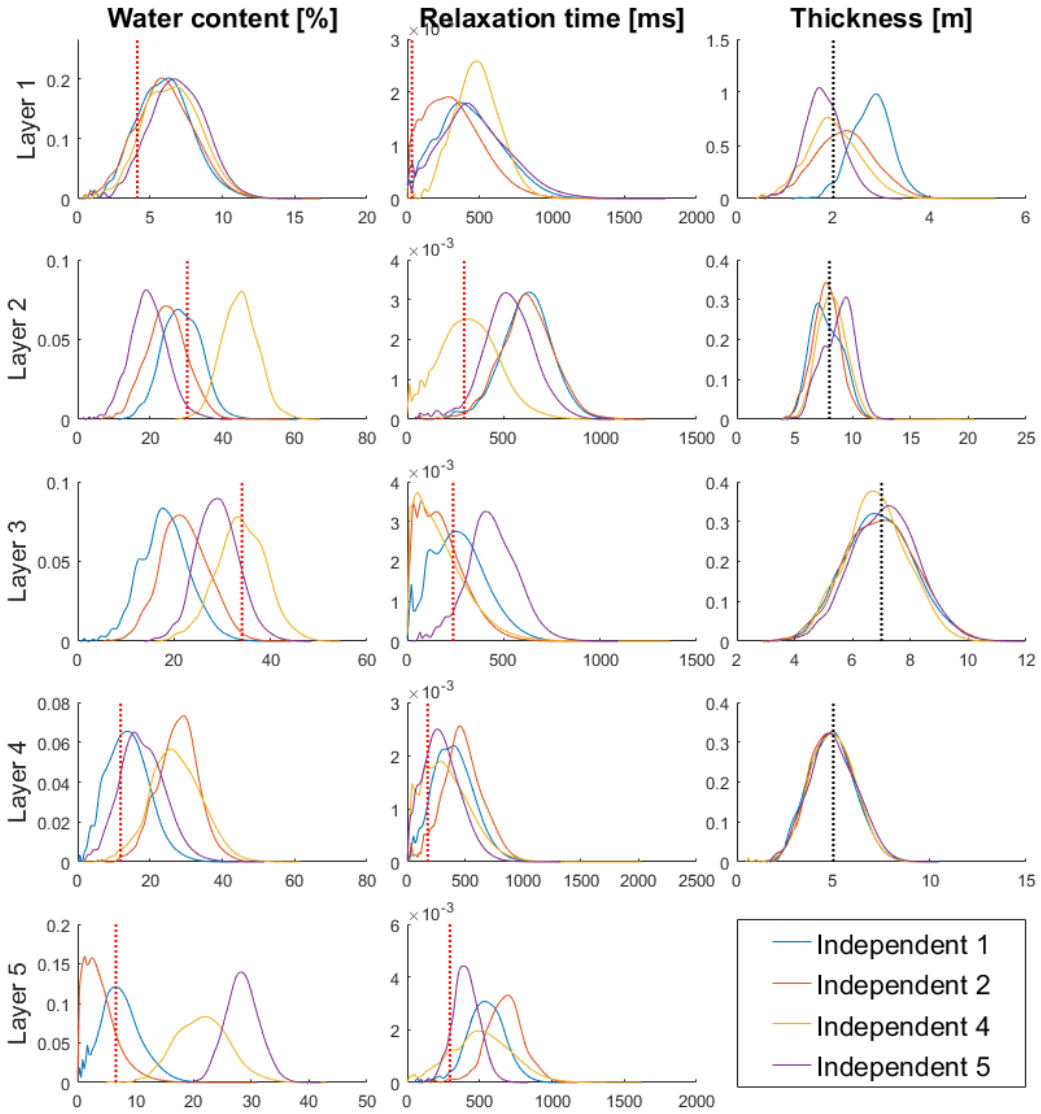

Figure 7.34: Results for the "Independent" configurations using the PFA imaging process. The names of the configurations refer to names presented in Table 7.7. The dashed black lines in the thickness column represent the depth obtained from boreholes in the surrounding. The dashed red lines in the water content and relaxation time columns represents the approximated value obtained through the QT-inversion.

The Gaussian character of the distributions is tested using a "One-sample Kolmogorov-Smirnov test" (Massey, 1951). Table 7.11 enhances the observed disparities between the different configurations, with similar standard deviations for each parameter but somehow different mean values.

Name	Independent 1		Independent 2		Independent 4		Independent 5	
	Mean	Std	Mean	Std	Mean	Std	Mean	Std
W_1 [/]	0.0619	0.0153	0.0588	0.0175	0.0633	0.0134	0.0722	0.0190
W_2 [/]	0.1411	0.0493	0.2264	0.0497	0.4381	0.0576	0.1456	0.0515
W_3 [/]	0.0939	0.0614	0.1018	0.0584	0.3508	0.1054	0.2323	0.0570
W_4 [/]	0.0843	0.0592	0.2805	0.0788	0.3030	0.0974	0.1313	0.0753
W_5 [/]	0.0440	0.0342	0.0516	0.0420	0.3299	0.0418	0.2813	0.0468
$T^*_{2,1}$ [ms]	229.8733	109.4502	196.6098	103.9810	179.6282	93.2683	228.9658	111.3608
$T^*_{2,2}$ [ms]	145.5474	63.7455	400.1678	58.6325	479.9594	83.5481	194.1114	98.0162
$T^*_{2,3}$ [ms]	96.2625	63.8813	269.9411	78.8953	352.0178	99.0763	333.9914	77.1320
$T^*_{2,4}$ [ms]	98.8175	68.2816	220.0207	96.2240	211.6924	96.3135	187.5569	86.5770
$T^*_{2,5}$ [ms]	315.9668	68.3233	283.3383	54.9341	157.0893	54.8658	140.3315	62.1770
e_1 [ms]	1.7224	0.5553	2.1027	0.5666	1.8001	0.5463	1.2203	0.3802
e_2 [m]	8.0296	1.2060	8.0200	1.2107	8.0335	1.1679	7.9329	1.2448
e_3 [m]	7.3131	1.0961	7.1839	1.0956	6.8713	1.1578	6.9174	1.1260
e_4 [m]	4.9052	1.1006	5.1364	1.1396	4.9199	1.1857	5.1988	1.1497

Table 7.11: Results from the "Independent" PFA imaging: characteristics of the posterior distributions of parameters. The red values correspond to non-Gaussian distributions ("One-sample Kolmogorov-Smirnov test" with significance level of 5%).

7.3.3.2 Joint: 1 transmitter/multiple receivers

The two joint configurations results are presented in Figure 7.35. Globally, there is less spreading of the obtained values. The obtained distributions are closer one-another and they are restrained to smaller ranges. This is presented in Table 7.12. The standard deviation is globally smaller for most of the parameters. This proves that the use of multiple datasets at once enables to better restrain the possible values of the parameters, especially for the relaxation time.

Again, the spreading is larger for the relaxation time than for the other parameters. This could signify that the experiment, even if highly controlled by this last parameter, could not provide a reasonable range for this parameter, hence is not sensitive enough. This may be due to the noise level, which enables the presence of models with relatively larger distributions and an obtained error still below the noise level.

It is also observed that the thickness of the first layer is mostly overestimated in both

cases. Otherwise, the thickness of the other layers is relatively well estimated with consistent distributions centered on the values measured in the boreholes. The distributions for the water content are also closer, depending on the configuration, than in the "Independent" configurations. The distributions for the water content are much closer for the shallowest parts than for the least sensitive, in-depth, layers.

Name	Joint 1		Joint 5	
	Mean	Std	Mean	Std
W_1 [/]	0.0579	0.0184	0.0590	0.0157
W_2 [/]	0.2793	0.0507	0.2287	0.0495
W_3 [/]	0.1012	0.0592	0.1280	0.0559
W_4 [/]	0.1045	0.0617	0.1922	0.0882
W_5 [/]	0.0411	0.0340	0.2088	0.0506
$T^*_{2,1}$ [ms]	170.0767	95.7939	135.4757	85.7335
$T^*_{2,2}$ [ms]	440.3852	60.2151	171.9341	91.1135
$T^*_{2,3}$ [ms]	260.8610	75.6438	372.8993	73.8005
$T^*_{2,4}$ [ms]	318.2677	84.2818	207.5173	98.3966
$T^*_{2,5}$ [ms]	238.4132	54.2860	165.9978	75.7185
e_1 [m]	2.8475	0.3835	2.5039	0.3358
e_2 [m]	8.0177	1.2167	7.9867	1.2271
e_3 [m]	7.0238	1.1960	6.6813	0.9043
e_4 [m]	4.9964	1.1969	5.1543	1.2143

Table 7.12: Results from the "Joint" PFA imaging: characteristics of the posterior distributions of parameters. The red values correspond to non-Gaussian distributions ("One-sample Kolmogorov-Smirnov test" with significance level of 5%).

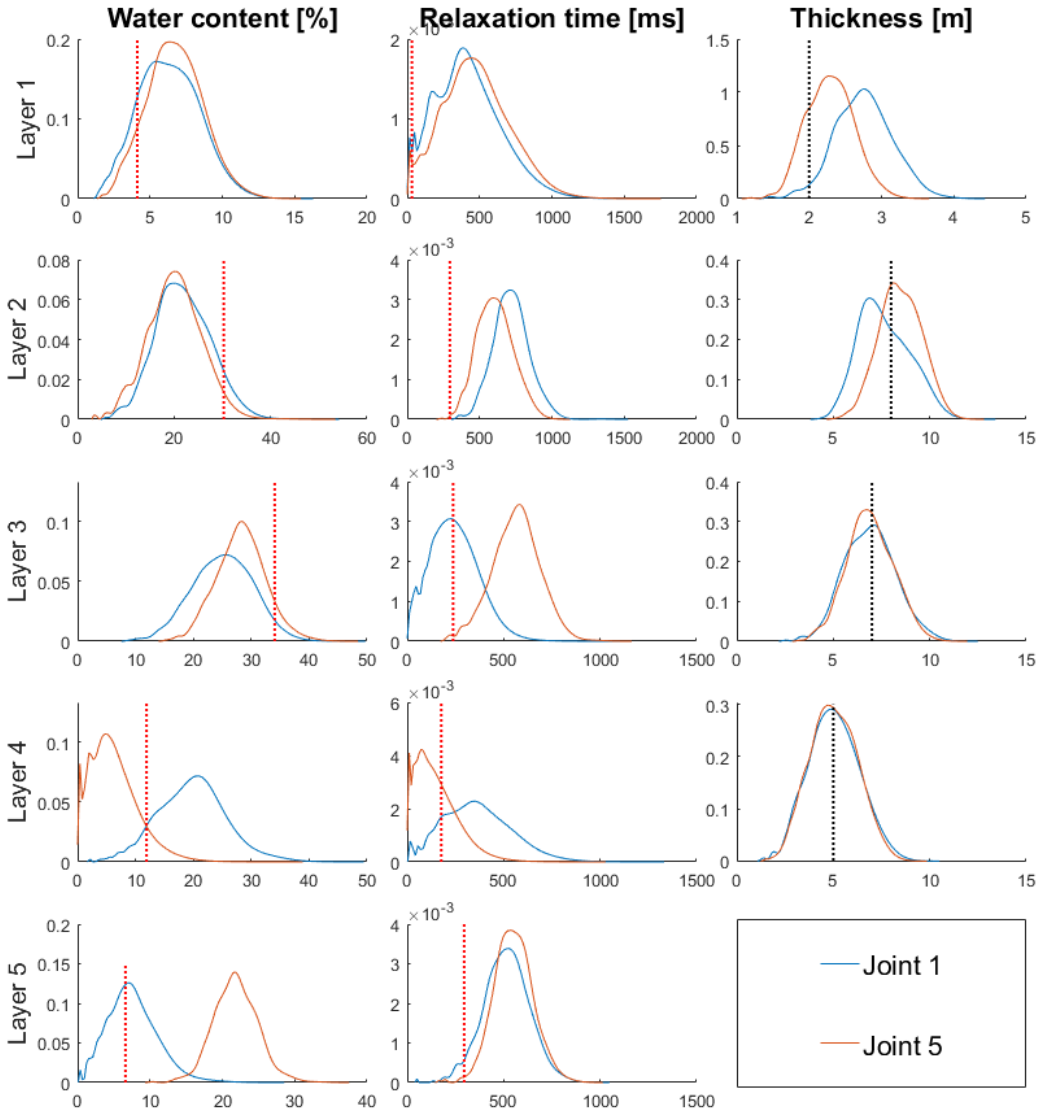

Figure 7.35: Results for the "Joint" configurations using the PFA imaging process. The names of the configurations refer to names presented in Table 7.7. The dashed black lines in the thickness column represent the depth obtained from boreholes in the surrounding. The dashed red lines in the water content and relaxation time columns represents the approximated value obtained through the QT-inversion.

7.3.3.3 General: multiple transmitters/multiple receivers

The results from those three configurations are presented in Figure 7.36. The characteristics of the distributions are presented in Table 7.13. The results appear very similar to the ones obtained with the "Joint" inversion, with the exception that now, some spreading of the values is observed. The "General 4" distributions appear to be the closest to the distributions obtained in the "Joint" configurations, meaning that the addition of a second transmitter to the dataset is probably not that informative compared to the first transmitter.

Name	General 1		General 2		General 4	
	Mean	Std	Mean	Std	Mean	Std
W_1 [/]	0.0649	0.0142	0.0695	0.0194	0.0595	0.0184
W_2 [/]	0.3118	0.0557	0.1411	0.0482	0.2485	0.0488
W_3 [/]	0.0644	0.0487	0.2015	0.0567	0.1226	0.0598
W_4 [/]	0.2254	0.0784	0.1724	0.0720	0.0872	0.0575
W_5 [/]	0.0786	0.0447	0.1126	0.0465	0.0552	0.0368
$T^*_{2,1}$ [ms]	87.8501	62.8548	227.4293	113.7065	155.9846	93.8796
$T^*_{2,2}$ [ms]	270.2070	96.8257	365.5081	49.6566	392.8048	51.3491
$T^*_{2,3}$ [ms]	101.0280	59.9339	358.2498	74.9690	354.3126	72.6487
$T^*_{2,4}$ [ms]	196.5505	85.5137	279.6420	89.4141	161.4683	81.0649
$T^*_{2,5}$ [ms]	206.4122	83.3995	220.0561	59.2157	229.6353	58.0003
e_1 [m]	1.8120	0.4218	1.4890	0.4916	2.6672	0.3886
e_2 [m]	9.2524	0.9464	8.0290	1.1677	8.0034	1.2172
e_3 [m]	6.5330	0.9505	7.0590	1.2266	7.0881	1.1222
e_4 [m]	4.9738	1.0831	5.1923	1.1679	5.0618	1.1859

Table 7.13: Results from the "General" PFA imaging: characteristics of the posterior distributions of parameters. The red values correspond to non-Gaussian distributions ("One-sample Kolmogorov-Smirnov test" with significance level of 5%).

If we compare the obtained spreading of the different configurations used, it appears that, for most of the parameters, the standard deviations of the distributions are diminished with the larger datasets, proving the advantage of the multiple loops configuration. This is done in Figure 7.37, where the mean standard deviation for each cluster of configuration ("Independent", "Joint" and "Global") is used as an indicator of the spreading. The values are compared to the value corresponding to the prior standard deviation. It appears that most of the parameters benefit from the larger constraints offered by multiple loops datasets. Even better, when the spreading tends to increase, it is in much smaller amplitudes than when it decreases (at the exception of the relaxation time).

As a conclusion, it seems that the "Global" configuration method is the one that offers posterior distributions with less uncertainty, even if the "Joint" configuration already significantly improves the possible ranges.

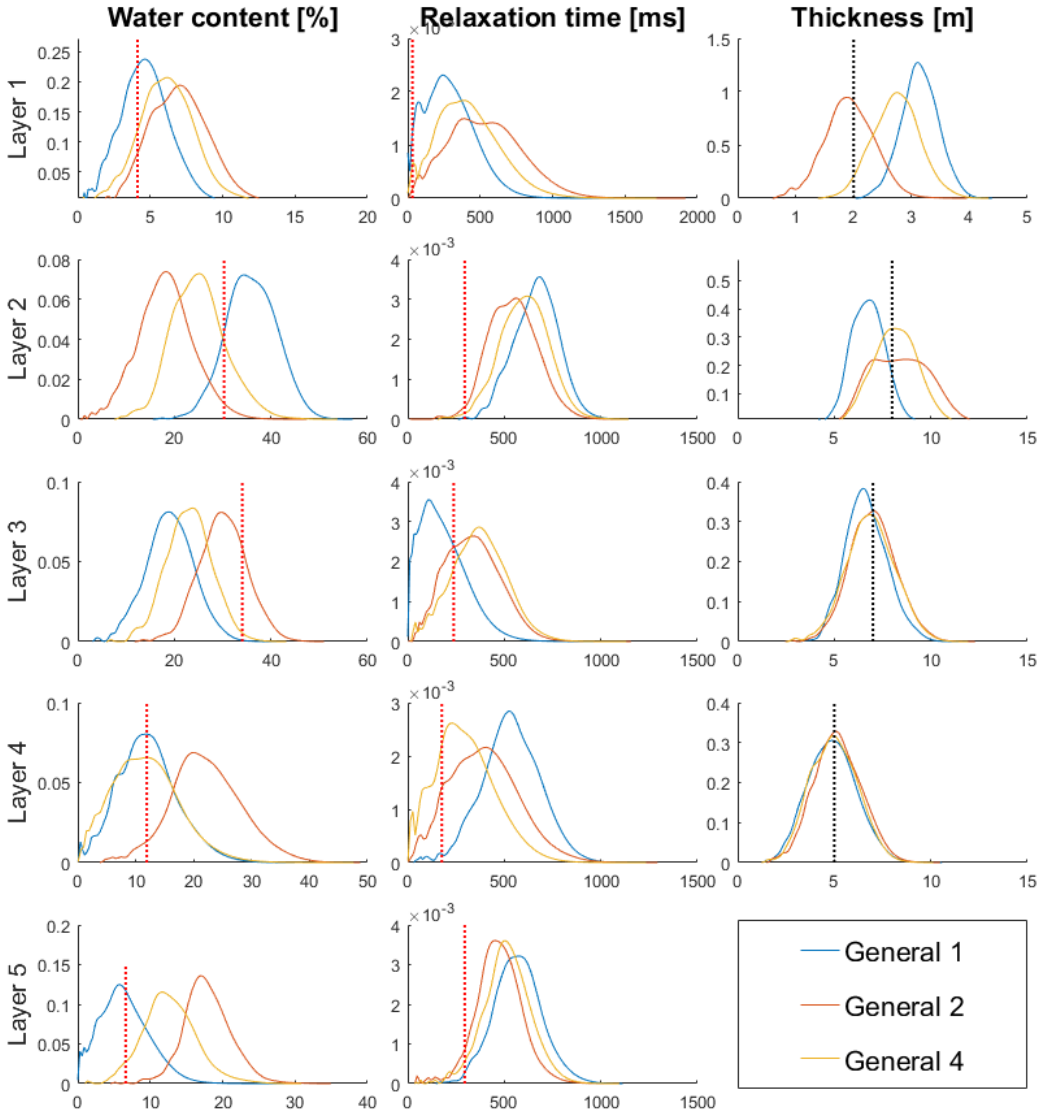

Figure 7.36: Results for the "General" configurations using the PFA imaging process. The names of the configurations refer to names presented in Table 7.7. The dashed black lines in the thickness column represent the depth obtained from boreholes in the surrounding. The dashed red lines in the water content and relaxation time columns represents the approximated value obtained through the QT-inversion.

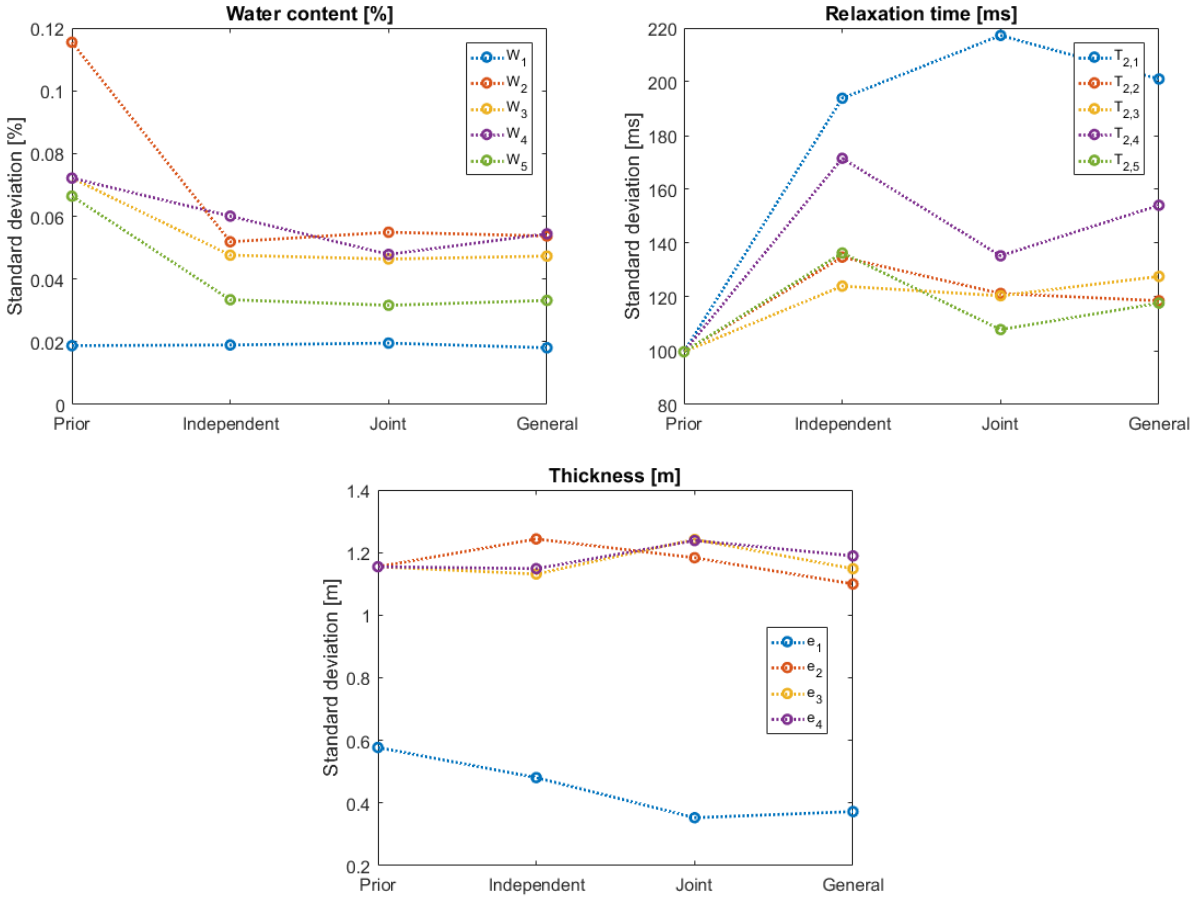

Figure 7.37: Evolution of the spreading with the configuration. Top left: water content, Top right: relaxation time and Bottom: thickness.

7.3.4 Discussion

Figures summarizing the different results are presented in Figures 7.38 and 7.39 along with groundtruth data from Dlugosch (2014). From Figure 7.38, it is easily observed that the "General 4" configuration is the one that performs best. It produces a well-marked first unsaturated layer consistent with the knowledge of the site. Moreover, the remaining part of the distribution is more comparable to the results obtained by Dlugosch (2014) on the same site, both in terms of water content and relaxation time. On the other hand, the gains observed between the "Independent 1" and "Joint 1" inversions are difficult to assess. It seems that the addition of the smaller receiver loop tends to better constrain the water table by reducing the water content of the first meters, but otherwise, the results are very similar in terms of water content. Again, in terms of relaxation time, the "Joint 1" inversion presents lower values for the first meters. This is probably the effect of the smaller loop. In conclusion, for the QT inversion, it appears that the addition of specific loops, sensitive to specific aspects of the model, are beneficial.

The PFA imaging process (Figure 7.39) shows similar results. However, improvements, in terms of uncertainty reduction, due to the addition of loops in the dataset are barely noticeable when directly observing the distributions. The use of the graphs representing the evolution of the standard deviation from the obtained distributions is more convenient in order to analyze the specific advantages of the different configurations (Figure 7.37). From those graphs, it appears that the standard deviation tends to globally decrease when a large dataset is used, meaning that the use of multiple transmitter/receiver loops is beneficial to better constrain the uncertainty on the different parameters. However, it also appears that, for some parameters, the effect of the addition of transmitter/receiver loops is reversed and an increase of the standard deviation is observed. This is probably linked to the fact that some datasets are less sensitive to those parameters, and therefore their addition in the process does not improve the reduction of uncertainty. This is mostly the case for the in-depth layers, were inner loops show few sensitivity (see the sensitivity kernels, Section 7.3.1). Nonetheless, those increases are significantly lower than the decreases. On the other hand, the dramatic increase of uncertainty observed for the relaxation time of the first layer is due to a relative insensitivity of the experiment to this parameter, linked to the low water content in this layer (Appendix B).

As a conclusion, the results from the addition of transmitter/receiver loops is mitigated for the PFA imaging process. Even though, the parameters that benefit from the addition of sensitive couples are mainly observed in very sensitive areas of the subsurface (i.e. large extent layers with high water content at an intermediate depth). On the other hand, it appears that the water content is always better solved than the relaxation time.

Finally, the results of the QT inversion are very difficult to compare to the results of the PFA imaging, due to the different nature of the emerging image of the subsurface. It is reassuring to observe that the results of the QT inversion are always contained inside

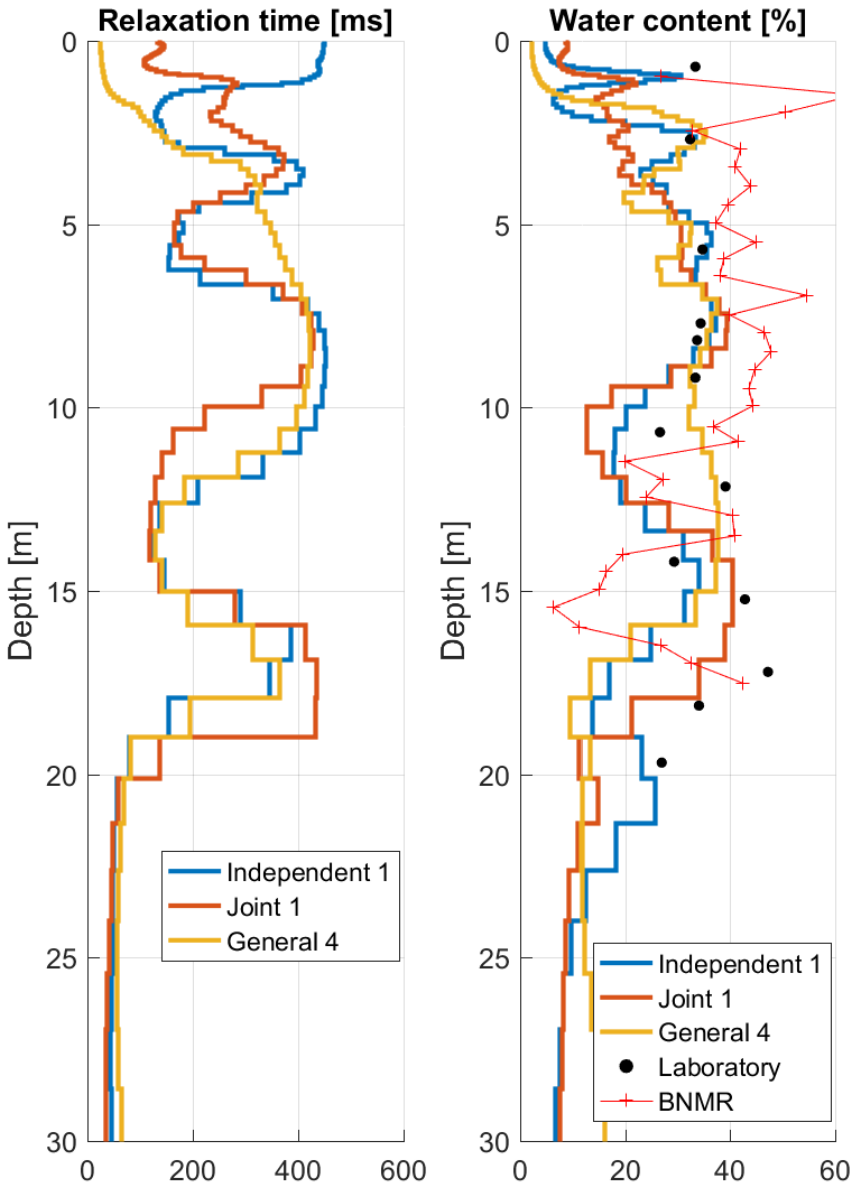

Figure 7.38: Comparison of the main QT inversion results. The "Independent 1" inversion corresponds to the commonly applied experimental design, with a 50 m transmitter/receiver loop. The "Joint 1" inversion is the first multiple loops approach: one 50 m transmitter with two receivers (50 and 30 m diameter). Finally, the "General 4" inversion constitutes the most general inversion carried on in this project: two transmitter loops (50 and 30 m diameter) coupled with two receiver loops (50 and 30 m diameter). The results are compared to laboratory measurements of the water contents (black dots) exposed by Dlugosch (2014).

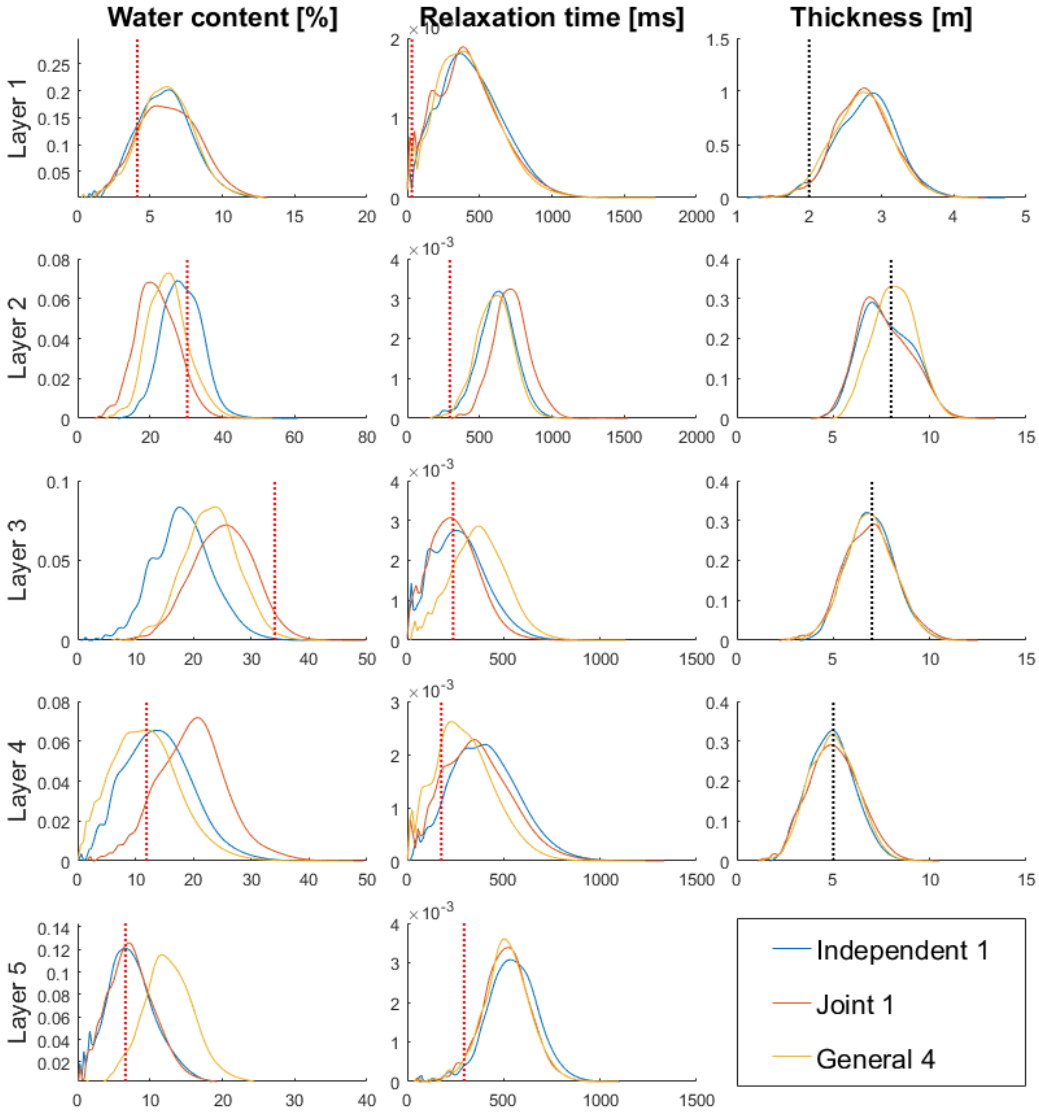

Figure 7.39: Comparison of the main PFA imaging results. The "Independent 1" configuration corresponds to the commonly applied experimental design, with a 50 m transmitter/receiver loop. The "Joint 1" configuration is the first multiple loops approach: one 50 m transmitter with two receivers (50 and 30 m diameter). Finally, the "General 4" configuration constitutes the most general inversion carried on in this project: two transmitter loops (50 and 30 m diameter) coupled with two receiver loops (50 and 30 m diameter). The dashed black lines in the thickness column represent the depth obtained from boreholes in the surrounding. The dashed red lines in the water content and relaxation time columns represents the approximated value obtained through the QT-inversion.

the obtained ranges of possibilities from the PFA imaging (with the exception of the first unsaturated layer, absent of most of the "Independent" and "Joint" inversions). However, the two approaches showed complementarity. The PFA imaging proposed a way to retrieve a full posterior distribution of parameters. This result is more complete than the results obtained from the QT inversion (a deterministic approach), but this also means that those results are more complex to integrate. Albeit simpler to interpret, the results of the QT inversion relies on a highly discussed parameter: the regularization parameter. This latter guarantees a smoother model, avoiding the creation of artefacts due to noise in the dataset. This parameter is therefore critical, but very difficult to assess objectively. The use of the L-curve criteria, even if widely spread, is not always consistent and shows mitigated results. Hence, the logs obtained from the QT inversion algorithm are still subject to a large uncertainty on this parameter. On the other hand, the PFA imaging does not require such parameters, as it only relies on the definition of a consistent prior. In terms of computation, both approaches have their strengths and weaknesses. Where the QT inversion relies on an algorithm that has evolved in the past years, hence optimized for recent computers, the PFA imaging process is still under development and therefore requires more CPU time and memory. Moreover, even if the PFA algorithm was highly optimized, it will still require larger amounts of CPU time and memory than the QT inversion, due to the use of very large datasets.

Chapter 8

Conclusion

This work has developed the potential of the multiple loops SNMR experimental configuration. This configuration benefits from the increased sensitivity to shallow subsurface of coaxial loops while conserving the information issued from the classical coincident loops. In order to benefit from this configuration, an adaptation of the state-of-the-art QT inversion scheme has been developed to enable the use of larger datasets originating from those hybrid datasets (Chapter 6).

On the other hand, a new innovative method to interpret SNMR data has been proposed: the prediction-focused approach (PFA) imaging. This latter is the prediction part of a larger new framework for the analysis of data: Bayesian evidential learning (BEL). This approach relies on the constitution of statistics-based relations between synthetic model parameters issued from a prior model space and their corresponding data, enabling the production of the full posterior distribution constraint to field-acquired data. As this method was never applied to SNMR data in the past, a fully functioning MATLAB code has been developed for this purpose. The different steps constituting the PFA imaging process have been detailed and discussed, with an emphasize on the divergences between the developed process and previous similar processes applied to other types of data (Hermans et al., 2016) (Chapter 5).

Then, the developed PFA scheme has been tested on several synthetic examples, demonstrating the potential of this new configuration method (Chapter 7, Section 7.1). In a nutshell, the main outcomes of those extensive analyses showed that the use of principle component analysis as a dimension reduction tool was nearly insensitive to Gaussian noise, meaning that no particular attention was needed for the treatment of noise. The method performed satisfyingly with both noise-free and noisy data. However, it appeared that the resolution of the water content and thickness of the layers was always more performing than the resolution of the relaxation time, even if a multivariate sensitivity analysis demonstrated that the experiment was highly sensitive to those parameters.

Knowing that the PFA imaging process was working correctly, the QT inversion and the PFA imaging were applied to a synthetic noisy multiple loops dataset. It demonstrated that the developed schemes adapted for the use of those particular datasets were consistent and that both methods performed satisfyingly. For this dataset, "Independent" configurations (1 transmitter/1 receiver) and "Joint" configurations (1 transmitter/multiple receivers) were carried out successfully.

Then, the two methods were applied to a real multiple loops dataset from the Schillerslage hydrogeological test site (Section 7.3). There, the previously tested "Independent" and "Joint" configurations have been conducted with both the QT inversion and the PFA imaging and another case was added: the "General" inversion (multiple transmitters/multiple receivers). This study showed that the main advantage of the use of multiple loops configurations originates from the increased sensitivity of the dataset to the shallow layers, hence results in a better resolution for the shallowest layers.

Finally, a comparison between the different methods showed that both interpretation methods had advantages. The QT inversion results are more comprehensive compared to full posterior distributions in several parameters. However, the PFA imaging does not require the difficult determination of a regularization parameter. On computational aspects, the QT inversion is far superior albeit not producing a full posterior distribution of models. The PFA imaging requires around 10 minutes to produce 1000 models of the posterior distribution. This computation time may seem substantial but, compared to the similar process in the QT inversion (bootstrap inversion), is way better and adapted to multiple loops datasets.

Further works will consist in improvements of the PFA imaging process, and in the full development of the BEL approach to acquire/interpret SNMR data and better constrain the prior model space, crucial for the PFA imaging. On the other hand, researches should be conducted on the development of stochastic methods based on the deterministic inversion of data to assess uncertainty-based SNMR multiple loops data, via an adapted sampling scheme for the bootstrap inversion.

References

Aster, R., Borchers, B., & Thurber, C. (2013). *Parameters estimation and inverse problems* (2nd ed.). Academic Press. doi: 10.1016/C2009-0-61134-X

Behroozmand, A. A., Auken, E., Fiandaca, G., & Rejkjaer, S. (2016, April). Increasing the resolution and the signal-to-noise ratio of magnetic resonance sounding data using a central loop configuration. *Geophysical Journal International*, *205*(1), 243–256. doi: 10.1093/gji/ggw004

Behroozmand, A. A., Keating, K., & Auken, E. (2015, January). A review of the principles and applications of the NMR technique for near-surface characterization. *Surveys in Geophysics*, *36*(1), 27–85. doi: 10.1007/s10712-014-9304-0

Binot, F. (2008). *Vier neue Bohrungen im Mess- und Testgebiet des GGA-Instituts nördlich von Schillerslage bei Burgdorf, Niedersachsen.* GGA-Institut, Stilleweg 2, D-30655 Hannover. (Archive Nr.: 0 128 085)

Dlugosch, R. (2014). *Aquifer characterisation using nuclear magnetic resonance* (Doctoral dissertation, Technischen Universität Berlin, Berlin). Retrieved from `https://depositonce.tu-berlin.de/bitstream/11303/4602/2/dlugosch_raphael.pdf`

Fedi, M., Hansen, P. C., & Paoletti, V. (2005, November). Analysis of depth resolution in potential-field inversion. *GEOPHYSICS*, *70*(6), A1–A11. doi: 10.1190/1.2122408

Gilson, M., Briers, P., Ruthy, I., & Dassargues, A. (2017). *Elsenborn - Langert - Dreiherrenwald : Notice explicative.* Retrieved from `http://environnement.wallonie.be/cartosig/cartehydrogeo/document/NOTICE_5034_50A1.pdf` (OCLC: 1023843314)

Günther, T. (2004). *Inversion methods and resolution analysis for the 2D/3D reconstruction of resistivity structures from DC measurements* (Doctoral dissertation, Technischen Universität Bergakademie Freiberg, Freiberg). Retrieved from `http://citeseerx.ist.psu.edu/viewdoc/download?doi=10.1.1.473.8116&rep=rep1&type=pdf`

Günther, T., Rücker, C., & Spitzer, K. (2006, August). Three-dimensional modelling and inversion of DC resistivity data incorporating topography - II. Inversion. *Geophysical Journal International*, *166*(2), 506–517. doi: 10.1111/j.1365-246X.2006.03011.x

Grombacher, D., & Auken, E. (2018, May). Gaining insight into the T2*–T2 relationship in surface NMR free-induction decay measurements. *Geophysical Journal International*,

213(2), 1402–1411. doi: 10.1093/gji/ggy067

Hermans, T., Oware, E., & Caers, J. (2016, September). Direct prediction of spatially and temporally varying physical properties from time-lapse electrical resistance data. *Water Resources Research*, *52*(9), 7262–7283. doi: 10.1002/2016WR019126

Hertrich, M. (2005). *Magnetic Resonance Sounding with separated transmitter and receiver loops for the investigation of 2D water content distributions* (Doctoral dissertation, Technischen Universität Berlin, Berlin). Retrieved from `https://depositonce.tu-berlin.de/bitstream/11303/1340/1/Dokument_50.pdf`

Hertrich, M. (2008, November). Imaging of groundwater with nuclear magnetic resonance. *Progress in Nuclear Magnetic Resonance Spectroscopy*, *53*(4), 227–248. doi: 10.1016/j.pnmrs.2008.01.002

Holland, R., Dlugosch, R., Günther, T., Sass, S., Holzhauer, J., Sauer, J., ... Yaramanci, U. (2011). Das hydrogeophysikalische Testfeld Schillerslage. *Deutsche Geophysikalische Gesellschaft e.V. Mitteilungen*(1/2011), 51–54. Retrieved from `https://www.researchgate.net/profile/Peter_Brosche/publication/301770235_Ozeanschwingungen_und_Gezeitenreibung_-_Zur_Bewertung_von_Resonanzkurven/links/5726f3b808aef9c00b88ff95/Ozeanschwingungen-und-Gezeitenreibung-Zur-Bewertung-von-Resonanzkurven.pdf`

Jolliffe, I. (2002). *Principal Component Analysis* (2nd ed.). Springer. doi: 10.1007/b98835

Kremer, T., Michel, H., Müller-Petke, M., Irons, T., Hermans, T., Duglosch, R., & Nguyen, F. (2018, March). Improving the accuracy of 1D SNMR surveys using the multi-central-loop configuration. In *Proceedings of the 31st sageep conference, nashville (*US*).* Retrieved from `https://biblio.ugent.be/publication/8558539` (Poster presentation)

Legchenko, A., & Shushakov, O. (1998). Inversion of Surface NMR data. *Geophysics*, *63*(1), 75–84.

Legchenko, A., & Valla, P. (2002, May). A review of the basic principles for proton magnetic resonance sounding measurements. *Journal of Applied Geophysics*, *50*(1-2), 3–19. doi: 10.1016/S0926-9851(02)00127-1

Levitt, M. H. (2008). *Spin dynamics: Basics of nuclear magnetic resonance, 2nd Edition.* Wiley.

Massey, F. J. (1951, March). The Kolmogorov-Smirnov test for goodness of fit. *Journal of the American Statistical Association*, *46*(253), 68. doi: 10.2307/2280095

Matlab and statistics and machine learning toolbox. (2016a). (The MathWorks, Inc., Natick, MA, USA)

McKay, M. D., Beckman, R. J., & Conover, W. J. (1979, May). A comparison of three methods for selecting values of input variables in the analysis of output from a computer code. *Technometrics*, *21*(2), 239. doi: 10.2307/1268522

Michel, H., Nguyen, F., Kremer, T., & Hermans, T. (2018, September). The Bayesian Evidential Learning framework: A new approach to SNMR data interpretation.

Changchun (China). (Submitted extended abstract)

Müller-Petke, M. (2009). *Extended use of Magnetic Resonance Sounding (MRS) datasets - QT inversion and resolution studies* (Doctoral dissertation, Technischen Universität Berlin). Retrieved from `https://depositonce.tu-berlin.de/bitstream/11303/2548/1/Dokument_45.pdf`

Müller-Petke, M., Braun, M., Hertrich, M., Costabel, S., & Walbrecker, J. (2016, July). MRSmatlab — A software tool for processing, modeling, and inversion of magnetic resonance sounding data. *GEOPHYSICS*, *81*(4), WB9–WB21. doi: 10.1190/geo2015-0461.1

Müller-Petke, M., & Yaramanci, U. (2008, December). Resolution studies for Magnetic Resonance Sounding (MRS) using the singular value decomposition. *Journal of Applied Geophysics*, *66*(3-4), 165–175. doi: 10.1016/j.jappgeo.2007.11.004

Mohnke, O., & Yaramanci, U. (2005). Forward modeling and inversion of MRS relaxation signals using multi-exponential decomposition. *Near Surface Geophysics*, *3*(3), 165–185. doi: 10.3997/1873-0604.2005012

Mueller-Petke, M., & Yaramanci, U. (2010, July). QT inversion — Comprehensive use of the complete surface NMR data set. *GEOPHYSICS*, *75*(4), WA199–WA209. doi: 10.1190/1.3471523

Park, J., Yang, G., Satija, A., Scheidt, C., & Caers, J. (2016, December). DGSA: A Matlab toolbox for distance-based generalized sensitivity analysis of geoscientific computer experiments. *Computers & Geosciences*, *97*, 15–29. doi: 10.1016/j.cageo.2016.08.021

Roy, J., & Lubczynski, M. (2003, August). The magnetic resonance sounding technique and its use for groundwater investigations. *Hydrogeology Journal*, *11*(4), 455–465. doi: 10.1007/s10040-003-0254-8

Scheidt, C., Li, L., & Caers, J. (2018). *Quantifying uncertainty in subsurface systems* (Wiley-Blackwell ed.).

Scheidt, C., Renard, P., & Caers, J. (2015). Prediction-focused subsurface modeling: investigating the need for accuracy in flow-based inverse modeling. *Mathematical Geosciences*, *47*(2), 173–191.

Walsh, D., Turner, P., Grunewald, E., Zhang, H., Butler, J. J., Reboulet, E., ... Fitzpatrick, A. (2013, November). A small-diameter NMR logging tool for groundwater investigations. *Groundwater*, *51*(6), 914–926. doi: 10.1111/gwat.12024

Wand, M. P., & Jones, M. C. (1993, June). Comparison of smoothing parameterizations in bivariate kernel density estimation. *Journal of the American Statistical Association*, *88*(422), 520. doi: 10.2307/2290332

Wastiaux, C. (2008). Les tourbières sont-elles des éponges régularisant l'écoulement ? *BSGLg [Online]*, *50*, 10. Retrieved from `https://popups.uliege.be/0770-7576/index.php?id=1639`

Weichman, P. B., Lavely, E. M., & Ritzwoller, M. H. (2000, July). Theory of surface nuclear

magnetic resonance with applications to geophysical imaging problems. *Physical Review E*, *62*(1), 1290–1312. doi: 10.1103/PhysRevE.62.1290

Yaramanci, U., & Müller-Petke, M. (2009, October). Surface nuclear magnetic resonance—A unique tool for hydrogeophysics. *The Leading Edge*, *28*(10), 1240–1247. doi: 10.1190/1.3249781

Appendix A

Computability of kernels according to the experimental configuration

Details of the results for the kernels computability are presented in this appendix. The blue dots represent successful attempts to compute the kernel for the given configuration (size of transmitter/receiver and multiplier applied to the transmitter size to obtain the maximal depth of the kernel).

The results show two cases where the computation of the kernel is impossible:

- A much too small maximal depth (multiplier = 0.1)
- A too large maximal depth for the receiver size

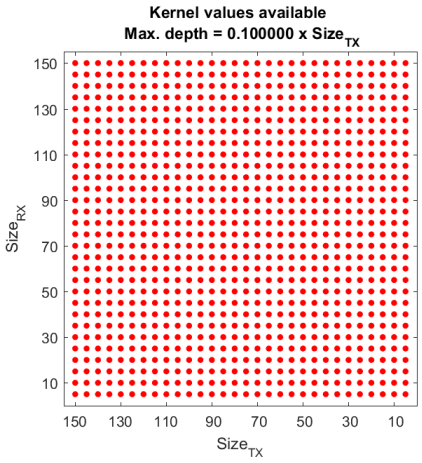

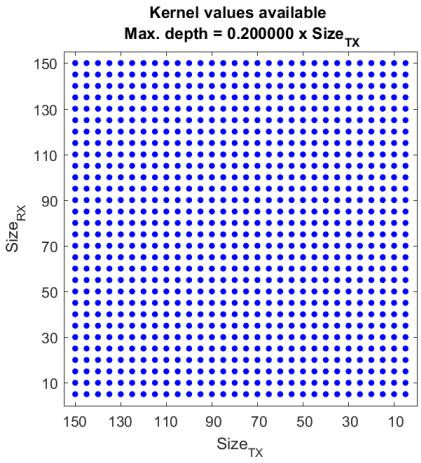

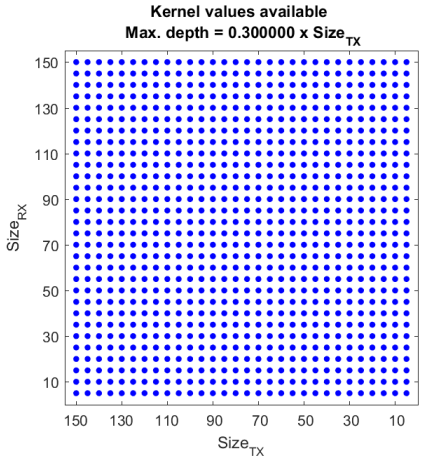
Kernel values available
Max. depth = 0.300000 x Size$_{TX}$
Size$_{RX}$
Size$_{TX}$
150 130 110 90 70 50 30 10

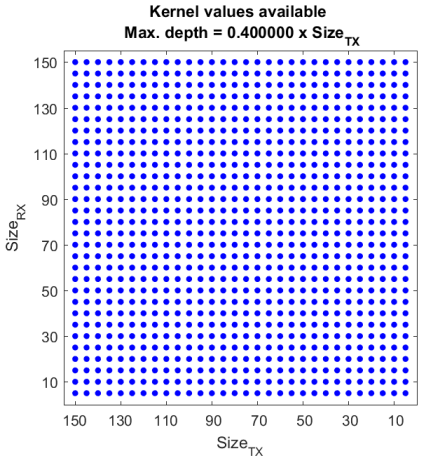
Kernel values available
Max. depth = 0.400000 x Size$_{TX}$
Size$_{RX}$
Size$_{TX}$
150 130 110 90 70 50 30 10

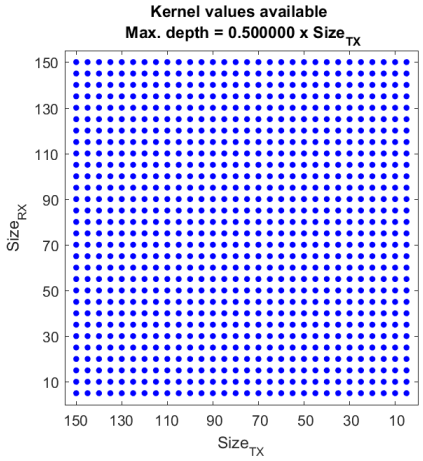
Kernel values available
Max. depth = 0.500000 x Size$_{TX}$
Size$_{RX}$
Size$_{TX}$
150 130 110 90 70 50 30 10

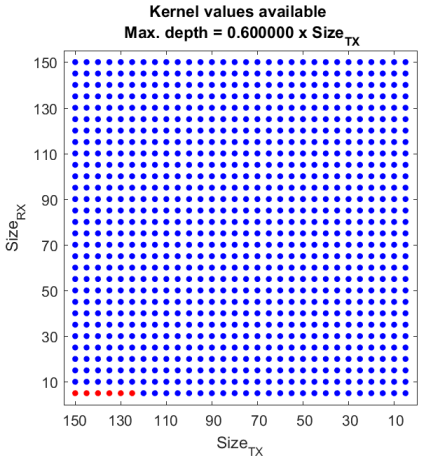
Kernel values available
Max. depth = 0.600000 x Size$_{TX}$
Size$_{RX}$
Size$_{TX}$
150 130 110 90 70 50 30 10

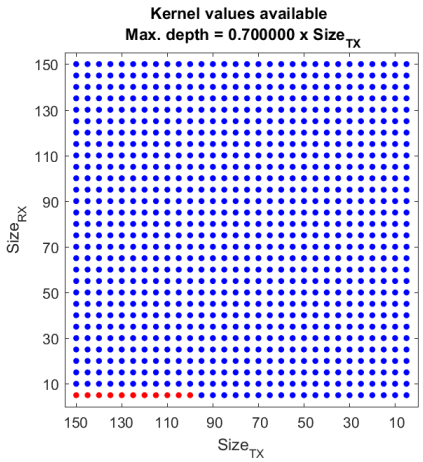
Kernel values available
Max. depth = 0.700000 x Size$_{TX}$
Size$_{RX}$
Size$_{TX}$
150 130 110 90 70 50 30 10

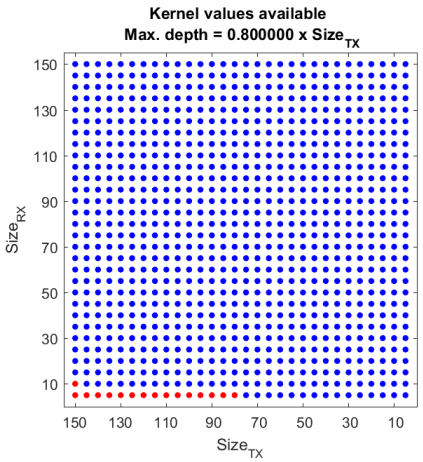
Kernel values available
Max. depth = 0.800000 x Size$_{TX}$
Size$_{RX}$
Size$_{TX}$
150 130 110 90 70 50 30 10

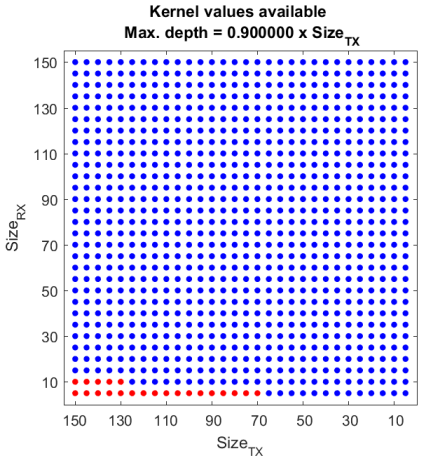
Kernel values available
Max. depth = 0.900000 x Size$_{TX}$
Size$_{RX}$
Size$_{TX}$
150 130 110 90 70 50 30 10

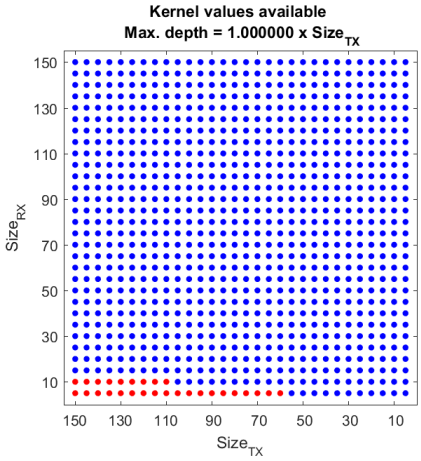
Kernel values available
Max. depth = 1.000000 x Size$_{TX}$
Size$_{RX}$
Size$_{TX}$
150 130 110 90 70 50 30 10

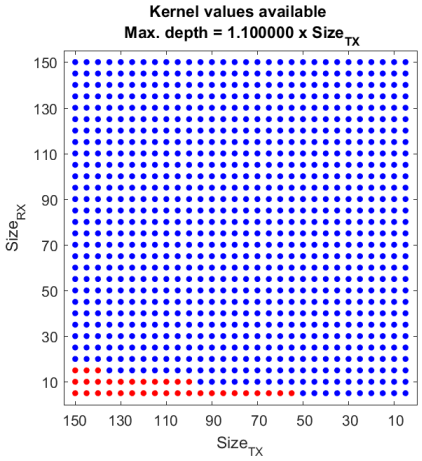
Kernel values available
Max. depth = 1.100000 x Size$_{TX}$
Size$_{RX}$
Size$_{TX}$
150 130 110 90 70 50 30 10

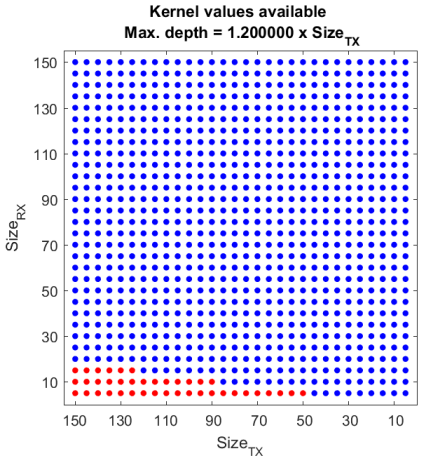
Kernel values available
Max. depth = 1.200000 x Size$_{TX}$
Size$_{RX}$
Size$_{TX}$
150 130 110 90 70 50 30 10

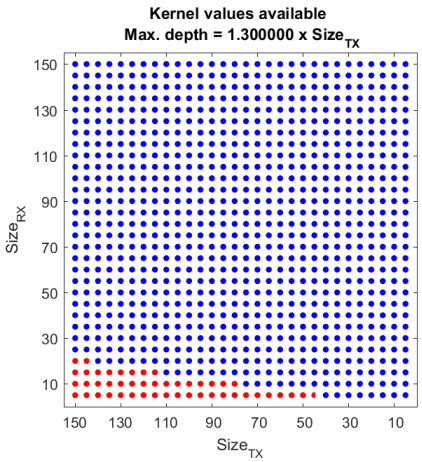
Kernel values available
Max. depth = 1.300000 x Size$_{TX}$
Size$_{RX}$
Size$_{TX}$
150 130 110 90 70 50 30 10

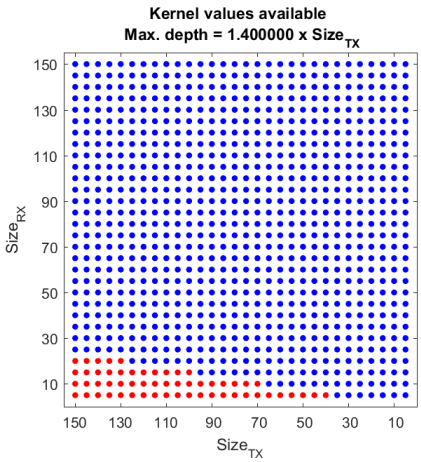
Kernel values available
Max. depth = 1.400000 x Size$_{TX}$
Size$_{RX}$
Size$_{TX}$
150 130 110 90 70 50 30 10

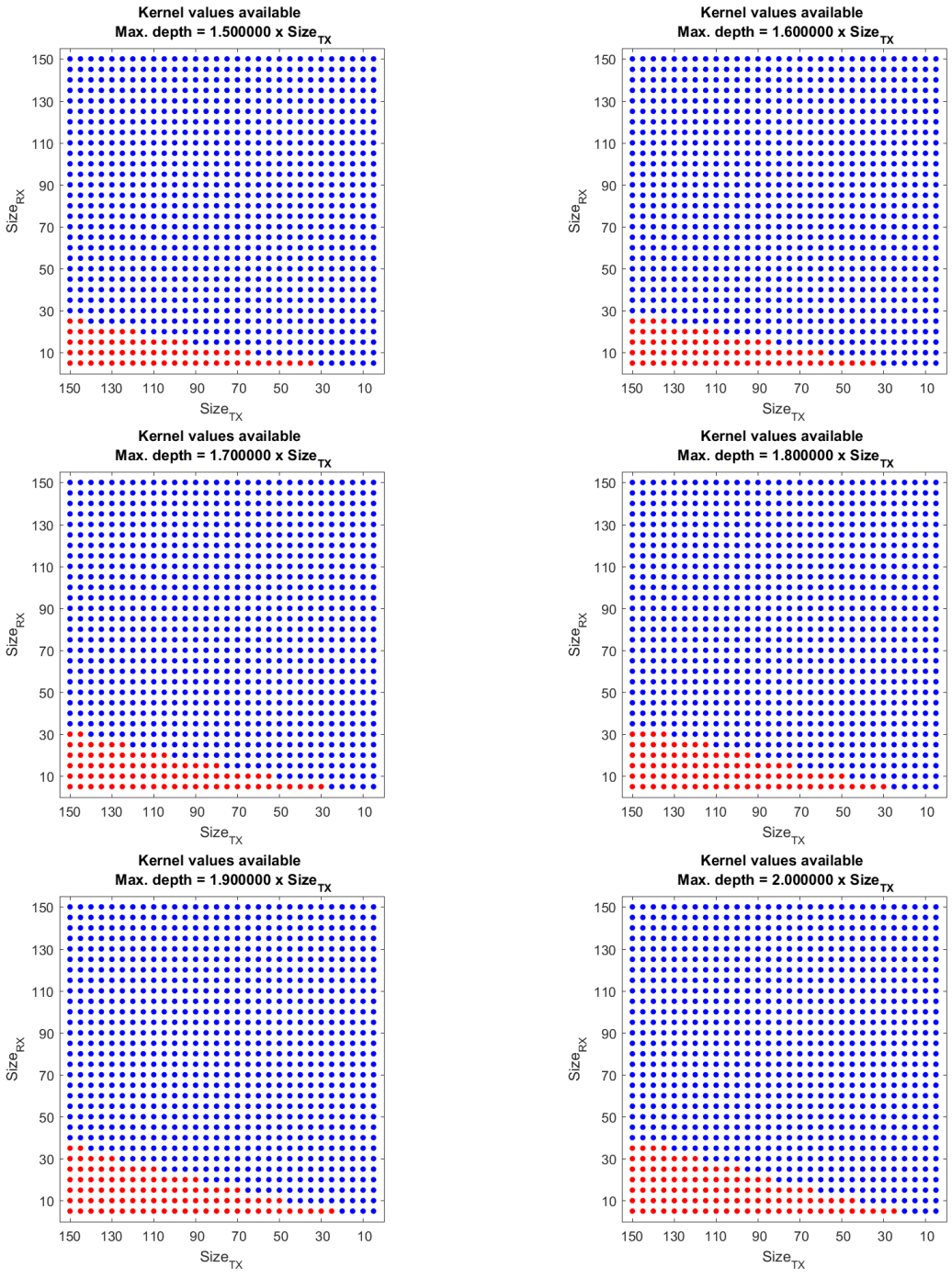

Figure A.1: Computability of the kernels for different experimental configurations. Red dots represent uncomputable combinations and blue dots represent computable kernels.

Appendix B

Sensitivity to relaxation time at low water content

In order to demonstrate the intrinsic insensitivity of the SNMR response to the relaxation time under very low water content, 1000 models have been generated and their corresponding free induction decays computed (50 m transmitter/receiver loop). Then, the SNMR response has been submitted to the DGSA algorithm (Park et al., 2016), in order to analyze the influence of the relaxation time in the response.

The models were generated with two layers. The first layer (thickness between 8 and 12 m) has a water content ranging from 1 to 3 %. The second layer has a water content between 3.5 and 35 %. The relaxation time is ranging from 5 to 500 ms.

The results of the DGSA are presented in Figure B.1. It clearly demonstrates that, in the case of a very low water content in a given layer, the relaxation time relative to this layer is a low sensitivity parameter.

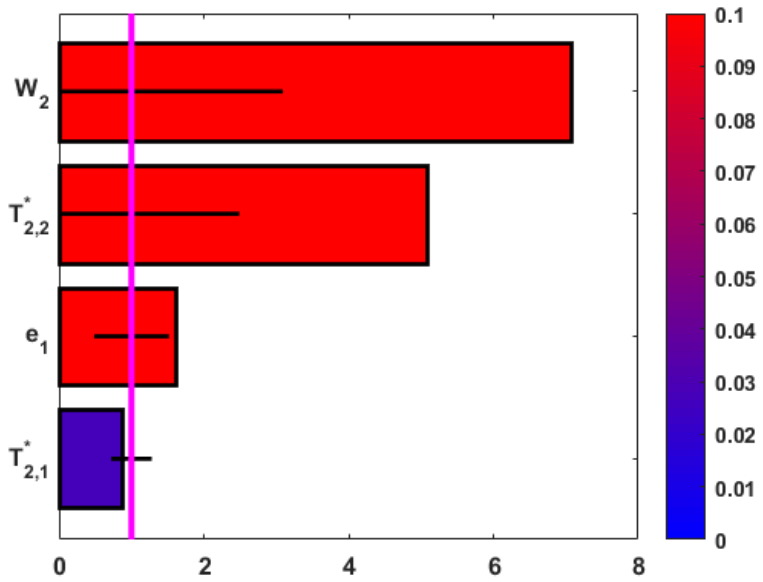

Figure B.1: Pareto plot for the sensitivity of the FID response to relaxation time.

Appendix C

Deterministic inversion: Resolution matrices

A way to assess the ability of the model to retrieve correct data in a deterministic way is to compute the associated resolution matrix. To do so, Müller-Petke and Yaramanci proposed in 2008 an approach based on the singular-value decomposition (SVD) of the forward operator:

$$\mathbf{d^{obs}} = \mathbf{Gm} = \mathbf{USV}^T\mathbf{m} \tag{C.1}$$

They suggested the use of the Picard conditions (linked to Picard plots) to assess the right truncation to apply to the decomposed problem in order to avoid noise propagation in the model. The use of the Picard condition is supposed to account for the noise level and avoid noise propagation, similarly to regularization parameters in the QT inversion (Müller-Petke & Yaramanci, 2008). It states that the value of :

$$a_i = |\mathbf{u_i}^T\mathbf{d}|/\sigma_i \tag{C.2}$$

where,

- $\mathbf{u_i}^T$ is the transpose of the i^th column of the matrix U
- $\mathbf{d}$ is the data (here, the amplitude at t=0 to comply with the linearity of the problem)
- σ_i is the i^th singular value (diagonal of S)

should remain more or less constant or decrease with the value of the index i (Fedi, Hansen, & Paoletti, 2005).

From the Picard plot, it is possible to establish a reasonable truncation. In this work, it has been chosen to use a simple algorithm to compute the "best" truncation index:

1. Compute the means of the a_i values from $i - 10$ to i
2. Compute the relative increment of each mean value
3. Find the first relative increment larger than 25%

Then, the resolution matrices were computed using:

$$\mathbf{R_m} = \mathbf{V}_p \mathbf{V}_p^T \tag{C.3}$$

with p, the truncation index ($\mathbf{V}_p$ is the matrix constituted of the p first columns of the $\mathbf{V}$ matrix from the SVD) (Müller-Petke & Yaramanci, 2008).

This process has been applied to all the inversions presented in the Subsection 7.3.2 (Chapter 7). The results of such analyses are presented in Figure C.1.

From those matrices, it is interesting to point out that the "Independent 1" and "Independent 5" datasets (hence the same transmitter/receiver) are producing the clearest resolution matrices with a very narrow resolution at the top and a spreading with depth. The other inversions are susceptible to a larger spreading of the resolution, even at low depth. However, the "depth of confidence", marked with the dashed red line, is changing with the type of transmitter/receiver couple in the "Independent" inversions, whereas this depth is not significantly changing with the "Joint" and "General" inversions. The use of the "Joint" and, to a larger extent, the "General" inversions tends to decrease the spreading of the resolution matrix along the diagonal, hence to recover the behavior of the classical inversions.

The use of the 10 m loop is also questionable from the analysis of the observation of the resolution matrices. Actually, it seems that the corresponding "Independent 3" and "Independent 6" are the ones that lead to smaller confidence depths (respectively 13.5 and 30.5 m) compared to the classical inversions. It is also observed that the "Independent 4" (30 m transmitter but 50 m receiver) resolution matrix has a large spreading around 20 m, which limits the confidence depth to 21.0 m. However, contrary to the two other limited resolution cases, the resolution of this model shows very few spreading around the diagonal above this confidence depth, which ensures a better model.

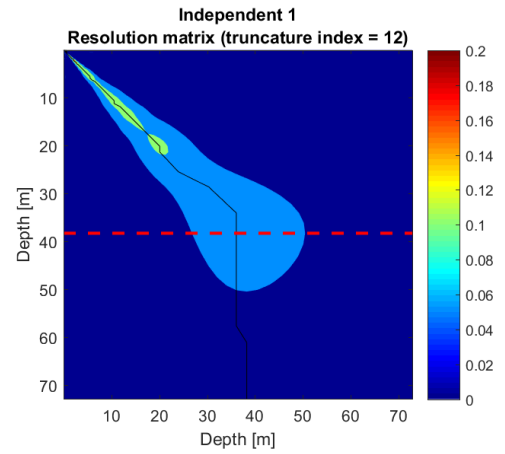
Independent 1
Resolution matrix (truncature index = 12)
Depth [m]
Depth [m]

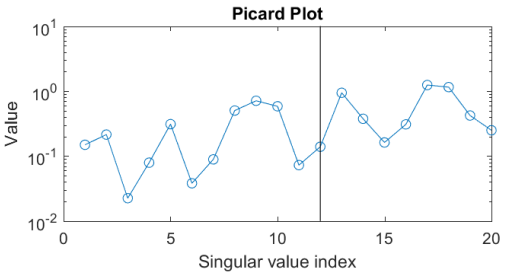
Picard Plot
Value
Singular value index

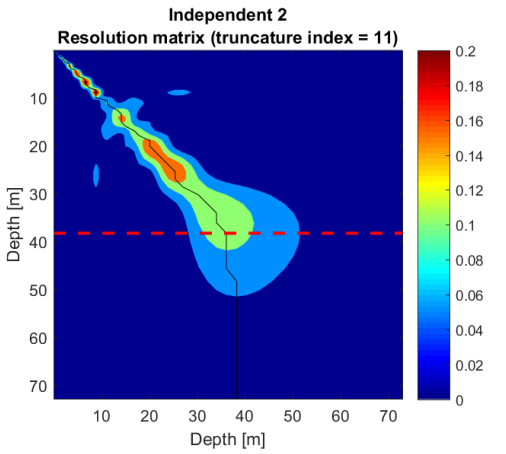
Independent 2
Resolution matrix (truncature index = 11)
Depth [m]
Depth [m]

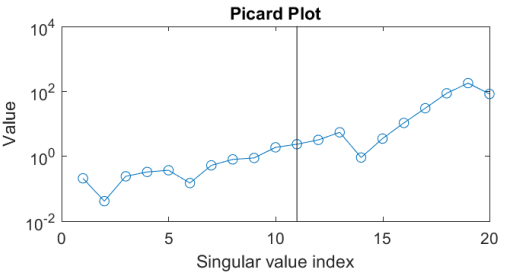
Picard Plot
Value
Singular value index

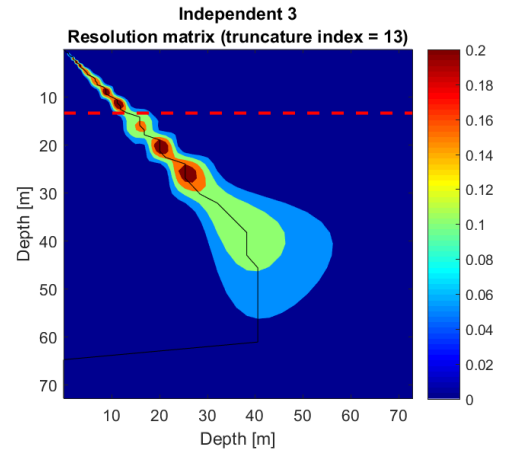
Independent 3
Resolution matrix (truncature index = 13)
Depth [m]
Depth [m]

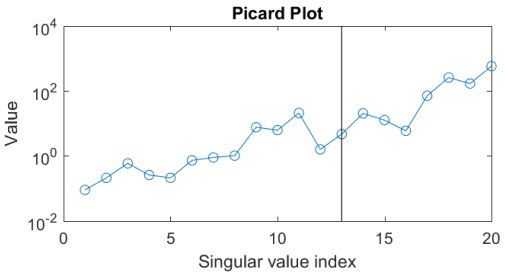
Picard Plot
Value
Singular value index

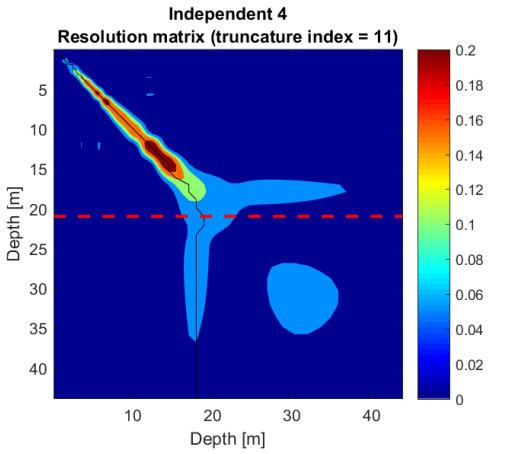
Independent 4
Resolution matrix (truncature index = 11)
Depth [m]
Depth [m]

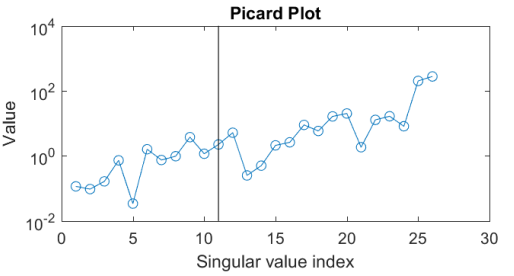
Picard Plot
Value
Singular value index

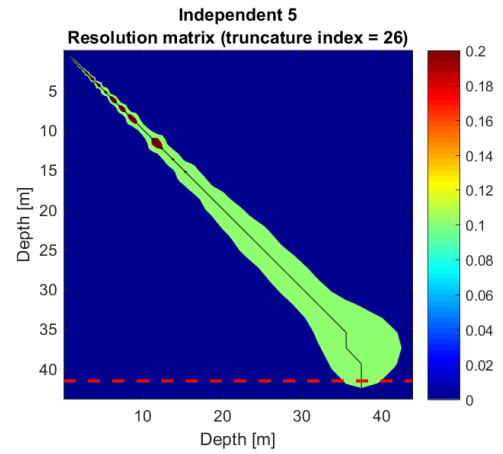
Independent 5
Resolution matrix (truncature index = 26)
Depth [m]
Depth [m]

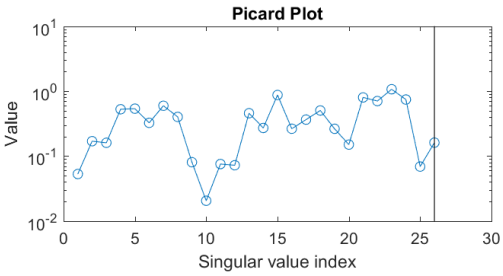
Picard Plot
Value
Singular value index

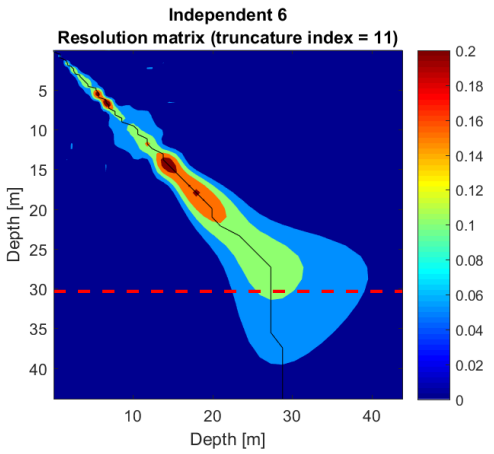
Independent 6
Resolution matrix (truncature index = 11)
Depth [m]
Depth [m]

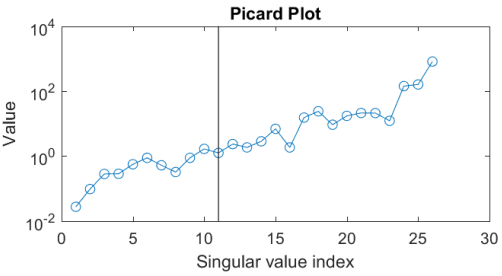
Picard Plot
Value
Singular value index

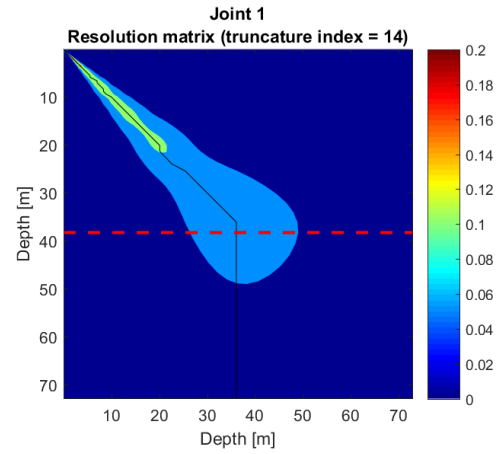
Joint 1
Resolution matrix (truncature index = 14)
Depth [m]
Depth [m]

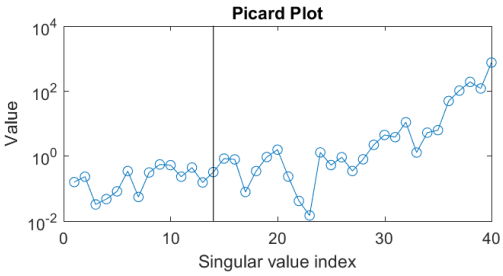
Picard Plot
Value
Singular value index

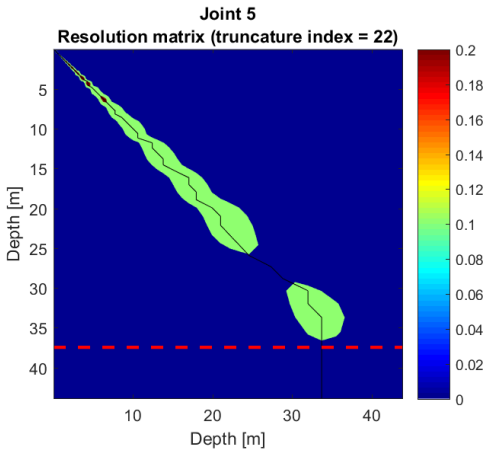
Joint 5
Resolution matrix (truncature index = 22)
Depth [m]
Depth [m]

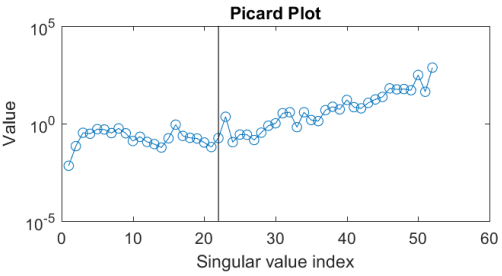
Picard Plot
Value
Singular value index

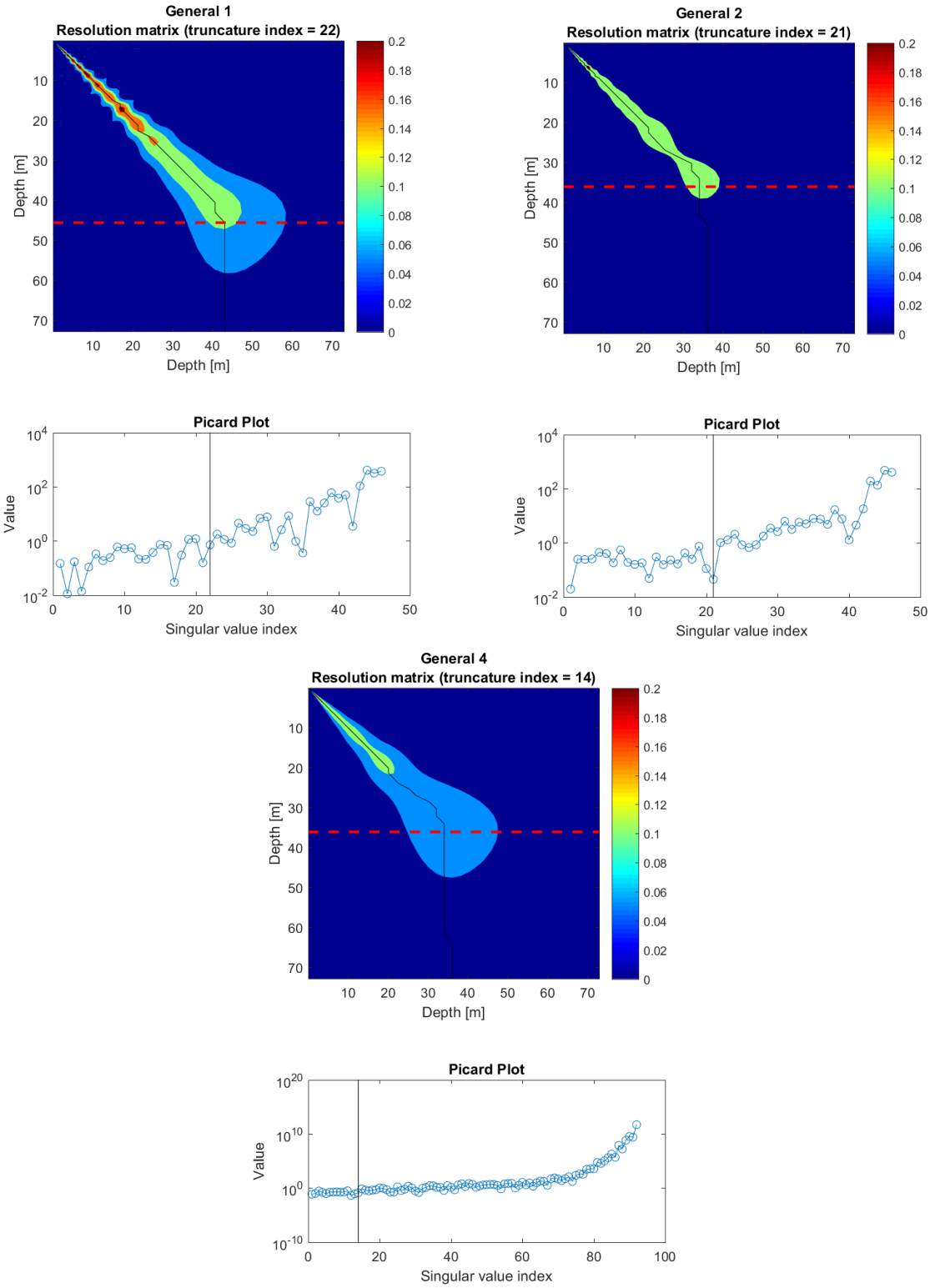

Figure C.1: Resolution matrices (absolute value) and Picard plots for the different inversions proposed in the Subsection 7.3.2. The black line represents the maximum of resolution and the dashed red line represents the maximal depth where the deviation from the diagonal is less than 10% (Müller-Petke & Yaramanci, 2008).